Stability of complex gravity currents in coastal environment

Ashraf Maskoni

▶ **To cite this version:**

Ashraf Maskoni. Stability of complex gravity currents in coastal environment. Reactive fluid environment. Université de Bretagne occidentale - Brest, 2023. English. NNT : 2023BRES0026 . tel-04440646

HAL Id: tel-04440646
https://theses.hal.science/tel-04440646v1

Submitted on 6 Feb 2024

HAL is a multi-disciplinary open access archive for the deposit and dissemination of scientific research documents, whether they are published or not. The documents may come from teaching and research institutions in France or abroad, or from public or private research centers.

L'archive ouverte pluridisciplinaire **HAL**, est destinée au dépôt et à la diffusion de documents scientifiques de niveau recherche, publiés ou non, émanant des établissements d'enseignement et de recherche français ou étrangers, des laboratoires publics ou privés.

COLLEGE DOCTORAL BRETAGNE SCIENCES POUR L'INGENIEUR

Université de Bretagne Occidentale

THESE DE DOCTORAT DE

L'UNIVERSITE
DE BRETAGNE OCCIDENTALE

ECOLE DOCTORALE N° 647
Sciences pour l'Ingénieur
Spécialité : *Mécanique des Milieux Fluides*

Par
Ashraf MASKONI

Stabilité de courants gravitaires complexes en environnement côtier

Thèse présentée et soutenue à Brest, le 01/06/2023
Unité de recherche : Institut de Recherche Dupuy de Lôme (IRDL)-UMR CNRS 6027

Rapporteurs avant soutenance :

MOPHOU Gisèle	Professeur, Université des Antilles
KAMSU FOGUEM	Bernard Professeur, Université de Toulouse - ENI Tarbes

Composition du Jury :

Président :	ASTOLFI Jacques André	Professeur Ecole Navale
Examinateurs :	MOPHOU Gisèle	Professeur, Université des Antilles
	KAMSU FOGUEM Bernard	Professeur, Université de Toulouse - ENI Tarbes
	MISHRA Rakesh	Professeur, Université de Huddersfield, UK
Dir. de thèse :	NSOM Blaise	Professeur, UBO,
Co-dir. de thèse :	LATRACHE Noureddine	Maître de Conférences HDR, UBO

Invité(s)

ASIM Taimoor	Senior Lecturer Robert Gordon University, Aberdeen, UK
OUKHLEF Aimad	MC HDR, EST de Beni Mellal, Maroc
WOUMENI Robert	Maître de Conférences, INP Grenoble

Stability of Complex Gravity Currents in Coastal

Université de Bretagne Occidentale
Ecole doctorale SPI

DISSERTATION

Stability of Complex Gravity Currents in Coastal Environment

Submitted by
Ashraf MASKONI

In partial fulfillment of the requirements
For the degree of Doctor of Philosophy

In
Coastal Engineering
Speciality: Fluid Mechanics

Supervised by
Dr. Noureddine Latrache & Prof. Dr. Blaise Nsom

March 2023

ACKNOWLEDGEMENT

This dissertation is the result of three years and six months of research activity. I would like to express my heartfelt gratitude to my supervisor Prof. Dr. Blaise NSOM and my co-supervisor Dr. Noureddine LATRACHE for their invaluable suggestions, assistance and encouragement and for everything they did for me to complete this thesis during last years.

I also thank the members of my doctoral dissertation committee Madame le Professeur Giséle MOPHOU, Vice-presidente de l'Université des Antilles en charge de la commission Recherche, Directrice du L.A.M.I.A. Monsieur Bernard KAMSU FOGUEM, Professeur, Université de Toulouse, Ecole Nationale d'lngénieur de Tarbes (ENIT) rapporteur. Monsieur Jacques André ASTOLFI, Professeur à l'Ecole Navale, Directeur de l'IRENav, examinateur. Mister Rakesh MISHRA, Professeur, Université de Huddersfield, UK examinateur. Monsieur Noureddine LATRACHE, Maître de Conférences, UBO, co-directeur de thèse. Monsieur Blaise NSOM, Professeur UBO, Directeur de thèse. Mister Taimoor ASIM, Senior Lecturer Robert Gordon University, Aberdeen, UK, invité. Dr. Aimad OUKHLEF, Maître de Conférences HDR, EST de Beni Mellal (Maroc), invité. Monsieur Robert WOUMENI, Maître de Conférences INP Grenoble, invité. I would like to extend my gratitude to Prof. Dr. Mohamed BENBOUZID, Director of Institut de Recherche Dupuy de Lôme (Université de Bretagne Occidentale).

Also, out of loyalty and gratitude to everyone who extended a helping hand to us in order to complete this dissertation, I would like to express my deep thanks and gratitude to the college de France to have funded my study throught the program PAUSE .

I would like to thank Father Guillaume GAUD, Director of the Saint Curé d'Ars International Seminary in Flavigny, for his embrace and constant assistance to us, since the first day of my family and I arrived in France.

Forever, I thank my father who died during the completion of my dissertation and my mother, who without them I would not be who I am now. Finally, and most importantly, I would like to thank my wife Dr. Anne and my son Fadi, they stood by me throughout my life and during the completion of this work.

CONTENT

LIST OF FIGURES

LIST OF TABLES

ACRONYMS

CFD	Computational Fluid Dynamics
PDE	Partial Differential Equation
VOF	Volume of Fluid

LIST OF SYMBOLS

Symbol	Definition	Units
v	kinematic viscosity	m^2/s
μ	viscosity for upper layer	Kg.$m^{-1}.s^{-1}$
μ_l	viscosity for lower layer	Kg.$m^{-1}.s^{-1}$
ω	viscosity ratio	
ε	dissipation rate of turbulent kinetic energy	m^2/s^2
ρ	density for upper layer	Kg/m^3
ρ_l	density for lower layer	Kg/m^3
D	density ratio	
t	time	s
g	magnitude of gravity acceleration	m/s^2
h	depth of gravity current (lower layer)	m
H	depth of ambient fluid (upper layer)	m
x	horizontal coordinate	m
y	lateral coordinate	m
z	vertical coordinate	m
u	horizontal velocity	m/s
p	pressure	N/m^2
Q	the flux ratio between the two fluids	
q_{l0}	the intial flux of lower layer	$mol * m^{-2}/s$
q_0	the intial flux of upper layer	$mol * m^{-2}/s$
l	the lower layer	
L	the characteristic length of the flow	m
m		
T	the characteristic time scales	s
s		
A	constant depends on the dimensionless parameters	
a	constant depends on the dimensionless parameters	
σ	surface tansion	Nm^{-1}
ρ_1	the density of lighter liquide	Kg/m^3
ρ_2	the density of denser liquide	Kg/m^3
μ_1	the viscosity of lighter liquide	Kg.$m^{-1}.s^{-1}$

μ_2	the viscosity of denser liquid	$\mathrm{Kg}.m^{-1}.s^{-1}$
$h(x,t)$	thickness of the gravity current	m
$H(x,t)$	thickness of the ambient fluid	m
U	horizontal velocity	m/s
V	vertical velocity	m/s
U_b	horizontal velocity of basic flow	m/s
V_b	vertical velocity of basic flow	m/s
p_b	pressur of basic flow	Pa
X	horizontal non-dimensional coordinates	m
Y	vertical non-dimensional coordinates	m
m	the viscosity ratio	
$\psi(x,t)$	stream function	
c	complex number	
α	real number	
T	the interface tension	mN/m
$\xi(x,t)$	interface height	
$\alpha(x,t)$	a small angle is defined between the horizontal axis and the tangent to the interface at abscissa and time.	
$\overleftarrow{h}(x,y,t)$	the left-moving lane interface	m
$\vec{h}(x,y,t)$	the right-moving lane interface	m
$\overleftarrow{H}(x,y,t)$	the left-moving lane interface upper surface	m
$\vec{H}(x,y,t)$	the right-moving lane interface upper serface	m

GENERAL INTRODUCTION

The coast is the contact zone between the mainland and the sea. It is a place of different activities such as tourism, leisure, fishing, etc. It is therefore likely to collect polluted liquid coming both from the sea and from the mainland. Those that come from the sea are for example heavy crude oil and those come from the land are generally releases from human activities. We are interested for the case where intrusive liquid which is moved by gravity alone and is called the gravity current, is denser than seawater and therefore flows below it. Hydrodynamic stability analysis of this gravity current is fundamental as it will determine if a small disturbance will grow or vanish.
To tackle that problem, we consider two configurations:

1) The gravity current propagates upon a sloping plane and beneath static water. Both liquids are immiscible with different densities and equal viscosities; the seawater depth is much greater than the thickness of the gravity current. A small disturbance (perturbation) is superimposed to the basic laminar flow and we investigate its temporal instability, in order to determine the critical parameters characterizing the occurrence of the instability. The investigation is analytic.
2) Two immiscible liquids of different densities are released in lockexchange configuration upon horizontal plane. Both liquids are immiscible with equal viscosities. The difference of density is kept fixed while the viscosities are increased to control the initial Reynolds number (Re_0). The interfacial surface tension is varied to control the initial Weber number (We_0). The Reynolds and Weber numbers permit to determine the threshold of the interface instability between the seawater and the denser liquid. The investigation is performed by the numerical simulations.

The main goal of this work is to identify the nature of the instabilities created at the interface in stratified flow between two immiscible liquids with different densities. The competition between stratification and shear leads to Kelvin-Helmholtz or Holombe instability at the interface (Figures Pouliquen 1994, Alexakis 2009, Carpenter 2010). The answer to this question is to compare the thickness of the velocity gradient (δ_u) and that of the density gradient (δ) close to the interface. For the case of two immiscible liquids, the thickness of the density gradient is equal to zero (δ=0). In this case, only the interface position and velocity gradient need to be calculated (figure 0). We must state if the instability is of the Holomboe type and validate the result.
The manuscript is organized in three chapters:

The first chapter presents the literature: description of generalities on gravity current, main previous theoretical experimental and numerical studies on gravity currents, mains previous works in our laboratory on gravity current in coastal environment and finally the scientific project of this thesis. The second chapter is devoted to the analytical study of the gravity current that propagates upon a sloping plane and beneath static water. After a presentation of the instability due to viscosity stratification, Kelvin-Helmhotz instabilities, an extension of the Kowal model, we develop a general analytical model taking into a count the density stratification, the interfacial surface tension and the slope. The results have been published in the International Journal of COMADEM (Maskoni et al., 2023).

In the third chapter, we present the numerical simulations of a system of two immiscible liquids in the lockexchange configuration upon horizontal plane performed with the help of OpenFoam softwar. The obtained results from the numerical simulations are validated by the Huppert theory (Huppert et al., 1982) of the space-time front position with the initial Reynolds number lying between 25 and 7000 and with the initial Weber number lying between 5 and 2000. We have investigated the hydrodynamic field close to the unstable interface in order to identify the nature of the instabilities.

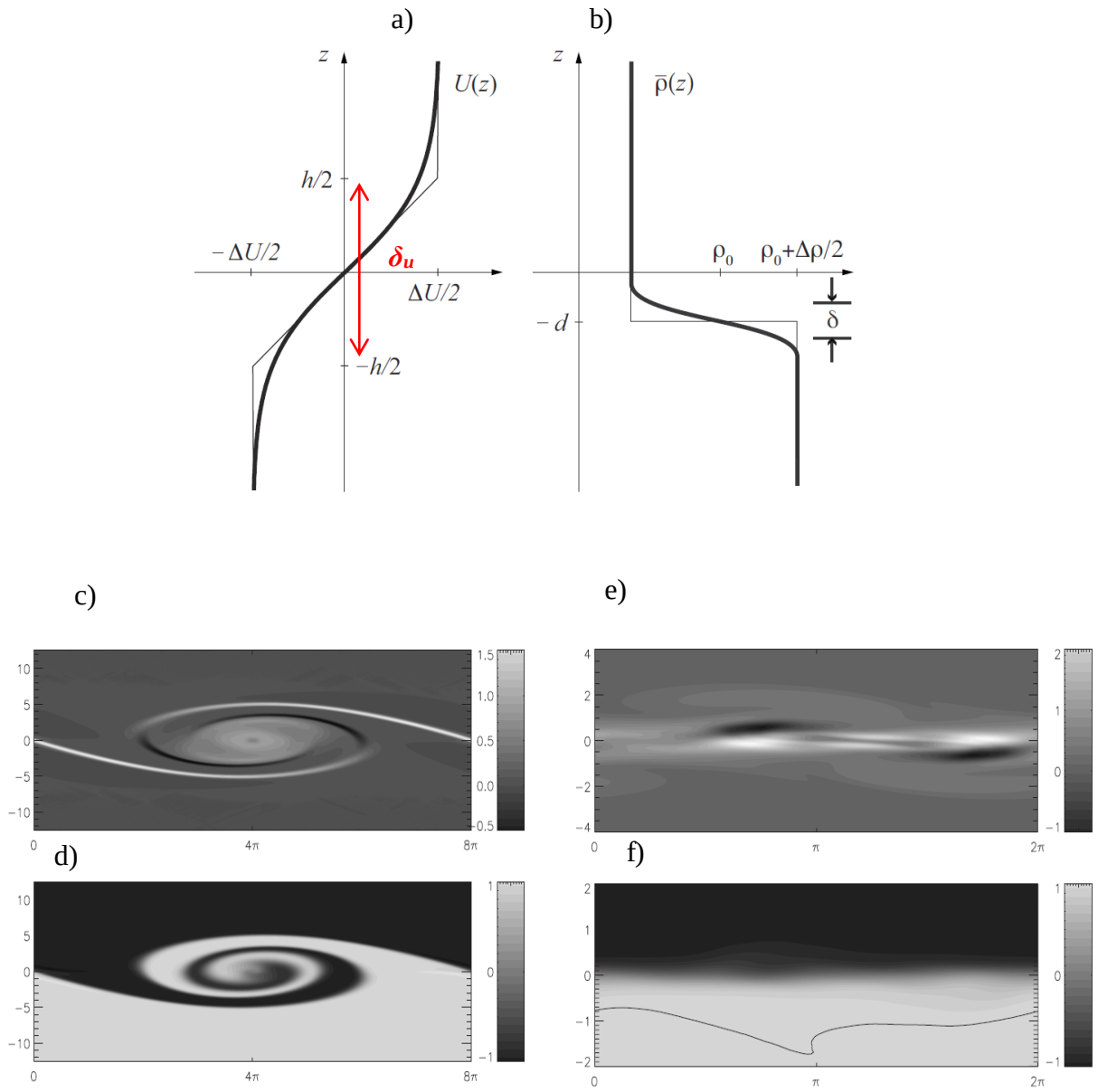

Figure 0. (a,b) Gray-scale image of the vorticity (top panel)and the density lower. (c,d) Gray-scale image of the vorticity (top panel) and the density (lower panel) field at the nonlinear stage for the first Holmboe mode instability. (e,f) Gray-scale image of the vorticity (top panel) and the density (lower panel)field at the nonlinear stage for the second Holmboe instability(Alexakis, 2009 & Carpenter and al.,2010)

INTRODUCTION GÉNÉRALE

La côte est la zone de contact entre la terre ferme et la mer. C'est un lieu de différentes activités telles que le tourisme, les loisirs, la pêche, etc. Elle est donc susceptible de collecter des liquides pollués provenant aussi bien de la mer que de la terre ferme. Ceux qui viennent de la mer sont par exemple du pétrole brut lourd et ceux qui viennent de la terre sont généralement des rejets d'activités humaines. Nous nous intéressons au cas où le liquide intrusif qui est déplacé par la seule gravité et est appelé le courant gravitaire, est plus dense que l'eau de mer et s'écoule donc en dessous. La stabilité hydrodynamique de ce courant gravitaire est fondamentale et déterminera si une petite perturbation va croître ou s'évanouir.
Pour résoudre ce problème, nous considérons deux configurations :

1) Le courant gravitaire se propage sur un plan incliné et sous l'eau statique. Les deux liquides sont immiscibles avec des densités différentes et des viscosités égales ; la profondeur de l'eau de mer est très supérieure à l'épaisseur du courant gravitaire. Une petite perturbation est superposée à l'écoulement laminaire de base et nous étudions sa stabilité temporelle, afin de déterminer les paramètres critiques caractérisant l'apparition de l'instabilité. L'étude est analytique.

2) Deux liquides immiscibles de densités différentes sont libérés dans une configuration de lockexchange sur un plan horizontal. Les deux liquides sont immiscibles avec des viscosités égales. La différence de densité est maintenue fixe tandis que les viscosités sont augmentées pour contrôler le nombre de Reynolds initial (Re0). La tension interfaciale est variée pour contrôler le nombre de Weber initial (We0). Les nombres de Reynolds et de Weber permettent de déterminer le seuil d'instabilité de l'interface entre l'eau de mer et le liquide plus dense. L'investigation est réalisée par des simulations numériques.

L'objectif principal de ce travail est d'identifier la nature des instabilités créées à l'interface en écoulement stratifié entre deux liquides immiscibles de densités différentes. La compétition entre stratification et cisaillement conduit à une instabilité de Kelvin-Helmholtz ou Holombe à l'interface (Figures Pouliquen 1994, Alexakis 2009, Carpenter 2010). La réponse à cette question est de comparer l'épaisseur du gradient de vitesse (δu) et celle du gradient de densité (δ) près de l'interface. Pour le cas des liquides immiscibles, l'épaisseur du gradient de densité est égale à zéro ($\delta=0$). Dans

ce cas, seuls la position de l'interface et le gradient de vitesse doivent être calculés (figure0). Il faut dire si l'instabilité est de type Holomboe et valider le résultat.

Le manuscrit est organisé en trois chapitres :

Le premier chapitre présente la littérature : généralités sur les courants gravitaires, principales études théoriques expérimentales et numériques antérieures sur les courants gravitaires, principaux travaux antérieurs dans notre laboratoire sur les courants gravitaires en milieu côtier, et presentation du projet scientifique de cette thèse. Le deuxième chapitre est consacré à l'étude analytique du courant de gravité qui se propage sur un plan incliné et sous l'eau statique. Après une présentation de l'instabilité due à la stratification de la viscosité, les instabilités de Kelvin-Helmhotz, une extension du modèle de Kowal, nous avons développé un modèle analytique général prenant en compte la stratification de la densité, la tension interfaciale et la pente. Les résultats sont publiés dans le Journal International de COMADEM (Maskoni et al., 2023).

Dans le troisième chapitre, nous présentons les simulations numériques réalisées à l'aide du logiciel OpenFoam dans la configuration du lockexchange sur plan horizontal. Les résultats obtenus à partir des simulations numériques sont validés par la théorie de Huppert (Huppert et al., 1982) par la determination spatio-temporelle de la position du front pour des valeurs du nombre de Reynolds initial comprises entre 25 et 7000 et pour des valeurs du nombre de Weber initial comprises entre 5 et 2000. Nous avons étudié le champ hydrodynamique proche d’une interface instable afin d'identifier la nature des instabilités.

CHAPTER I
Literature

1 Chapter I Literature

1.1 General presentation of gravity currents (GC)

Gravity currents are pertinent to engineering sciences, namely with regard to environmental protection from pollution among other concerns (e.g. process engineering). Pollution of ocean limits our ability to use oceans for economic, recreational and aesthetic purposes, can inhibit economic growth (Thanh Ca&al.2014a). The polluted ocean is a public health risk. It can cause significant changes in ecosystems that harm the health and livelihoods of communities. So discharged effluent in ocean such as heavy crude oil spill due to ships overloading is an environmental disaster that needs to find appropriate solutions and address it. This disaster can be represented by propagation of anthropogenic gravity currents. The following section will be to provide a presesntation general of gravity currents and as follows:

1.1.1 Gravity Currents

Gravity currents or “density/turbidity /buoyancy currents” are flows generated by a density gradient between two fluids and occur in both natural and industrial flows. The density differences can be due to the variations in salinity, temperature, or concentration of suspended particulates (Simpson1997& Benjamin 1968).

Gravity currents are a ubiquitous phenomenon in the atmosphere or water bodies. They can be observed in both natural and anthropogenic environments, and there are numerous examples of gravity currents. In the atmosphere, the sea breeze is a well-know example of gravity current. The sea breeze (Figure1.1a), which is the flow of cool moist air from the sea to the land. On a warm day the sun heats the land more than the sea and, consequently, the air at low altitudes over the land is warmer than that over the sea. The resulting density difference drives the sea breeze (Breeze& Linden2004).

Gravity currents can also be found in the industral setting: When we pour honey on a pancake and we let it spread out on its own (thespruceeats.com), as shown as bellow in Figure1.1b.

(a)

(b)

Figure1.1: Example of gravity currents in the atmosphere and the industral: (a) the atmosphere gravity current (the sea breeze) (b) the industral gravity currents (honey) on Cinnamon Pancakes.

Gravity currents can also be found in the natural setting. Regarding natural examples include a hot particle-laden gravity currents, or pyroclastic flow from the eruption of Mt. Unzen in Japan 2001 and a pyroclastic flow on Montserrat in the Caribbean (Huppert2006). Shell Oil Spill in the Gulf of Mexico-Greenpeace in USA 2010 (https://www.greenpeace.org/usa/90000-gallon-oil-spill-looks-like/shell-oil-spill-in-the-gulf-of-mexico-4). Oil from the 2010 spill flowed toward the coast of Alabama(https://www.nsf.gov/news/mmg/mmg_disp.jsp?med_id=133765&from) as shown as follows:

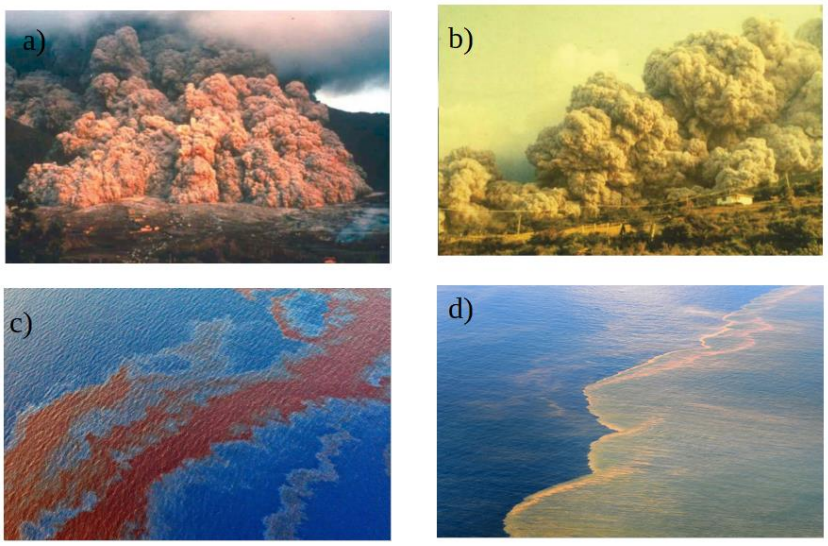

Figure 1.2: Example of gravity currents in the natural and industral environment: (a) A hot, particle-laden gravity current, or pyroclastic flow, from the eruption of Mt. Unzen in Japan. (2001), (b) A pyroclastic flow on Montserrat in the Caribbean (photographer: R. S. J. Sparks), (2001). (c) Shell Oil Spill in the Gulf of Mexico (2010). (d) Oil from the spill flowed toward the coast of Alabama.

A natural example to intrusive gravity currents is the “Morning Glory” phenomenon in northern Australia, where fluid of one density propagates along an interface between two homogeneous layers (Clarke and al.1981 & Smith and al. 1982). Morning Glory is an amplitude-ordered series of

solitary waves that form a series of roll clouds, The roll cloud is often very smooth in appearance, several hundred meters in diameter and 100-1000 km long, traveling at a speed of 10-20 ms^{-1} at 500 m above the ground. Seen near the southern coast of the Gulf of Carpenteria in northern Australia. “Morning Glory” phenomenoncan be seen in Figure1.3.

Figure1.3: Example of intrusive gravity currents is the “Morning Glory” phenomenon in northern Australia (Morning glory cloud over Goondiwindi July 2017).

For all these examples, there are several reasons for studying gravity currents:

(1) To assimilate this phenomenon and understand its various stages: The resting stage, the spreading stage and the deceleration phase.

(2) The consequences of a spillage of heavy crude oil is disastrous, as illustrated by Oil Spill in the Gulf of Mexico in 2010, Figure 1.2 (c). For this reason, the study of gravity currents to assess the risks if they occur.

(3) Because of thier economic significance, there is an economic importance for the study of gravity currents, which is represented by important economic costs related to the problem of loss of storage capacity in reservoirs due to one of the types of gravity currents, which are called turbidity currents (Cesare & al.2001).

1.1.2 Description of gravity current flow

The basic sketch of a typical gravity current configuration is shown in Figure1.4. Important parameters that determine gravity currents propagation are the total depth of the fluid layer (H), depth of the gravity current (h), the density diference between the two fluids (Δρ), the the gravitational acceleration (g), the density of heavy fluid ρ, the density of ambient fluid (ρ-Δρ), and reduced gravity $\acute{g} = (g\Delta\rho)/(\rho - \Delta\rho)$.

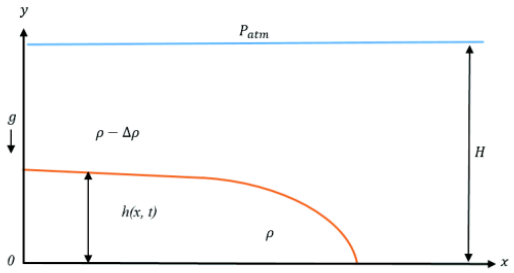

Figure 1.4. Basic sketch of a gravity current

The gravity current with density ρ propagates into the ambient fluid with a different density (ρ-Δρ). If the difference in density is small, so that the buoyancy forces are of equal or greater magnitude than the inertial forces, in this case, this system is called by Boussinesq system.

The gravity current's shape consists of the head, which is the leading edge of the gravity current, is a region in which relatively large volumes of ambient fluid are displaced. Its height is approximately twice the height of the current in the next phase of the flow (Simpson.1982), in the frontal zone of the current (the head) a nose rising above in the next phase of the flow can usually be observed (Simpson 1997). The body and tail is the bulk of flow that follows the head. Gravity flow characteristics can be characterized by the Froude and Reynolds numbers, which is an important dimensionless parameter, and represent the ratio of flow speed to gravity (buoyancy) and viscosity, respectively (Huppert.2006).

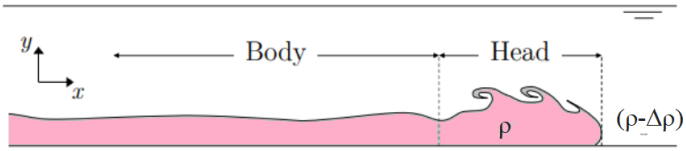

Figure 1.5. A schematic diagram of the gravity current sections

1.1.3 Non-dimensional parameters

The most important non-dimensional parameters for a Boussinesq gravity current are:

1- Reynold number (Re), which is defined as the ratio of inertial forces to viscous forces. Reynolds number is given by the following well-known formula: $R_e = U_b h/v$ where U_b is the current velocity, v is kinematic viscosity, h is the height of gravity current. U_b can be calculated as $U_b = \sqrt{g'H}$, H depth gravity current, $g' = g\frac{\rho_2 - \rho_1}{\rho_1}$ reduced gravity. Reynolds number measures the importance of viscous dissipation on the current (Marianoi & al.2007).

2- The Froude number (Fr), which is defined as the ratio between the inertia and gravity forces in a fluid, which is defined as $F_r = U/\sqrt{\acute{g}h}$ where h hydraulic mean depth(m), U velocity (m/s) and g acceleration of gravity (9.81 m/s^2).

3- Weber number (We), which is defined as the ratio between the inertial force and the surface tension force. Weber number is given by the following well-known formula $W_e = \rho U^2 h/\sigma$, where h is the height of gravity cur rent, σ surface tension, and ρ density current. It can be thought of as a measure of the relative importance of the fluid's inertia compared to its surface tension. The quantity is useful in analyzing thin film flows and the formation of droplets and bubbles (Day& al.2012).

4- The Richardson number (Ri) which is defined as the ratio of the buoyancy term to the flow shear flow term. Richardson number is given by the following well-known formula: $R_i = \frac{g}{\rho}\frac{\partial\rho/\partial y}{(\partial u/\partial y)^2}$, where g is gravity, ρ is density, u represents flow velocity, y represents the depth. The Richardson number, of practical importance in investigating density and turbidity currents in oceans, lakes, and reservoirs. And it is used to estimate the level of turbulence in the gravity currents flows (Kundu & Cohen 2002).

The phenomenon of gravity currents has a broad and active field of academic research and engineering applications. In fluid dynamics, the dynamics of gravity currents have been widely studied by laboratory experiments and numerical simulations. The study of gravity currents has generated a quite large literature including some partial review papers e.g. (Griffiths and al.1986 & Felix & a l.2002). The start of quantitative study (or modeling) of gravity current is attributed to von Karman in 1940, where the first quantitative study of gravity currents flows was done by Von Karman, who evaluated the spread of poisonous gas (Huppert 2006). Subsequently, (Karm 1940) formulated a classical relationship for the GC depth and velocity using Bernoulli's theorem in which a heavier fluid advances into the lighter atmosphere: $F_r = U/\sqrt{\acute{g}h}$, where h and U are the depth and velocity of the front or leading edge of the GC, respectively. Fr is the Froude number of the GC front, which was evaluated by Von Karman to equal $\sqrt{2}$ in the context of a relatively deep ambient (Benjamin 1968) argued that Von Karman's formulation was invalid because he applied Bernoulli's theorem across a streamline characterized with head losses. Subsequently, Benjamin re-derived this expression $F_r = U/\sqrt{\acute{g}h}$ using the momentum integral and ended up with the same results. This result surprised Benjamin; however, because both approaches used a different integral of the Euler equation, they could not have reached different results (Huppert 2006).

1.1.4 Gravity current flow stages

The gravity current evolves through three stages, defined by the dominant forces acting upon it. During the initial stage, known as the slumping stage, non-equilibrium condition occurs between the two fluids. Hence the heavier fluid flows under the lighter one, producing the gravity current, this stage, which is characterized by the initial drop in depth And increase the velocity of the current and the head, body(and tail) of the gravity current are formed, and the height of the current decreases. The buoyancy forces dominate and the front travels at a quasi-constant velocity. After travelling a certain distance, the current transitions into the self-similar phase, during which the front starts decelerating with the velocity following a $t^{-1/3}$ law (Huppert & al.1980, Gratton and al.1994). During the final stage, the current rush decreases and the velocity decreases because the gravity current becomes at this stage surrounded by the ambient fluid that works to trap and impede the progress of the gravity current. In this stage onward the propagation rate decreases with time and the current gradually slows down. Finally, as the current spreads even further, it becomes so thin that viscous forces between the intruding fluid and the ambient and boundaries govern the flow. Viscous forces start to dominate over the inertial-buoyant forces, and the current enters the buoyant-viscous phase characterised by an even faster deceleration which follows a $t^{-4/5}$ law (Huppert & al.1982, Rottman & al.1983).

1.1.5 Classification of gravity currents

Bottom gravity currents or (turbidity currents, debris flow) are generated when the gravity current density is greater than the density of the ambient fluid, upper gravity currents are generated when the gravity current density is less than the density of the ambient fluid. Furthermore, gravity currents can also occur as intrusions of mixed fluid in a sharply or linearly stratified ambient (Ungarish2009).

According to the different density types of the current and the ambient fluid, gravity currents can be draw as: (1) Bottom gravity currents (Figuer1.5(a)), when the current is denser than the ambient fluid, $(\rho > (\rho - \Delta\rho))$. (2) Upper greavity currents (Figuer1.5 (b)) if the density of the current is lower than the ambient fluid ($\rho < (\rho - \Delta\rho)$). (3) Intrusion of "mixed" fluid in a sharply stratified ambient (Figuer1.5(c)) when the current has intermediate density value when compared to the stratified ambient fluid. (4) Intrusion of "mixed" fluid in a linearly-stratified ambient, with $\rho = (\rho - \Delta\rho)$(Figuer1.5 (d)).

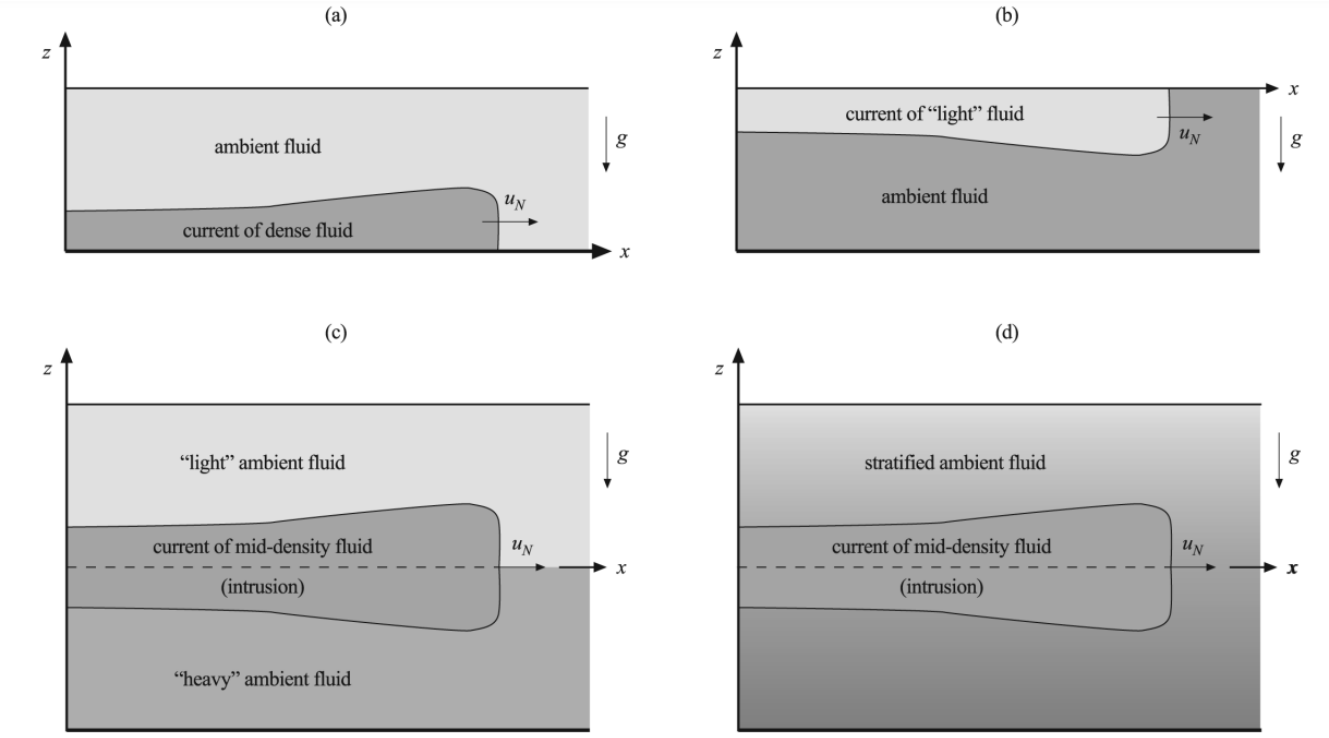

Figure 1.6: Schematic description of typical gravity current configurations (a) bottom current of more dense (heavy) fluid $\rho > (\rho - \Delta\rho)$; (b) top (surface) current of less dense (light) fluid, $\rho < (\rho - \Delta\rho)$; (c) intrusion of "mixed" fluid in a sharply stratified ambient ; (d) intrusion of "mixed" fluid in a linearly-stratified ambient, $\rho = (\rho - \Delta\rho)$ (y= 0).

On the other hand, gravity currents can be categorized as compositional or particle-driven gravity currents. In the case of compositional gravity currents. The movement of the gravity current is caused by the difference in density as we mention above. While for particle-driven gravity currents, the driving force is represented by the suspension of sediments. By depending on the concentration intensity of the sediment, three main types of gravity currents flow can be distinguished: (1) debris flows: Debris flows are characterized by the cohesion existing between the transported particles (sands, pebbles). (2) Granular (or fluidized) flows: This type flow occurs in silts, sands (3) liquefied flows: Liquefied flows are mainly due to a rapid increase in pressure interstitial of the fluid. Liquefied flows are characterized by non-cohesive particles (sands or silts), held in suspension by the over pressure of the interstitial fluid. From the three main types of gravityl currents, depending on the concentration of particles.

1.1.6 Classification

Gravity currents can be of the following types:

1 – **Constant (fixed) / non-constant volume**

Depending on the volume of the fluid, gravity currents can be divided into two types, the first type is gravity currents which is of finite volume. In this type, Fixe volume gravity currents, are generated in the laboratory using a lock-exchange tank in which the two fluids of different densities are separated by a vertical barrier. The vertical barrier is swiftly removed, and the intruding fluid collapses into the receiving ambient, eventually giving way to a constant-volume gravity current. The second type of gravity current is called non-finite volume gravity current which is provided by a continuous source.

2 – **Inviscid / viscous**

Viscous gravity currents propagate under a balance between viscous and buoyancy forces (and the two fluids are usually considered essentially immiscible). The Reynolds number $R_e = UL/v$ gives an indication of the ratio of these two effects (inviscid or viscous). Here U, L and v are the typical velocity, length and kinematic viscosity of the current. A current is inviscid or inertial when $R_e \ll 1$, and viscous when Re is not large.

3 – **Boussinesq /non-Boussinesq**

If the difference of the density between the gravity current and the ambient fluid is small, then the current is a Boussinesq type. Otherwise, it is called non-Boussinesq type.

4 – **Homogeneous / stratified ambient**

It depends on the density of the ambient fluid as a function of the vertical coordinate. The case of homogeneous in the ambient fluid is the simpler and the more investigated. The stratified ambient is the most interesting, difficult. The difference between them is that gravity currents and intrusions in a continuously-stratified ambient propagate more slowly than in a homogeneous ambient for similar geometry.

5 – **Gravity current / intrusion**

A gravity current propagates on a wall defined lower or upper geometric boundary of the system, such as the bottom or top of a channel, including the free surface but an intrusion propagates horizontally inside a stratified fluid, typically like an isolated wedge which does not touch the horizontal boundaries. The guiding surface z = 0 say, is plane of neutral buoyancy for the intruding fluid.

6 – **Two-dimensional (2D) rectangular geometry / axisymmetric (cylindrical) geometry**

In the two-dimensional (2D) rectangular geometry, the axis of symmetry is not vertical, and the current propagation horizontally but in the cylindrical case, the axis of symmetry is vertical, and the current propagation in the radial direction(r). The curvature terms in the axisymmetric system introduce some non-trivial differences to the 2D current. In particular, we note that a cylindrical current may be convergent (propagate from the periphery of the container to the center), or divergent (spread out in the positive r direction).

7 – **Rotating / non-rotating frames**

In a current in a x-long box bounded by vertical side-walls, the major Coriolis acceleration is in the direction y but for an axisymmetric gravity current. The coriolis acceleration is in the direction of spread, hinders the propagation. and eventually renders.

1.1.7 Gravity current produced by lock exchange

The most straight forward approach to study density currents is the immediate release of a fluid of fixed volume to another fluid of large volume. In a lock exchange technique, the two fluids have different densities in a tank. At the first stage the two fluids at rest and separated by a vertical barrier-the lock gate-in a tank. When removing the septum, differences in the hydrostatic pressure cause the denser fluid to flow in one direction along the bottom boundary of the tank, while the lighter fluid flows in the opposite direction along the top boundary of the tank. A dense gravity current travels to the right along the lower boundary and a buoyant current travel to the left along the upper boundary. We can observe the flows are approximetly symmetric, and the dense fronts travel at almost the same speeds and at the same times (SHINand al.2004). When the lock is removed, the gravity current flows and it is consist of, a head, body and a tail. The head, which is the leading edge of the gravity current, is a region in which relatively large volumes of ambient fluid are displaced. The body and tail are the bulk of flow that follows the head. The depth of the current becomes much less than half of the total depth. If the gravity current movement is fast when the lock is removed, a region of mixed liquid is formedin the upper region of the head of the gravity current, vertical velocities are generally much smaller than horizontal velocities in the current, and Flow characteristics can be characterized by the Froude and Reynolds numbers, which represent the ratio of flow speed to gravity (buoyancy) and viscosity, respectively. After that the propagation rate decreases with time and the current gradually slows down. Finally, as the current spreads even further, it becomes so thin that viscous forces between the intruding fluid and the ambient and boundaries govern the flow.

1.2 Main previous works and their results

Many previous theoretical, experimental and numerical studies, deals with gravity currents, and the results obtained had the greatest impact in providing a lot of information about this phenomenon. The first credit for the results and information obtained is to the giant names in the subject, including Von Kàrmàn (Von Kàrmàn1940), Benjamin (Benjamin1968) and Simpson (Simpson 1997) and others. The following is the representation of the most important research works and its results, which are closely related to this thesis.

In 1940, Theodore Von Karman, investigated the applications of analytical methods available for the solution of certain nonlinear problems in which the engineer was interested. The phenomenon of gravity currents has been discussed. The purpose of his paper was to improve the convergence between the viewpoints of mathematics and engineering, and induce mathematicians to volunteer for pioneering work in such engineering problems (Von Kàrmàn 1940).

In 1967 Benjamin presented a broad investigation into the properties of steady gravity currents. It was represented by perfect-fluid theory and simple extensions of it (like the classical theory of hydraulic jumps) that give a rudimentary account of dissipation. The effects of viscosity and mixing of the fluids at the interface were ignored, the hydrodynamical problem was formally the same as that for an empty cavity advancing along the upper boundary of a liquid. The problem is treated as a prototype for the class of physical problems under study: most of the analysis was related to it specifically, but the results thus obtained were immediately applicable to gravity currents by scaling the gravitational constant according to a simple rule. The possible states of steady flow in the present category between fixed horizontal boundaries were examined on the assumption that the interface becomes horizontal far downstream. A certain range of flows appears to be possible when energy was dissipated; but in the absence of dissipation only one flow is possible, in which the asymptotic level of the interface was midway between the plane boundaries. The corresponding flow in a tube of circular cross-section is founded. The theory was shown to be in excellent agreement with the results of recent experiments by (Zukoski 1966). The two-dimensional energy-conserving flow was investigated. A close approximation to the shape of the interface was obtained. The discussion turns to the question whether flows characterized by periodic wavetrains were realizable, and it appears that none is possible without a large loss of energy occurring. The case of infinite total depth was considered, relating to deeply submerged gravity currents. It was shown that the flow must always feature a breaking ‘head wave’, and various properties of the resulting wake were demonstrated. Reasonable agreement was established with experimental results obtained by Keulegan & al. (Benjamin 1968 & Keulegan 1957).

In 2002, Simpson & al., measured the linearly stratified fluid experimentally and calculated numerically. Their goal was to determine how this sequence is modified when the heavy fluid is released at the lower boundary of tank containing a linearly stratified ambient fluid that is, how the internal waves produced by the lock release interact with the current to change its characteristics and how it, in turn may change the wave field. The density, bottom to top, of the stratification was (ρ_b-ρ_0) and its intrinsic frequency is N. For a given ratio of the depth of released fluid h to total depth H, it has been found that the dimensionless internal Froude number, $F_r = V/NH$ where V represents the constant initial speed of propagation of heavy gravity currents, was independent of the length of the lock and is a logarithmic function of a parameter R = (ρ_c-ρ_0)/(ρ_b-ρ_0), except at small values of h/H and R close to unity. This parameter R, was one possible measure of the relative strength of the current (ρ_c-ρ_0) and stratification(ρ_b-ρ_0). The distance propagated by the current before this constant velocity regime ended (Xtr), scaled by h, has been found to be a unique function of Fr for all states tested. After this phase of the motion, for subcritical values of Fr, internal wave interactions with the current resulted in an oscillation of the velocity of its leading edge. For supercritical values, velocity decay was monotonic for the geometries tested. A two-dimensional numerical model incorporating a no-slip bottom boundary condition has been found to agree with the experimental velocity magnitudes to within 1:5%.

In 1994 Huppert & Woods studied the motion of instantaneous and maintained releases of buoyant fluid through shallow permeable layers of large horizontal extent which was described by a nonlinear advection-diffusion equation. The similarity solutions of this equation are describe the release of one fluid into a horizontal porous layer initially saturated with a second immiscible fluid of different density. Asymptotically, a finite volume of fluid has spreaded as $t^{1/3}$. On an inclined surface, in a layer of uniform permeability, a finite volume of fluid have propagated steadily along slope under gravity, and spreaded diffusively owing to the gravitational acceleration normal to the boundary, as on a horizontal boundary. However, if the permeability varies in this cross-slope direction, then, in the moving frame, the spreading of the current eventually becames dominated by the variation in speed with depth, and the current length have increased as $t^{1/2}$. They showed that if the porosity increases or decreases with distance from the boundary, then, in the long-time asymptotic limit, a discrete release of fluid will tend to generate a discontinuity at the nose or tail of the flow respectively. Shocks developed either at the leading or trailing edge of the flows depending upon whether the permeability increased or decreased away from the sloping boundary. Finally they have considered the transient and steady exchange of fluids of different densities between reservoirs connected by a shallow long porous channel. Similarity solutions in a steadily migrating frame described the initial stages of the exchange process. In the final steady state, there was a continuum

of possible solutions, which may include flow in either one or both layers of fluid. The maximal exchanged flow between the reservoirs involved motion in one layer only. They have confirmed some of our analysis with analogue laboratory experiments using a Hele-Shaw cell (Huppert & Woods 1994).

In 2007, Huppert & Takagi studied Newtonian viscous gravity currents propagating along horizontal and inclined channels with semicircular and V-shaped boundaries. They obtained the similarity solutions from the governing mathematical equations and they compared with closely matching data from laboratory experiments in which the propagation of glycerine along different channels was recorded. They discussed the resultsof geological applications (lava flows down the flanks of a volcano). Based on the concept of viscous fluid. They came up with different mathematical relationships that they had obtained between propagation distance and time by looking at different confining boundaries. At the instantaneous release of a fixed volume of fluid into a semicircular cross-section, the propagating distance scales was $t^{1/4}$ for non-inclined and $t^{3/7}$ forinclined channels, regardless of the angle of inclination. For V-shaped boundaries, the distance scales was $t^{2/7}$ for non-inclined and $t^{1/2}$ for inclined channels, again independent of the angle of inclination. These scalings hold independently of the angle at the vertex. they have noted that the results significantly differ from two-dimensional and axisymmetric geometries in the horizontal, where propagation distance scales like $t^{1/5}$ and $t^{1/8}$ respectively (Huppert 1982a). Two-dimensional flows down a slope propagate like $t^{1/3}$. They concluded that the results they obtained were very consistent with (Naranjo & al.1992 and Huppert & Takagi 2007).

In 2000 Huppert & Ungarish analyzed the behaviour of an inviscid, lock-released gravity current which propagates over a horizontal porous boundary in either a rectangular or an axisymmetric geometry by both shallow-water theory and box-model approximations. They solved the one-layer shallow-water equations for this problem, and they pointed out the differences with the classical current (over an impermeable boundary). It was showed that the effect of the porous boundary could be incorporated by means of a parameter λ which represents the ratio of the characteristic time of porous drainage τ to that of horizontal spread $x_0 = (g'h_0)^{1/2}$ where x_0 and h_0 where the length and height of the fluid initially behind the lock and $g' = g\Delta\rho/\rho_0$ was the reduced gravity. The value of τ is assumed to be known for the fluid-boundary combination under simulation. The interesting cases correspond to small values of λ, otherwise the current has drained before any signicant propagation can occur. Typical solutions were presented for various values of the parameters, and differences to the classical current (over a non-porous boundary) are pointed out. The results were consistent with the experiments in a rectangular tank (Thomas & al.1998), but a

detailed verification, in particular for the axisymmetric geometry case, requires additional experimental data (Huppert & Ungarish 2000).

Nsom& al. (2019) comparatived the influence of the initial and geometrical conditions on dam-break flow. The conditions were including the reservoir still water level, length and width as well as tail-water depth on dry and wet beds, respectively. The free surface evolution was analyzed through the volume of fluid (VOF) method. The sensitivity to mesh resolution and turbulence closure models were evaluated in three cell sizes and four models, respectively namely k-ε, k-w, RNG (RANS models) and LES. Likewise, the turbulence closure models namely Reynolds averaged Navier-Stokes (RANS) and large eddies simulation (LES) were compared with the previous experimental data. The LES showed relatively better agreement than other ones on the free surface evolution. The results declared the crucial role of the initial and geometrical conditions on the free surface progression, flow energy, outflow and inflow hydrographs and the resultant forces. The researchers reached the following important results: (1) Raising the dam reservoir water level causes an increase the free surface height, the advancing distance and the flow velocity. Likewise, it leads to increase the downstream specific energy; the outflow maximum depth and the hydrograph; the resultant shears and pressure forces. Whereas, it leads to relative decline of the Froude number in the middle to last stages. (2) Raising the reservoir length leads to attenuate the dam-break Froude number during the middle to last stages. However, it causes an increase the free surface height; the outflow maximum depth and the hydrograph during the middle to last stages. Nevertheless, it does not affect the downstream specific energy. Further, it leads to raise the resultant shears forces in the dam reservoir. (3) Increasing the reservoir width does not affect the free surface height; the advancing distance and the flow velocity; the temporal variations of the dam-break Froude number; the reservoir outflow depth as well as the downstream specific energy. However, it increases the dam outflow rate, the resultant shears and pressure forces. (4) Increasing the tail water level reduces the flow velocity during the initial to the middle stages. Further, it leads to increase the free surface height; the free surface fluctuations in the jet body region as well as the maximum depth of the dam reservoir outflow. In return, it causes an attenuate in the outflow hydrograph and the resultant shears and pressure forces (Nsom & al. 2019).

In (2015) Kowal & Worster presented a theoretical and experimental study of viscous gravity currents lubricated by another viscous fluid from below (golden syrup lubricated by dense potassium carbonate solution). Lubrication theory have been used to model both layers as Newtonian fluids spreads under their own weight in two-dimensional and axisymmetric settings over a smooth rigid horizontal surface and consider the limit in which vertical shear provides the

dominant resistance to the flow in both layers. There were contributions from Poiseuille-like flow driven by buoyancy and Couette-like flow driven by viscous coupling between the layers. The flow is self-similar if both fluids are released simultaneously, and exhibits initial transient behaviour when there is a delay between the initiation of flow in the two layers. they have been solved for both situations and they showed that the latter converges towards self-similarity at late times. The flow relied on three key dimensionless parameters relating the relative dynamic viscosities, input fluxes, and density differences between the two layers. Provided the density difference between the two layers was bounded away from zero, they were found an asymptotic solution in which the front of the lubricant is driven by its own gravitational spreading. There was a singular limit of equal densities in which the lubricant no longer spreads under its own weight in the vicinity of its nose and ends abruptly with a non-zero thickness there. They explored various regimes, from thin lubricating layers underneath a more viscous current to thin surface films coating an underlying more viscous current and find that although a thin film does not greatly influence the more viscous current if it forms a surface coating, it begins to cause interesting dynamics if it lubricates the more viscous current from below. They found experimentally that a lubricated gravity current is prone to a fingering instability where fingering instability develops at late stages of thier experiments, with lobes of highly lubricated, thin regions of high viscosity fluid becoming separated from the less lubricated and less mobile regions of deep, high viscosity fluid, also they have explored, theoretically and experimentally, the fundamental dynamics relevant to the flow of lubricated ice streams and extended the study to a broader range of fluid mechanical situations, and they concluded that the results they obtained from conducting the experiments were in agreement with the theoretical results (Kowal & Worster 2015).

By asking whether the instability is an internal instability, arising from internal dynamics or a frontal instability, arising from viscous intrusion. In (2019) Kowal& Worster examined the origin of the instability. They found it was the latter (frontal instability) and characterize the instability criterion in terms of viscosity difference or, equivalently, the jump in hydrostatic pressure gradient at the intrusion front. The mechanism of this instability was similar to, but contrasts with, the Saffman-Taylor instability, which occured as a result of a jump in dynamic pressure gradient across the intrusion front. They focused on the limit in which the two viscous fluids are of equal density in which a frontal singularity arising at the intrusion, or lubrication front becomes a jump discontinuity and perform a local analysis in an inner region near the lubrication front, which they matched it asymptotically to the far field. They also investigated the large-wavenumber stabilization by transverse shear stresses in two dynamical regimes: a regime in which the wavelength of the

perturbations is much smaller than the thickness of both layers, and an intermediate regime, in which both vertical and horizontal shear stresses are important.

Linear stability analyzes of lubricated viscous gravity currents in the internal region showed that the steady flow is unconditionally stable and suggests that the instability observed in experiments was a frontal instability. The latter analysis explained the mechanism of instability by exploring three physical scenarios. The first scenario has occured for wavelengths much larger than the thicknesses of the two layers. Analytically, they derived an asymptotic solution for the growth rate of the perturbations as an outer, large-wavenumber limit, which showed that the growth rate σ of the perturbations grows linearly with the wavenumber k as $k \rightarrow \infty$. Also they showed that jump in upper surface slope was positive (that is, the flow was stable) precisely when the viscosity ratio M= μ/μl (μ:Upper layer kinematic viscosity, μl: lower layer kinematic viscosity), between the two layers was less than one. By using a combination of asymptotic and numerical methods, they found that for the second scenario, involving perturbations resisted dominantly by horizontal shear stresses, the growth rate of the perturbations converges towards a constant rather than growing unboundedly. By considering the third scenario, they found that transverse shear was weakly stabilizing for intermediate wave numbers as well and that intermediate wave numbers are the most unstable at modest values of M (Kowal & Worster 2019).

Also in (2019) Kowal & Worster investigated the interaction between the mechanism of the instability and the stabilising influence of buoyancy forces by performing a global and fully time-based analysis, which does not use the frozen-time approximation. They determined a critical condition for instability in terms of the viscosity ratio and the density difference between the two layers. Instabilities were occurred when the jump in hydrostatic pressure gradient across the lubrication front was negative or equivalently, when the intruding fluid was less viscous than the overlying fluid, provided that the two fluids were of equal densities. Once there was a nonzero density difference, these driving buoyancy forces suppresed the instability for large wavelengths, giving rise to wavelength selection. As the density difference increases, the instability criterion has required higher viscosity ratios for any instability to occur, and the band of unstable wavenumbers became bounded. Large enough density differences suppresed the instability completely. And they concluded from the results they obtained that the flow became unstable precisely when the jump in hydrostatic pressure gradient across the lubrication front was negative (Kowal & Worster 2019).

Nsom & al. (2019) studied the linear stability of shear-thinning fluid down an inclined plane was investigated theoretically with application to chemical engineering (coating process) and environmental engineering (debris flow impact). The following four issues were tackled in this paper: (1) Build an equation of Orr-Sommerfeld type associatedwith appropriate boundary conditions. (2) Solve the generalized Orr-Sommerfeld equation. (3) From this solution the wave velocity was derived. (4) From this solution, derive Effect was extracted (stabilizing or not) of the different forces acting on the flow. The power-law modelwas used to describe the fluid rheological behavior. A linear stability analysis was brought out for building a generalized Orr-Sommerfeld model with appropriate definition of non-dimensional numbers in order to overcome the inconsistency of the existing shallow-water models. At first order, the effect of the different forces acting on the flow has been pointed out. It was particularly shown that pressure and surface tension have a stabilizing effect, while inertia and rheo-fluidification have a destabilizing effect. Moreover, the relative variation of critical Reynolds number increases with increasing reduced wavenumber for all values of slope tested while it decreases with increasing power-law index for all values of reduced wavenumber tested (Nsom & al.2019).

Holmboe instability is an instability of an unbounded stratified parallel shear flow to the development of cusplike waves that propagate with phase speed along the flow direction significantly different from the speed of the inflection point of the shear. In (2005) and in his tagged article, ' On Holmboe's instability for smooth shear and density profiles', Alexakis presented a study of the linear stability of a stratified shear flow for smooth density profiles. The work focused on the nature of the stability boundaries of flows in which both Kelvin–Helmholtz and Holmboe instabilities were present. For a fixed Richardson number, the unstable modes were confined to finite bands between a smallest and a largest marginally unstable wave number. The researcher observed a deep connection between the free gravity wave spectrum and the Holmboe unstable waves. The results indicated that the stability boundary for small was comprised of neutral modes with wave numbers phase velocity equal to the maximum/minimum wind velocity whereas the other stability boundary, for large wave numbers, was comprised of singular neutral modes with phase velocity in the range of the velocity shear. He showed how these stability boundaries could be evaluated without solving for the growth rate over the entire parameter space as was previously done. The researcher showed how these modes can be determined without solving the full eigenvalue problem for the complex eigenvalue c. The results indicated further that there was a new instability domain that has not been previously noted in the literature. The unstable modes, in this new instability domain, appeared for larger values of the Richardson number and are related to the higher harmonics of the internal gravity wave spectrum (Alexakis 2005).

Khoshkonesh and al. (2021) compared numerical results for SWE and 3DNavier Stokes models in the dam-break phenomenon. The study was to specify the capability of SWE and 3D Navier Stokes models in reconstructing the instantaneous dam-break phenomenon. The numerical simulations were implemented by a CFD software. The results showed that SWE model had lower accuracy, in reproducing the wave evolution and bed deformation, compared to the 3D Navier Stokes model. Furthermore, the kinematic and dynamic properties of the dam-break wave were affected by the initial conditions and bed characteristics. The researchers concluded that, the 3D Navier Stokes models, and LES amongst them, had highest accuracy in reproducing the free surface evolution and bed deformations compared to the SWE model. Furthermore, the 3D models need lower computational efforts in reproducing this phenomenon (Nsom& al.2019).

In (2005), EAMES&al., studied the influence of an external laminar flow on the spreading of a viscous gravity current moving over a horizontal floor theoretically and experimentally. The viscous stress exerted by the ambient flow drives the viscous gravity current streamwise with a velocity proportional to the local height of the current. The one-way coupling between the ambient flow and the spread of the current was examined. The underlying equations developed by coupling mass continuity and momentum equations were reduced to a similarity form and applied to study viscous gravity currents generated by line and point sources. Similarity and numerical solutions were developed to describe viscous gravity currents spreading from line and point sources. An experimental study of the spreading of viscous gravity currents issuing from a point source in a channel flow, for both constant-flux and instantaneous releases, confirmed the essential character of this description. The researchers concluded that there is a new agreement between the experimental and theoretical data obtained (EAMES & al.2005).

Mathunjwa&Hogg in 2006 generalized the linear stability analysis of the axisymmetric self-similar solution of gravity currents from finite-volume releases to include perturbations that depend on both radial and azimuthal coordinates. They showed that the similarity solution was stable to sufficiently small perturbations by proving that all perturbation eigenfunctions decayed in time. They established that the self-similar solution is linearly stable to disturbances that involve both radial and azimuthal dependences by proving that all eigenvalues have negative real parts. Moreover, asymmetric perturbations were showed to decay more rapidly than axisymmetric perturbations in general. An asymptotic formula for the eigenvalues were derived, which indicates that asymptotic rates of decay of perturbations were given by $t^{-\sigma}$ where $0< \sigma < 14$ as the Froude

number decreases from $\sqrt{2}$ to 0. They demonstrated that this formula agreed closely with numerically calculated eigenvalues and, in the absence of azimuthal dependence, it reduces to an expression that improves on the asymptotic formula obtained by Grundy & Rottman (1985). For two-dimensional(planar)currents, they further proved analytically that all perturbation eigenfunctions decay like $t^{-1/2}$ (Mathunjwa & Hogg in 2006).

In 1985, and in‘ The approach to self-similarity of the solutions of the shallow-water equations representing gravity-current releases‘ Grundy& Rottman studied similarity solutions of the shallow-water equations representing the motion of constant-volume gravity currents in both plane and axisymmetric geometries. They found that these solutions were linearly stable to small correspondingly symmetric perturbations and that they constitute the large-time limits of the solutions of the initial-value problem. Furthermore, the analysis revealed that the similarity solution has been approached in an oscillatory manner. Two initial-value problems have been solved numerically using finite differences and in each case the approach to the similarity solution was compared with the analytic predictions (Grundy and Rottman1985).

Thomas&al. (2004) studied the motion of a dense fluid that develops as an inertial gravity current of decreasing mass above a horizontal porous bed. The flow is described by Darcy’s law which states that the flow rate at any point in the reservoir is given by the fluid pressure gradient, the viscosity of the fluid, and its effective fluid permeability. Laboratory experiments were carried out in which fixed volumes of salt water were released from behind a lock with an impermeable bottom into a large rectangular crosssection channel containing fresh water. The current were flowing over a thick permeable layer, which was initially saturated with fresh water. As the salt water penetrates the bed, it drives the fresh water downwards in the bed, and out through the bottom. Measurements were presented of the gravity current and related to the loss of salt water from the current. From the set of laboratory experiments performed, they obtained measurements of the mass and the front position of the current by changing different parameters were presented. The results were explained by means of a global analytical model that suggested practical correlations combining the parameters. Thus, previous experimental, numerical and theoretical findings have extended to describe lock-release gravity currents above more realistic porous beds. They have presented a model to describe the flow of the current in terms of a local Froude number at the front, and a global mass balance suggesting an analytical approximation to extended currents over thick porous layers: the mass evolution does not depend on the height profile, mixing, Froude number at the front, details of the beginning of the flow including the evolution of the bore, and the initial fractional depth of the dense fluid. For a better comparison between the loss of fluid from the

current and the laboratory results, they introduced a simple correction through an integral model with proper initial conditions and F function, and achieving a good agreement. In addition, the current decelerate as the driving pressure was reduced because of the current thinning due to the sinking (Thomas & al. (2004)).

NSOM & al.2008 presented a paper dealt with the dam-break problem in a horizontal smooth 1D channel, for hydrogeological hazards purpose. The fluid is muddy and It has been described as Newtonian model, provided that the inertial effects be neglected versus the viscous ones in the momentum balance. Assuming the shallow water approximation, a non dimensional equation was built from the continuity and the Navier-Stokes equations in the limit of zero-inertia and solved analytically in two limits: short time and long time. These solutions were then combined into a single, universal model. Limitations of the model were examined by comparison to a converged finite difference numerical solution of the flow equation. The results of the researchers showed that there is agreement between numerical and analytical solutions through the consistency of the numerical scheme for both short time and long time solutions. The time evolution of the abscissa and velocities of the different front waves were determined, as well as the different characteristic heights (NSOM & al.2008).

Zhu & al.(2004) performed experiments for lock release gravity currents in a rectangular channel with salt water and fresh water. The spreading law of the salt water was validated by using a digital video to record the progress of the current. Detailed instantaneous velocity structure of lock release gravity currents in the slumping phase was studied experimentally with particle image velocimetry (PIV). The time variation of the spatial distribution of velocity and vorticity was obtained, which shows some qualitative characters of the current as well as the effects of the bottom boundary layer and upper mixing layer. The results showed that the horizontal velocity increased gradually from the end of the tail to the current head, reached its maximum value under the maximum depth of the head, and then decreased till the foremost point of the current. Two obvious vorticity strips were seen at the interface of the two fluids and near the rigid bottom boundary, respectively. Eddies formed at the rear of the gravity current head because of velocity shearing and flow separating. The dense fluid was supplied from the center of the head to the leading edge and it was entrained away mainly by the upward ambient fluid and slightly by the downward ambient fluid. The horizontal velocity profiles in the gravity current head were shown, and the depth of the bottom boundary layer was estimated, which validates that the negative vorticity is concentrated in the boundary layer (Zhu & al.2004).

Zemach (2018),and in'Asymptotic similarity solutions for particle-driven gravity currents in non-rectangular cross-section channels of power-law form. He considered a high-Reynolds particle-driven gravity current (GC) propagating in channel above a horizontal boundary. The bottom and the top of the channel were at z = 0, H and it was cross-section is given by $-f(z) \le y \le f(z)$ for $0 \le z \le H$, where f (z) was a power-law function $f(z) = z\alpha$. he focused on the similarity stage of propagation of the current using a shallow-water (SW) model. While it was possible to derive the analytical similarity solutions for the homogeneous GC (for which the density of the current remains constant during the propagation), such similarity did not exist for the particle-driven GCs. He extended the similarity solutions of homogeneous GC to particle-driven currents by developing an asymptotic expansion and derived approximations of such solutions for channels of typical rectangular, triangular and parabolic forms. Comparison with the numerical solution of the SW equations showed that the leading-order asymptotic results were a good approximation in the domain of expected validity. However, out of bounds of this domain the numerical solutions systematically departed from the first-order asymptotic solutions, suggesting the need to include higher-order terms in the asymptotic series. The conclusion he reached in his research was that the particles in the current slow down the speed of propagation (Zemach2018).

Shringarpure&al. (2013) In their tagged research 'Front conditions of high-Re gravity currents produced by constant and time-dependent influx: An analytical and numerical study'. In particular attention was focused on the front condition of the current which was characterized by the Froude number $F_{rN} = U_N/(\acute{g}h_N)^{1/2}$ (where U_N, h_N were the speed and the height of the front, and g′ is the reduced gravity). Following a procedure similar to the one given in (Benjamin 1968), they have showed that the front condition was significantly influenced by the position of the outflow boundary (i.e. by the direction of flow of the ambient fluid displaced by the current). An expression for the front Froude number (Fr_N) as a function of the depth ratio $a = h_N/H$, which took into account the direction of the ambient flow, was presented. Two limiting cases were considered: no-return ambient flow (when the outflow and inflow were at the opposite end walls) and full-return ambient flow (inflow and outflow on the same end wall). Theoretical considerations suggested that the propagation speed of the gravity current in the no-return configuration would been higher than in the classical full-return configuration of Benjamin. Navier–Stokes simulations of constant inflow currents in no-return configuration were carried out. Overall, the front Froude number (Fr_N) has evaluated from these simulations conforms to the analytical insights and it was predictions. Unsteady gravity currents were also simulated by implementing time dependent inflow boundary conditions. Two sets of simulations were carried out that represent accelerating and decelerating currents by implementing waxing (increasing in time) and waning (decreasing in time) inflow rates.

It was observed that the front Froude number (Fr_N) has evaluated from the simulations of unsteady fronts was in good agreement with the front Froude number of a steady front for comparable depth ratio. The conclusion they reached in his research: This results confirmed the prediction that the ambient flow direction can significantly influence the front condition of the current (Shringarpure & al.2013).

Ciriello& al. (2016) have developed a model to grasp the combined effect of rheology and spatial stratifications on two- dimensional non-Newtonian gravity-driven flow in porous media. They have considered a power-law constitutive equation for the fluid, and a monomial variation of permeability and porosity along the vertical direction (transverse to the flow) or horizontal direction (parallel to the flow). Under these assumptions, similarity solutions were derived in semi-analytical form for thin gravity currents injected into a two-dimensional porous medium and having constant or time-varying volume. The extent and shape of the porous domain affected by the injection was significantly influenced by the interplay of model parameters. These described the fluid (flow behaviour index n), the spatial heterogeneity (coefficients β, γ, δ, ω for variations of per- meability and porosity in the horizontal or vertical direction), and the type of release (volume exponent α). Theoretical results were validated against two sets of experiments withα=1(constant inflow) conducted with a stratified porous medium (simulated by superimposing layers of glass beads of different diameter) and a Hele-Shaw analogue for power-law fluid flow, respectively. In the latter case, a recently established Hele-Shaw analogy was extended to the variation of properties parallel to the flow direction. Comparison with experimental results were showed that the proposed model was able to capture the propagation of the current front and the current profile. Their study predicted the time dependence of the volume of subsurface domain invaded by the contaminant or reached by the remediation agent; the results might be useful for a quick evaluation or bench-marking of numerical models even when the real conditions differ moderately from model assumptions. Future extensions of the model might include the usage of more complex constitutive equation for the fluid, and an improvement in the description of spatial heterogeneity (Ciriello& al.2016).

Longo& Federico (2014) have presented a novel formulation to analyse the axisymmetric propagation of single-phase gravity currents induced by the release of a time-variable volume of fluid in a porous domain. Their approach has based on a first order expansion of the velocity potential that allowed for the presence of vertical Darcy velocities. Coupling the flow law with mass balance equations led to a PDE which admited a self-similar solution for the special case in which the volume of the fluid fed to the current had increased at a rate proportional to t^3. A numerical solution was developed for rate proportional to t^{α} with $\alpha \neq 3$. Current profiles obtained with the first

order solution have a finite height at the origin. Theoretical results were compared with two experimental datasets, one has included freshwater and the other air as an ambient fluid. In general, experimental current profiles had collapsed well onto the numerical results; the first order solution showed a marked improvement over the zeroth order solution in interpreting the current behavior near the injection point. A sensitivity and uncertainty analysis was conducted on both the first order and zeroth order theoretical model. The sensitivity analysis were indicated that the flow process was more sensitive to porosity variations than to other parameters. The uncertainty analysis of the present experimental data indicated that the diameter of glass beads in an artificial porous medium was the source of most of the overall uncertainty in the current profile. The researchers reached several important results, namely: (1) The solution was self-similar for $\alpha = 3$. (2) An extensive comparison of the zeroth and first order theoretical models with two sets of experiments was carried out, together with a statistical analysis of the uncertainties affecting model results and experimental data. (3) Profiles obtained with the first order solution have a finite height in the origin and depend almost linearly on the distance from the origin. (4) The effect of the correction was much less important for the radius of propagation, which in the first order solution always increases, albeit modestly, with respect to the zeroth order solution. (5) In general the sensitivity analysis indicates that porosity (directly affecting, with the diameter d, the intrinsic permeability) was the main source of uncertainty hence, in controlled experiments, a great deal of attention should be paid in reproducing the porous medium with uniform known porosity (Longo& Federico2014).

1.3 Experimental and numerical study of model GC in coastal environment

Release of pollutants into rivers, the oil spillage on the sea environment, and desalination plants outflow are examples of man-made gravity currents that frequently cause negative environmental impacts. In order to better understand the propagation dynamics and the mixing process of dense gravity currents, the following outstanding contributions have been in our lab (Institut de Recherche Dupuy de Lôme (IRDL) Laboratory of Brest University UBO), presented the results of a thorough experimental and numerical investigation on dense gravity currents models. The gravity currents prepared were salt/tap water solutions at assigned concentrations. They were released in the form of a jet into a calm lighter ambient liquid (fresh tap water in this case) over a flat, smooth, and rigid bottom in order to simulate the discharge of a denser fluid in the coastal environment. The importance of studying gravity currents in the laboratory is due to several reasons, including firstly, laboratory experiments are carried out in a more controlled environment than larger scale field experiments. This means that more data of higher quality can be collected. Secondly, the effect of each aspect of the flow can be carefully studied for a full understanding. Thirdly, experiments can easily be repeated, either with the same parameters or for a wide range of parameters. It should be

noted that, since the 1950's, the gravity currents have been studied widely in laboratory experiments, and the spreading of buoyant jets in calm, and stratified environment with a linear density has been the theme of consideration by many researchers, including Ahmed 2015 and 2017, the owner of this contributions.

1.3.1 Experimental study of the effect of the spreading buoyant gravity current on the coastal

An experimental study of the effect of the spreading buoyant gravity current on the coastal was reproduce in a rectangular basin by releasing the fresh water with density ρ and initial speed U_0 over a salty water surface with density $\rho+\Delta\rho$ at rest. The surface flow of light liquid horizontally was looked as a special case of a two dimensional gravity current. This study was dedicated to displaying the results of laboratory experiments the spreading law of the fresh water was validated by using image processing technique to record the progress of the injection current. The time evolution of was measured of the progress x, and the spreading y of the gravity currents. The jet fluid was colored and the digital video can have a variation of light intensity in order to obtain the shape of the outer boundary of the gravity current and its distance from the source point with relation to initial time, or flow parameters of the jet source. The experimental device setup consists of a transparent basin made Plexiglas (3m long, 0.49 m wide and 0.49 m deep) containing the static ambient liquid, of 700L. A reservoir of 60L equipped with a floodgate and which releases the gravity currents into the basin. As shown in Fig.1.7. A bowl of 240L used to prepare the ambient fluid by introducing the quantity of salt corresponding to the concentration needed into a given volume of water. The solution prepared (salty water) was then poured into the previous basin. An observation system consisted of one camera(type: Photron Fastcam) taking 190 images per second with a resolution of (1024x1024 Pixels) was used. The camera was placed 1m above the water surface of the basin. The pictures observed by the camera were captured at a frequency of 38 Hz owing to a system of image processing consisting of a PC equipped with a Pentium IV processor (2.6 GHz) of a 1024 Mb random-access memory.

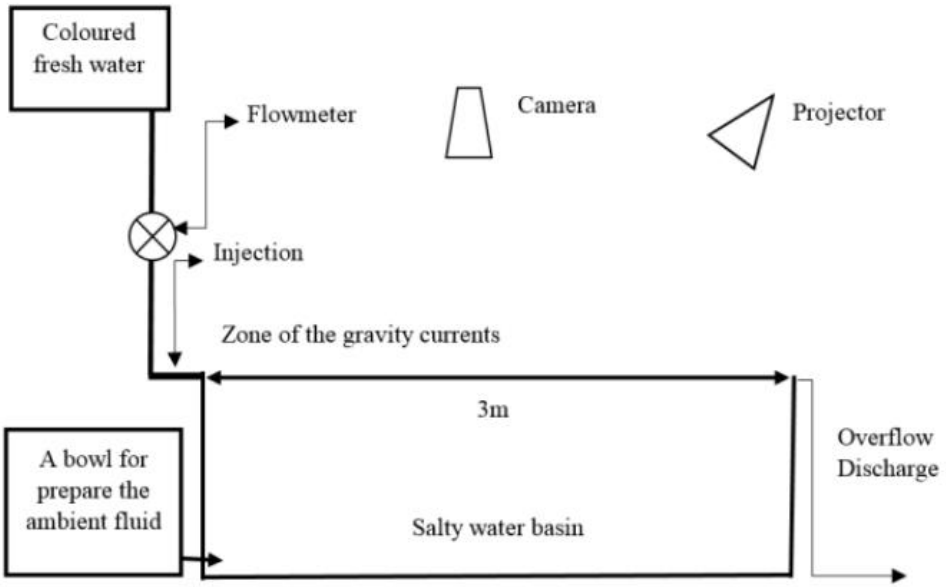

Fig.1.7. Schematic of the experimental setup

The experimental data collected come from visual method (e.g.visual technique measurements, red dye Rhodamine B), where the visualization was observed clearly by adding rhodamine B to the gravity current which can give the variation of the light intensity recorded by a camera. Also the red dye Rhodamine B was used to obtain the instantaneous images sequences of the saline gravity currents injection into the static fresh water. Recorded images were analyzed for extract the position of gravity current boundary. The image processing was based on the filtering of noise and binarization of image sequences as shown in Fig.1.8. and to exact the spatiotemporal interface position of the gravity current.

Fig.1.8. Image captured by a camera: (A) initial frame without flow Io, (B) frame with a colored gravity current flow, and (C) image obtained by difference and filtering processes.

After the captured video frames with current development have been subsequently converted into greyscale matries, in the region of the basin surface. They were converted into instantaneous density field as shown in Fig.1.9

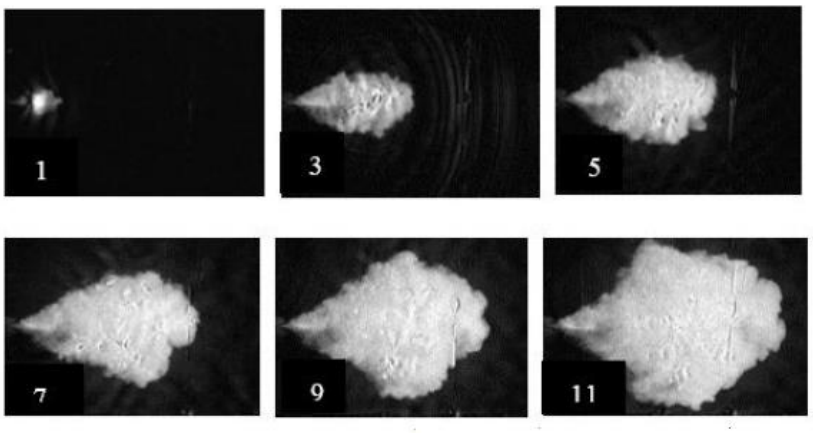

Fig.1.9 Snapshot of gravity currents obtained by image processing.

The techniques of image processing were complementary to characterize well experimentally the flow of gravity current. The two dimensions profiles of the gravity current showed that, the flow is non-axisymmetric and the shape of the outer boundaries of the gravity currents are nearly of elliptical form. The evolution of the front position showed a power law with time as shown in Fig.1.10 (a, b, c). A horizontal plane coordinate system (x; y), represented the outer boundary of injection current. An image analysis was applied to investigate the gravity currents developing over a horizontal free surface of the basin. Immediately after the injection of the lighter fluid in the basin, a gravity current was formed and the injection zone was depended on the flow rate. Through the injection process, the instantaneous front position x_f was estimated.

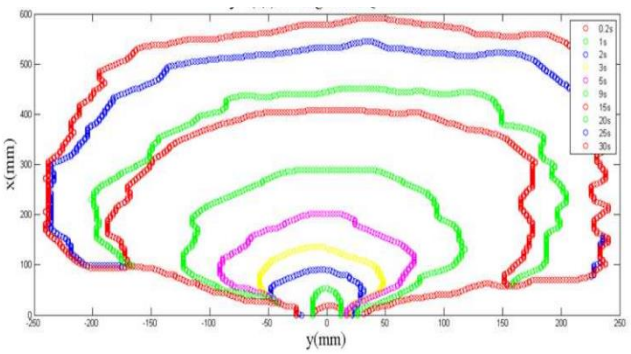

(a)

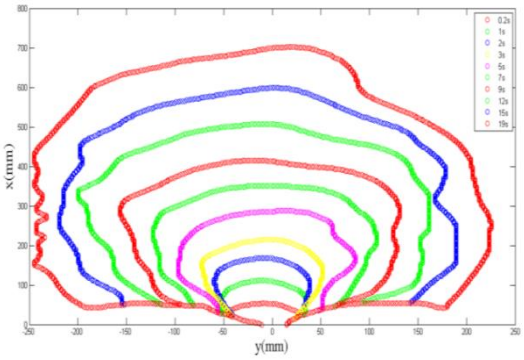

(b)

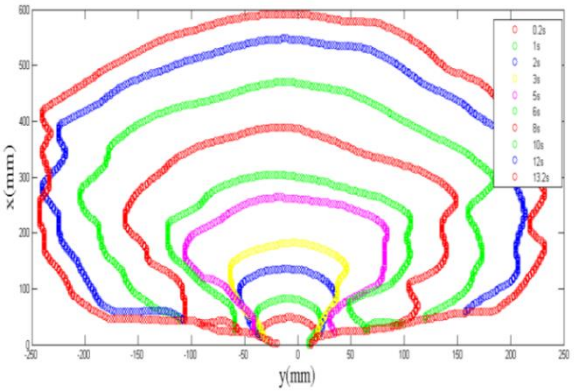

(c)

Fig.1.10 The profile of gravity currents outer boundary $y=f(x, t)$ for (a)Q= 30L/h (b)Q= 70L/h (c)Q= 110L/h.

Furthermore, the front of the two dimensional gravity currents were obtained by inconstant jet flow of fresh water. Through used the scaling law by appling the power fitting for measurements the exponents B and D (for $x = At^B$, $y = Ct^D$). It was found that B and D did not vary noticeably for all experiments. The exponents in a series of all experiments got the functional forms of the positions x and y together with time relationships and this led to the study of the variable spreading problem since the gravity current grows with time and the outer boundary variations as shown that in table 1.1.

Q	Re	Fr	**Spreading Law(x-direction)**	**Spreading Law(y-direction)**
30	481	0.36	$x=52t^{0.69}$ $[1.8 < t(s) < 18.6]$ $x=96t^{0.48}$ $[18.8 < t(s) < 30.2]$	$y = 64.6t^{0.67}$
70	3587	0.84	$x=68t^{0.63}$ $[1 < t(s) < 9.4]$ $x=91t^{0.56}$ $[9.6 < t(s) < 19.6]$	$y = 113t^{0.60}$
110	4434	1.32	$x=63t^{0.49}$ $[0.2 < t(s) < 2.6]$ $x=38.9t$ $[2.6 < t(s) < 11]$	$y = 90t^{0.70}$

Table1.1: Scaling laws obtained For The Spreading of Fresh water

Also they observed the variation of distances with time can see in Fig.1.11. (a ,b).

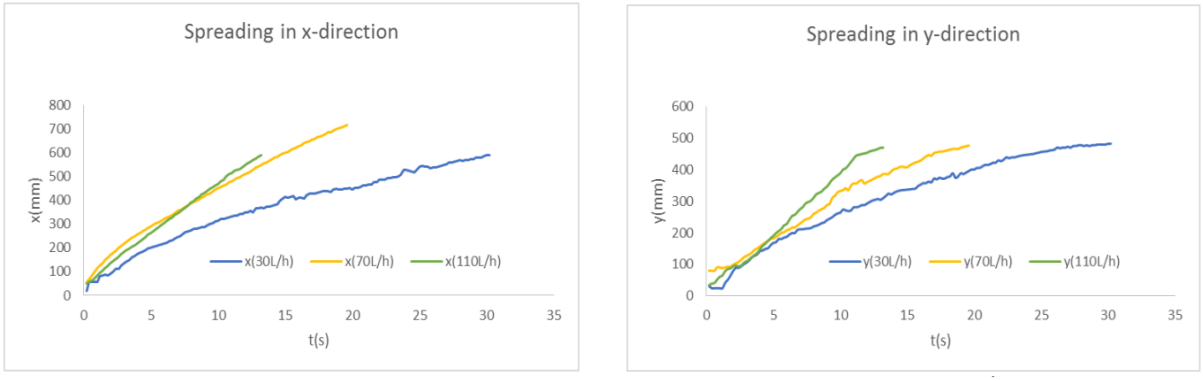

(a) (b)

Fig.1.11. Evolution of spreading front in (a) x-direction (b)y-direction**.**

This study is reached some conclusions, including: (1) For the initial Reynolds number and initial Froude number, which shown in table1.1, the alteration of flow regimes (which is any change in the natural flow regime of a river or stream) was in viscous regime $x \sim t^{0.6}$ approximately this confirmed experimentally by Britter (Britter1979). (2) The outer boundary of gravity current spreading on the salty water free surface was almost non-axisymmetric and the same thing for jet zone. (3) The front positions distances from the jet source to the outer boundary of the gravity currents were correlated with spatio temporal diagram and showing the balancing between buoyancy and, either drag (viscous spreading) or inertia. (4) By comparing the experimental results with Huppert1982, the front of the two dimensional gravity currents were obtained by a constant fresh water injection over the salty water surface basin.

1.3.2 Horizontal miscible jet propagation with positive buoyancy

Attention has been paid to a study of the spreading of a dense miscible jet (water salty) within a another less dense liquid (fresh water) on a rigid horizontal wall. In the presence of the difference in density between the fluid injected and the ambient fluid, the jets are driven by positive or negative buoyancy. In most previous studies, the authors have used the position of the forehead as an easily measured parameter. To test their theory which does not take mixing phenomena into account. The experimental setup consists of a rectangular basin containing a static ambient fresh water of 1.1cm^3 at H=5 cm. The dimensions of the basin are the following: L = 55 cm length, ℓ= 40 cm width, and H=5 cm depth. The walls of the basin are made of 5mm transparent glass allowing the visualization of the gravity current development. A tank with a capacity of 6 cm was used to prepare the salt fluid. The denser fluid is pumped to another tank with a capacity of 2 cm^3, where it was colored with Rhodamine B dye. The colored salt water was injected into the basin via a transparent plastic square channel at the horizontal bottom surface made of a smooth white plastic. The injection tube is a square channel with a length of d =0.5 cm, and it is kept horizontal for the duration of all the experiments. When the injection orifice opens instantly, the two fluids with different densities come in contact and a non-equilibrium condition occurs.

To describe the mixing of fresh and salt water, volume fraction transport equation was used, which took into account advection and diffusion. The volume fraction of salt water noted α_1 is equal to 0 in the region where there was onlyfresh water, and it was between 0 and 1 for the mixing zone. The volume fraction of water soft was determined as $\alpha_2=1-\alpha_1$ when α_1 was calculated. The equations of continuity and momentum were formulated by neglecting the interface tension force between the two miscible liquids. The averaged Navier-Stokes equations (RANS: Reynolds-Averaged Navier-Stokes) and that of the advection-diffusion of the volume fraction α1 of salt water were used to calculate the volume fraction α_1, the average speed ū and the pressure p.

Density was defined as $\rho = \alpha_1\rho_1 + \alpha_2\rho_2$, the effective viscosity $\mu_{eff} = \mu+\mu_t$,where μ was the dynamic viscosity and μ_t was the turbulent viscosity. The configuration studied was that of a salt water jet with a density of ρ_1=1040kg /m injected at the bottom of a freshwater basin of density ρ_2 =1000kg/m at constant initial flow Q0=U0.d2 with d = 5 mm the diameter of the square section of the injection channel (Fig.1.12). viscosities dynamics of the two liquids are respectively μ_1 =1.04.10 Pa.s for salt water and $\mu_2 = 1.10^{-3}$ Pa.s for fresh water.

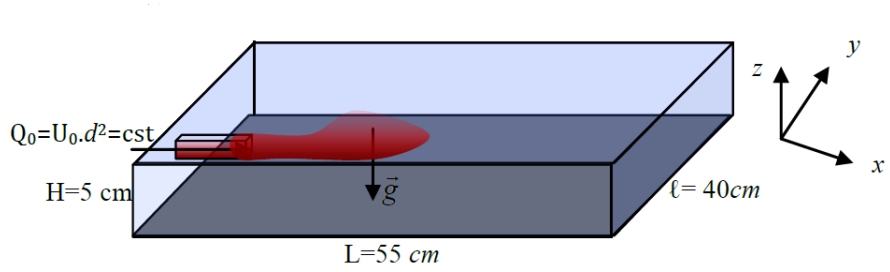

Figure 1.12 Configurations du jet horizontal miscible de flottabilité positive.

The twoLiquid Mixing solver has been used. BlockMesh has been taking used to achieve a structured and constant mesh (275x80x50) in the three directions without taking into account the symmetry of the problem. The numerical data were compared with the experimental data and it was found that there was a good and acceptable match between them.

Figure1.13. represents an example of the experimental and numerical jet spreading for a number initial Reynolds number of $Re_0= \rho_1 U_0.d/\mu_1 =2778$ which corresponds to an initial Froude number of $Fr_0=U_0/(g'd)=12.8$. The researchers found that the overall shape of the digital jet is similar to that observed in experiments. Instabilities at the interface of the front were observed unlike at the experimental jet. By comparing the position of the front of the experimental jet with that of the digital one in depending on the number of initial Reynolds Re_0 and the initial froude number Fr_0 (Fig.1.14), A delay of the digital jet far from injection was observed for low initial Reynolds number values Re_0 between 1111 and 2222 and Froude numbers Fr_0 between 5.1 and 10.2. This delay disappears for initial Reynolds values Re_0. Between 2500 and 3889 which corresponds to Fr_0. Between 10.5 and 18. Thanks to numerical calculations, it was possible to trace the variance of volume fraction of the jet as a function of time in the three directions (fig.1.13 on the right, fig.1.15). Near the injection the height of the jet can give a boundary allowing the distinction of the fresh water from the jet. On the other hand, far from the injection when the jet is well spread out, one cannot distinguish a clear boundary making it possible to distinguish the height of the jet α_1 (x, y, z, t). It is therefore a continuous evolution of the height of the jet.

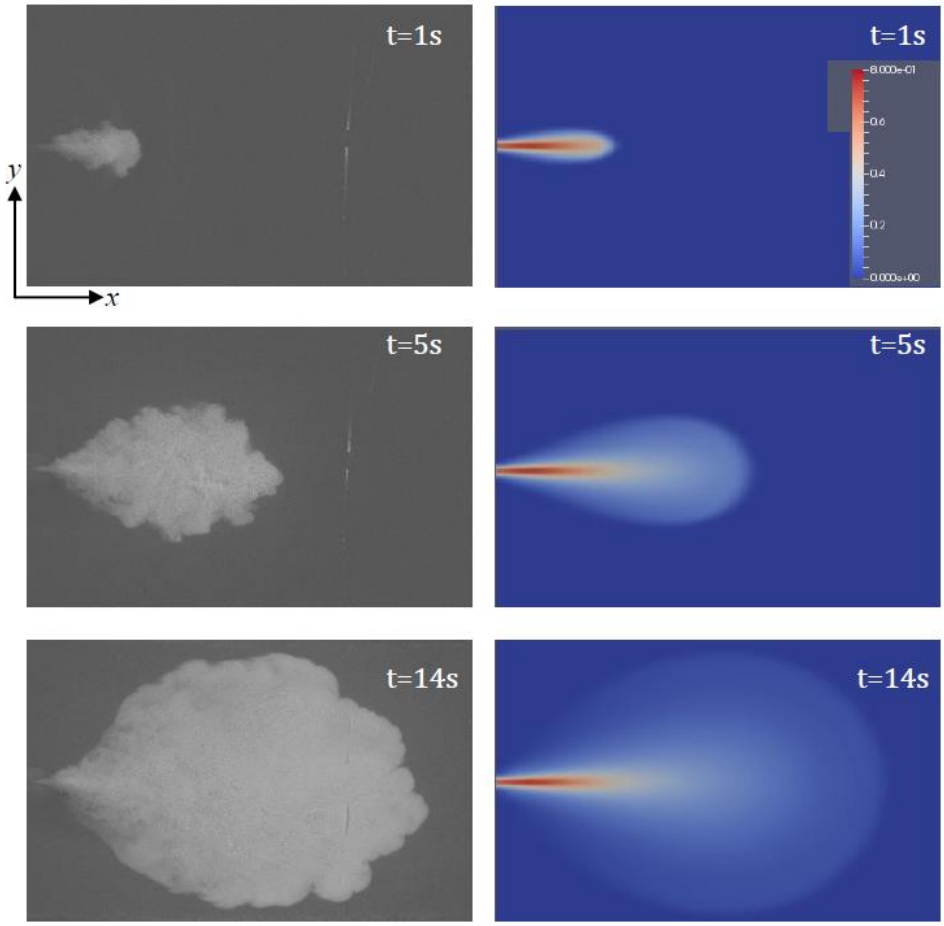

Figure 1.13: Miscible horizontal jet of positive buoyancy near the rigid wall at the bottom of the basin for Re0=2778 and Fr0=12.8; obtained experimentally on the left: images of the reflection of the light intensity I (x,y) of rhodamine B with time and numerically on the right: volume fraction of the mixture α1(x, z) with time.

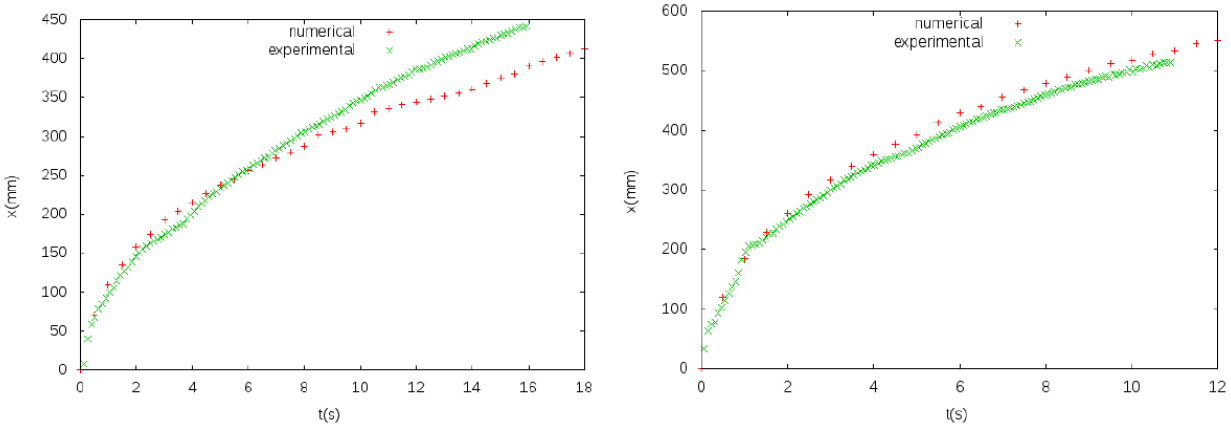

Figure 1.14. Comparison of the maximum axial position of the experimental and numerical jet front as a function of time: Re_0=1667 equivalent to Fr_0=7.7 (left) and Re_0=3889 equivalent to Fr_0=17.9 (right).

In Figure1.15. The evolution of the head of mixing gravity currents jet shows a head expansion and the disappearance of the density gradients throughout the gravity current development, which

occurs through deterioration of the current jet velocity far from the jet source, and finally fades away in time by diffusion processes.

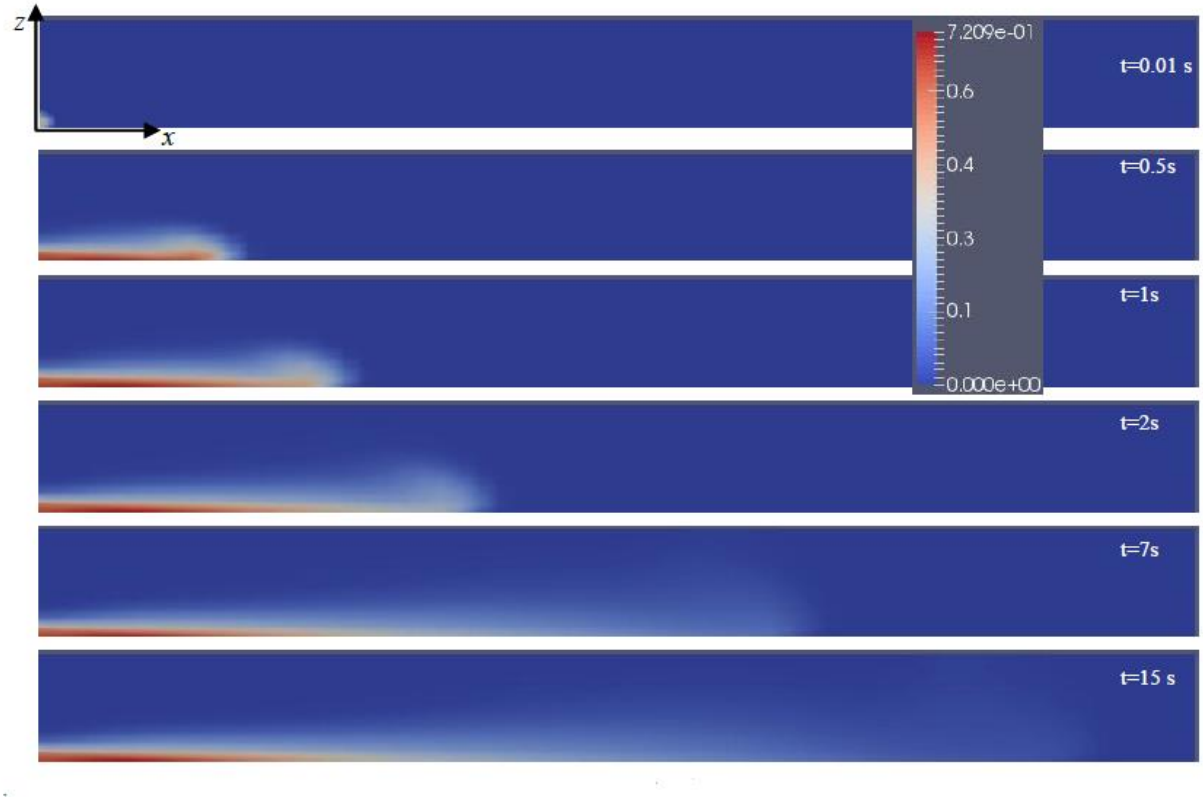

Figure 1.15 : Evolution of the volume fraction of the jet α1 (x, z) with time at y=0 for Re_0=2778; Fr_0=12.8.

1.3.3 Applied the large scale particle image velocimetry technique for measurement the velocity of gravity currents in the laboratory

This series laboratory experiments presented by Ahmed & al. (2015) was dedicated to investigate the gravity current of colored fresh water with density ρ-$\Delta\rho$, and initial speed u_0 upon the free surface of an ambient liquid (salty water) with density ρ at rest in a basin. Velocity flow measurement in laborator described by two steps: first: surface velocity measurement using particle image velocimetry (PIV) at the water surface, which is a measurement technique, that allows for capturing velocity information of the whole flow field in fractions of a second. This technique similar to large scale of particle image velocimetry (LSPIV). Second: Surface velocity measurements were made using particle image velocimetry, as well established technique in fluids research for laboratory flow measurement. We applied the image processing and the spatiotemporal diagrams technique in order to describe the time evolution of the progress x, and the spreading y of the gravity current. That means it is able to measure these two components which characterize the flow of the gravity current as a function of the flow rate and salinity (Froude number). These experiments shed light on some phenomena like the dominant flow and transport phenomena in the presence of river, stream and wetland ecology, stream corridor restoration, in the case of accidental pollution spills.

The experiments were conducted in a dark laboratory room to a void other light sources disturbing the experiments. The experimental device setup consists of an injection channel (600 mm long and 17 mm wide) manufactured in transparent glass and which links the reservoir to the basin. A transparent basin made from Plexiglas, containing the static ambient liquid, of 700 L (300 cm long, 49 cm wide and 49 cm deep). A reservoir of 60 L equipped with a floodgate and which releases the gravity currents into the basin.A bowl of 240 L used to prepare the ambient fluid by introducing the quantity of salt corresponding to the concentration needed into a given volume of water. The solution prepared (salt water), then poured into the previous basin. A light source made of 500 w (50 Hz) projector was placed ahead of basin to provide reflection of light source as shown in the figure:

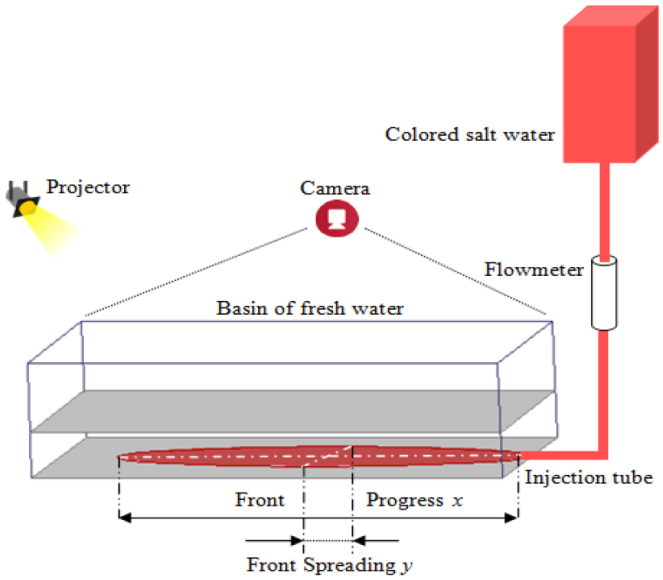

Figure1.16 Schematic of the experimental setup

An instrumentation equipment included: an observation system consisting of one SONY CCD XC-ST51/ST51CE camera equipped with a resolution of 768 × 576 pixels. The system of image capturing which consists of a PC equipped with a Pentium IV processor (2.6 GHz) of 1024 Mb of random-access memory and provided with a Matrox Meteor II multi-voice at 8 bits smart card. The images observed by camera was simultaneously captured at a frequency of 25 Hz or 50 Hz.

In the (PIV) technique, the small quantity of Rhodamine B colouring agent as a tracer was introduced for video-photographic analysis purpose. In testing the density and the viscosity of these gravity currents, it was observed that the addition of Rhodamine B does not modify the physical properties of the gravity current. Then the LSPIV technique has been used which provided the reliable measurements of velocities with acceptable accuracy. In this case, the solid particles used in classical PIV were replaced by an inert colouring agen (e.g. Rhodamine B), which was introduced in the gravity current injected in the ambient fluid. The difference between the light intensities of the two liquids was observed on the images and their respective motions could be followed and analyzed using the time elapsed between two consecutive images. The differences in light intensity between the two methods caused by the intrusion level of the gravity current were compared. The inter correlation algorithm has been used to compute velocity (Figure1.17a, b) and vorticity (Figure1.17 b) as shwon

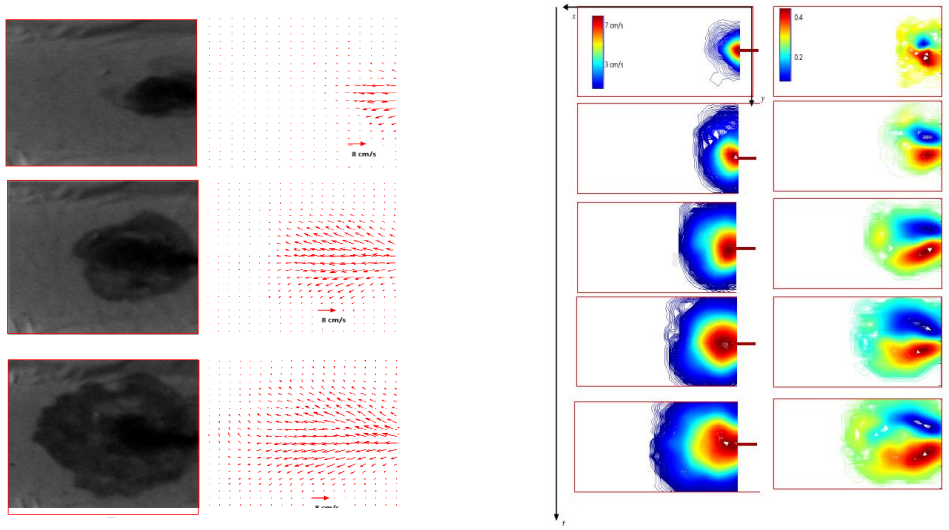

(a) (b)

Figure1.17(a)Spatio-temporal evolution of velocityfor increasing concentration in salt: *Cs* = 10g/Lang, Fr= 0.71. (b) Spatio-temporal evolutions of velocity (left) and of vorticity (right) for *Cs*=10g/Lang Fr = 0.71.

Both axial velocity U(x, 0) and the lateral velocity V(x, 0) have been plotted as shown :

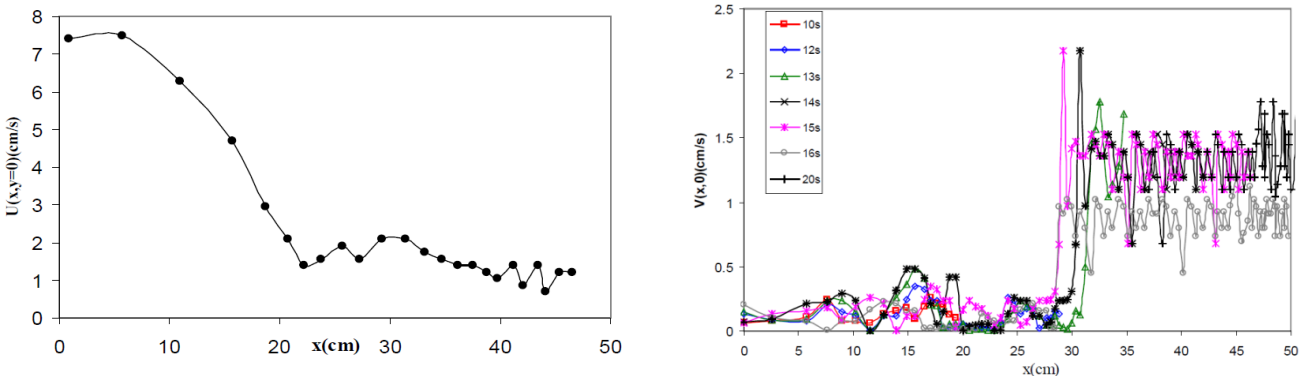

Figure1.18 : Variation of the velocity with the axial direction at y = 0 of (a) axial component U(x,0) and of (b) lateral component V(x,0) for $\Delta\rho/\rho$ = 0.0196: Re = 3587: and Fr = 0.97.

It was noted that the axial velocity U(x, 0) (Figure1.18(a)) was almost constant close to the injection channel. It was explained by the presence of the inertia regime when the progress of the front was linear with time. While far from the injection channel, the axial velocity decreased strongly with axial direction to it becomes 1 cm/s at the distance of 45 cm. It was explained by the establishment of the viscous regime. In the other hand, the lateral velocity V(x, 0) was very small at y = 0 in axial direction near the injection channel, while far from the injection, even the lateral velocity was small but it was of the same order than the axial velocity. This has been interpreted as near the injection channel, the flow was one dimensional in x-direction where the vorticity was very small or vanishing. Far from the injection channel, the free surface flow has followed a two dimensional propagation where the vorticity was not vanishing with a weak asymmetry with respect to the axis of the injection channel (Figure1.18(b)).

Both the axial velocity U(0, y) and lateral V(0, y) at fixed axial direction(x = 0)have been plotted as shown :

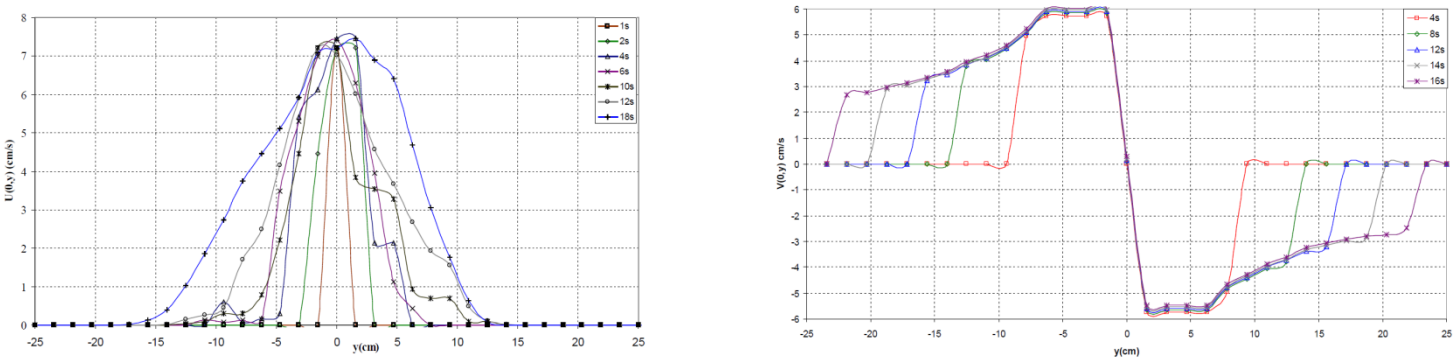

Figure1.19 Variation of the velocity with the axial direction at x = 0 of (a) axial component U(0,y) and of (b) lateral component V(0,y) for *Cs* = 10 g/L, and Fr = 0.71.

It was noted that the axial velocity direction U(0,y)(Figure1.19(a)) was maximal close to the injection channel and it decreased strongly with y. The lateral velocity V (0,y) vanished at the injection channel and then it became maximal. The lateral velocity V(0, y) decreases strongly with y (Figure 1.19(b)).

The study concluded: (1) Image processing technique has been proved for use in flow velocity measurement because of the initial evaluation of the feasibility of making flow surface measurements. (2)The characterization of flow was made by measurement of the velocity field and vorticity field using a large scale PIV technique.The image processing to estimate the surface velocity field with the LSPIV techniques. (3) Surface LSPIV measurements showed that the diffusion of dissolved tracer (Rhodamine B colouring) into the mixinglayer and the method involves surface velocity field injection estimation, and using initial flow parameters analysis as Froude Number.

1.4 Synthesis of numerical work - Issue and numerical project of this thesis

1.4.1 Synthesis of numerical work

Many previous numerical studies looked at gravity currents, and the results obtained had the greatest impact in providing a lot of information about this phenomenon. The following is a summary of the most important research work and its results, which are closely related to this thesis.

In (2018) Lam &al.presented direct numerical simulations (DNS) of two-dimensional stratified gravity current using OpenFOAM. The two-dimensional stratified gravity currents were simulated with the solver twoLiquidMixingFoam. The numerical data: the streamwise length Lx=20, the wall-normal length Ly=4. The step length $\Delta x \approx 0.0078$ and $\Delta y \approx 0.0156$. The purpose of the study was to investigate the effects of the initial aspect ratio and the stratification. Different aspect ratio were simulated like the ratio of the height of the dense fluid to the length of the dense fluid (h0/l0), with stratification ranging from S=0 (homogenous ambient) to S = 0.2. The Reynolds number (Re) of 4000 was used for all simulations. The magnitude of the stratification ($S=\varepsilon b/\varepsilon$) has been determined by calculating the reduced density differences of the bottom fluid with the ambient fluid ($\varepsilon b = (\rho b-\rho 0)/\rho 0$) and the dense fluid with the ambient fluid ($\varepsilon = (\rho c-\rho 0)/\rho 0$, where ρc represents the density of the dense fluid, ρb was the density at the bottom of the domain and $\rho 0$ is the density at the top). The analysis of contour has been used to compare the flow structure of weak stratified (S= 0.2) gravity current with non-stratified (S=0) gravity current. The front location of the gravity was reduced as the stratification increase and denoted that the front velocity of the gravity current was reduced by the stratification. They noted Kelvin-Helmholtz (K-H) billow formed behind the gravity current head. The simulation was validated with a test case from (Birman&al.2007) and he results were satisfactory (Lam &al.presented 2018).

Hydrodynamic characteristics of lock-exchange flow in curved channels in the presence of blocks were reported by Hamzenejad&al. (2020), where a rigid barrier was placed inside a curved channel with a curvature of 120 degrees and a radius (R) of one meter. It should be noted that the presence of a block within curved channels can cause new phenomena. Simulations were performed using the OpenFoam open-source software and the realizable k-epsilon turbulence model. They used twoLiquidMixingFoam, multiphase solver. This solver was based on the Volume of Fluid (VOF) method. The Reynolds number (Re) of 19700 was used for all simulations. The blocks were placed at 60 degrees of the curve. With an impediment, the secondary current was visible in the body and tail of the current but did not occur in the current head. They observed that the pattern of the secondary currents was different around the block from the other locations and the barrier also

reduced the spanwise velocity of the flow body. The current head was also affected by the block. The results showed that during the collision with the obstacle, the current slows down, and the nose of the current on the outer bank is overtaken by centrifugal forces on the external bank, and finally, it continues its path at a constant velocity as before the obstacle (Hamzenejad&al.2020).

Pelmard&al. (2018) investigated the influence of the grid resolution on the large eddy simulation (LES) (which is a mathematical model for turbulence used in computational fluid dynamic) of a lock-exchange turbidity current. The present work aimed at quantify the effect of grid resolution on the turbulence characteristics for currents with buoyant Reynolds numbers. The simulations were performed using a finite volume Boussinesq code(Finite volume schemes for Boussinesq type equations) with a Smagorinsky turbulence model(which is a model used for subgrid-scale for LES) for a range of buoyancy Reynolds numbers, ranging from transitional currents(Re_b= 1,0 0 0) to fully-developed turbulence (Re_b=60, 0 0 0). The general features of the flow and the relative independence of the current front for Re_b > 10, 0 0 0 were correctly predicted. The spanwise two-point correlations (which is employed to compare various shapes) were found to be the most useful quantities to assess the mesh resolution. In addition, velocity power spectrum densities were used to provide information on the maximum cell size required to ensure the LES filter cutoff wave length it was found inside the inertial range of the turbulence spectra. They showed that at low Reynolds numbers, the turbulence model was too restrictive and direct resolution (DNS) is preferable. For 10,0 0 0 < Re_b < 60,0 0 0, the combination of the different criteria led to a minimum resolution of 1140 ×37 ×74 cells for coarse LES, and 1925 ×62 ×125 cells for well-resolved LES, regardless of the Reynolds number. Finally, recommendations were maded on how to achieve a well-resolved LES based on examination of the vertical profiles of the ratio of SGS viscosity to molecular viscosity, and of the SGS (called subgrid-scale modeling and it is used to represent the effects of unresolved small-scale fluid motions (small eddies, swirls, vortices) in the equations governing the large-scale motions that are resolved in computer models). They showed that $N_v = \nu_{SGS} / \nu$ (The ratio of the SGS viscosity to the molecular viscosity), and $N_S = \tau_{SGS,12} / (u' v')_{ave}$ (the ratio of the SGS shear-stress to the resolved Reynolds stresses) decrease with grid refinement inside the current head. However, threshold values for a well-resolved LES are difficult to define. From the two-point correlations and the power spectrum densities they concluded that a complete resolution of the flow in the low turbulence region above the upper boundary of the current is achieved when N_v< 0.3. The ratios of shear-stresses inside the turbulent mixing layer was recommended to converge to values below $N S$ < 0.05 to achieve a well-resolved LES (Pelmard & al.2018).

In (2016) Penney& Stastna presented three-dimensional direct numerical simulations of laboratory scale double-diffusive gravity currents. The study utilized high-resolution DNS to simulate currents and presented an analysis of the effects of boundary conditions and current volume on flow development. Flow was governed by the incompressible Navier-Stokes equations under the Boussinesq approximation (which is called Joseph Valentin Boussinesq, it is used in the field of buoyancy-driven flow. Density diffrence is not taken into account except where they appear in terms multiplied by g, the acceleration due to gravity. The basis of the Boussinesq approximation is that the difference in inertia is negligible but gravity is sufficiently strong to make the specific weight appreciably different between the two fluids), with salinity and temperature coupled to the equations of motion using a nonlinear approximation to the UNESCO equation of state. The effects of vertical boundary conditions and current volume were examined, with focus on flow pattern development, current propagation speed, three-dimensionalization, dissipation, and stirring and mixing. It was observed that no-slip boundaries cause the gravity current head to take the standard lobe-and-cleft shape(Structures which is formed in the front part of the intrusive gravity current) and encourage both a greater degree and an earlier onset of three-dimensionalization when compared to what occurs in the case of a free-slip boundary. Under the effects of the no-slip condition, the current head exhibits the classical lobe-and-cleft instability and a significant degree of three-dimensionalization, while under the effects of free-slip conditions, the head remains two-dimensional and takes the shape predicted by inviscid theory. Two-dimensional salt fingers develop in the primary direction of the shear near the bottom of the wake of the currents. These fingers eventually experience spanwise rippling due to the shear-induced salt sheet instability, leading to fully three-dimensional salt fingers. Additionally, numerical simulations with no-slip boundary conditions experienced greater viscous dissipation, stirring (A process that occurs during the propagating of a gravity current in an ambient fluid and allows for the homogenization of mixable liquids), and mixing when compared to similar configurations using free-slip conditions. Preliminary investigations were suggested that shear dominates the double-diffusive instabilities in this type of configuration, which led to a typical gravity current, and little in the way of double diffusive effects (Penney& Stastna 2016).

In (2022) Farenzena & Silvestrini proposed a new method of front position determination free of arbitrary iso-value choice and strategies to minimize local uncertainty errors in the temporal evolution of the front velocity. Obtained results show that the local uncertainty error in front velocity was a function of the spatial discretization, the temporal sampling and the numerical derivative method. Such error could be minimized by the use of interpolation in the front position

acquisition method and/or using a new definition for the front velocity proposed in this study. The mathematical model and the computational code employed were described to perform the numerical simulations, The method to measure the front position from data was introduced, they showed the front velocity definition and its local uncertainties. The results presentation was divided into three parts: initially, the general features of a lock-release gravity current were presented with instantaneous flow visualizations. Afterward, they showed the front position obtained using the previously presented approaches. Finally, they presented the front velocity evaluation and its uncertainty (Farenzena& Silvestrini 2002).

In (2019) Tao&Zhang have made a research contribution to analyzed the Rayleigh-Taylor instability (RTI). Rayleigh-Taylor instability (RTI) along the density interfaces of gravity current fronts has been analyzed. The equations were solved with a pseudos-pectral method (or discrete variable representation (DVR) methods, are a class of numerical methods used in applied mathematics and scientific computing for the solution of partial differential equations) to study the lock-exchange flows in a cuboid box. The flowfield was expanded in Fourier modes in the x and z directions and Chebyshev polynomials in the y direction. Both the location and the spanwise wave number of the most unstable mode determined by the local dispersion relation agree with those of the strongest perturbation obtained from numerical simulations, suggesting that the original formation mechanism of lobes and clefts at the current front is RTI. Furthermore, the predictions of the semi-infinite RTI model, i.e., the original dominating spanwise wave number of the Boussinesq current substantially depends on the Prandtl number (which is a dimensionless number, defined as the ratio of momentum diffusivity to thermal diffusivity) and has $a^{1/3}$ scaling law with the Grashof number(which is a dimensionless number and defined as the ratio of the buoyancy to viscous forces acting on a fluid), are confirmed by the three-dimensional numerical simulations. They illustrated that the density stratification was the crucial factor dominating the onset of lobes and clefts. Without any detailed information of the flow field but only the fluids' properties (Gr and Pr) They showed theoretically and numerically that the Prandtl number has a substantial effect on the wave-number selection. With the increase of Gr and the development of turbulent states (Tao& Zhang2019).

In (2009) GONZALEZ-JUEZ & MEIBURG obtained simulation results for the flow of a partial-depth lock-exchange gravity current past an isolated bottom mounted obstacle by means of two-dimensional direct numerical simulations and steady shallow-water theory. The simulations indicated that the flux of the current downstream of the obstacle is approximately constant in space and time. This information was employed to extend the shallow-water models of (Rottman et

al.1985) and (Lane-Serff&al.1995) in order to predict the height and front speed of the downstream current as functions of the upstream Froude number and the ratio of obstacle to current height. The model predictions were found to agree closely with the simulation results. In addition, the shallow-water model provided an estimate for the maximum drag that lies within 10% of the simulation results for obstacles much larger than the boundary-layer thickness (GONZALEZ-JUEZ& MEIBURG2009).

Using high resolution numerical simulations of the two-dimensional Navier–Stokes equations, François Blanchette &al. (2006) evaluated a conceptually simple approach to model gravity currents traveling over a bottom boundary of varying slope. Their objective was to develop a conceptually simple approach which allows to simulate complex geometries. They considered a rectangular
computational domain, which allows for simple and efficient implementation of the equations and boundary conditions. Rather than implementing a complete coordinate transformation, the varying slope was modeled through the introduction of a spatially varying gravity vector. They assumed that the density of the fluid is linearly related to the concentration, c of either a solute or suspended particles, $\rho=\rho_0(1+\alpha c)$where$\alpha=(\rho_p-\rho_0)/\rho_0$where$\rho_0$ and ρ_p are the fluid and particle density respectively, and ρ_0, ρ_p and c were dimensional quantities. Their methodology was validated through studies of mass and energy conservation. The propagation velocity of the current and qualitative features of the flow were also found to be consistent with experimental observations of gravity currents travelling down constant or varying slopes. The researchers found that such models can be used to simulate flows with high Reynolds numbers and thier computations were seen to be consistent with numerical results obtained by previous authors (Blanchette &al.2006).

In (2017) Francisco&al. presented a numerical investigation of bi-disperse particle-laden gravity currents in the lock-exchange configuration. The intention of this work was to present a significant improvement and extension of the preliminary previous studies. This discussion focused on explaining how the presence of more than one particle diameter influences the main features of the flow, such as deposit profile, the evolution of the front location and suspended mass. They developed the complete energy budget equation for bi-disperse flows. A set of two and three-dimensional direct numerical simulations (DNS), with different initial compositions of coarse and fine particles, are carried out for Reynolds number equal to 40 0 0. Such simulations showed that the energy terms were strongly affected by varying the initial particle fractions. The addition of a small amount of fine particles into a current predominantly composed of coarse particles increases it’s run-out distance. In particular, it was showed that higher amounts of coarse particles have a

dumping effect on the current development. Comparisons showed that the two-dimensional simulation does not reproduce the intense turbulence generated in 3D cases accurately, which results in a significant difference in the suspended mass, front position as well as the dissipation term due to the advective motion (Francisco & al.2017).

In (2019) Issakhov& al. preformed a numerical simulation of the movement of the water surface when a dam was broken by the volume of fluid (VOF) method. They developed a three-dimensional numerical model of a dam break flow and identified flooding zones for three test problems. The mathematical model was based on the Navier-Stokes equations and uses the LES turbulent model, describing the flow of an incompressible viscous fluid and the equation for the phase (to determine the phase properties across the interface). All calculations were performed using the ANSYS Fluent. As a turbulence model was used the Smagorinsky model (which is a model used for subgrid-scale for LES). These equations were discretized by the finite volume method. PISO algorithm was chosen for numerical solution of this system of equation. The movement of the water surface was captured by using the VOF method (The equation for the phase was numerically solved by the CICSAM-VOF method (wher CICSAM: Compressive Interface Capturing Scheme for Arbitrary Meshes). This CICSAM-VOF method was designed to capture the surface and was clearly solved and implemented to track the movement that occurs on the water surface in multidimensional models), which led to a strict mass conservation law. The accuracy of the 3D model and the chosen numerical algorithm were tested using several laboratory experiments on dam break problem. In each of the problems, the obtained results were compared with the experimental data and several calculations by other authors and in each of the test problems, the developed model showed results close to the experimental data. Comparison of simulation results with experimental data for various turbulent models was also performed. And also a three-dimensional model of dam break flow on uneven terrain was developed. Two combined problems were performed which are more close to real conditions, with the help of these problems, flooding zones and flooding time were identified that would help in evacuating people from dangerous zones. All the results they obtained were satisfactory and can be relied upon to continue scientific research in this field (Issakhov& al.2019).

In (2022) Garoosi & al. Improved the accuracy and consistency of Volume-of-Fluid (VOF) method for simulating multiphase flow problems with large density ratios and moving interfaces. To accomplish this a novel high-order TVD flux-limiter scheme (total variation diminishing (TVD) is a property of certain discretization schemes used to solve hyperbolic partial differential equations)

has been developed and applied to approximate the convective fluxes in the momentum, energy and volume fraction equations. Moreover, the classical implicit non-iterative PISO (Pressure-Implicit with Splitting of Operators) algorithm was modified according to SIMPLER algorithm (it is numerical procedure which is used to solve the Navier-Stokes equations. SIMPLE is an acronym for Semi-Implicit Method for Pressure Linked Equations) and the combined model(PISOR) was then employed to handle the pressure-velocity coupling and to maintain a high level of numerical accuracy. Furthermore, the piecewise linear interface calculation (PLIC) based on the Efficient Least Squares Volume-of-Fluid Interface Reconstruction Algorithm(ELVIRA)(which is a class of interface tracking algorithms) was adopted for the treatment of the interface and curvature estimation. The robustness and consistency of the proposed modifications in handling violent free-surface flows involving interface rupture and coalescence were verified via simulation of several canonical test cases including: dam break over the dry and wet beds, rotating square patch of fluid and Rayleigh-Taylor Instability (RTI). The researchers came to the following conclusions: (1) the proposed model outperformed the existent classical VOF model available in the OpenFoam® environment. (2) The proposed hybrid PISOR algorithm with the aid of monotone convection scheme can accurately resolve physical discontinuities without obvious numerical fluctuations. (3) The ELVIRA technique (Efficient Least-square Volume-of-fluid Interface Reconstruction Algorith) can successfully reconstruct any arbitrary linear interfaces. (4) the newly constructed third-order bounded scheme can effectively eliminate the interface smearing due to numerical dispersion and dissipation errors and subsequently retain the integrity of the interface shape. (5) the pressure under-relaxation factor in the present hybrid PISOR scheme can be taken as unity which in turn accelerates the convergence rate of numerical simulations. (6) the proposed PISOR algorithm is capable of solving wide range of complex velocity coupling problems without introducing convergence difficulties. (7) The proposed TVD scheme can robustly control thickness of the interface and preserve sharpness of moving interfaces over2,3mesh intervals. (8) An improved VOF-R model is capable of dealing with a wide variety of multiphase flows with high topological changes (Garoosi & al.2022).

In (2016) Kaloudis & al. and by using Direct Numerical Simulations (DNS) investigated the flow phenomena in the intrusion region of a thermal storage water tank during discharge. The work was focued to the study of GCs inconfined spaces, by considering their interactions with solid boundaries in storage tanks and their implications with regard to mixing. The early times of the discharging process have significant effect on the thermal mixing and the associated energy losses. Methods to assess mixing have been used (method of analyze the evolution of the thermocline

thickness), which is one of the most popular method to quantify the energy losses associated with mixing during the charge/discharge phases, (Haller et al.2009). A detailed time evolution of the flow and temperature fields inside the tank was obtained for a range of relevant Froude numbers (Fr). Parameters such as the thermocline thickness(δ), the entropy generation rate S_g and the thermal mixing factor(k) were calculated to quantify the mixing mechanism in the tank. There were several alternative discharging scenarios where the Froude number (Fr) varied between 0.05 and 2.00, a range which corresponds to typical discharging conditions in real applications involving water storage tanks. The gravity currents (GCs) developing as the incoming cold fluid flows along the floor of the tank, their subsequent reflection on the opposite vertical wall and the interaction between the reverse flow and the incoming flow were analyzed and correlated to δ, S_g and k. Results of thermal mixing factor were in a qualitative agreement with mixing models showing enhanced mixing for the starting times of the discharging process(Kaloudis & al.2016).

In (2010) Zhang & al., studied the head front location as the function of time for an axisymmetric gravity current. The RNG approach is a mathematical technique that can be used to derive a turbulence model similar to the k-epsilon, results in a modified form of the epsilon equation which attempts to account for the different scales of motion. In this study, the adopted renormalization group (RNG) k-ϵ model for Reynolds-stress closure was used to character the time-dependent current with transitional and highly localized turbulence. The following dimensionless parameters were used: $R^*_f=R_f/R_0$, $t^*=t/t_c$, where R_0 is the radius of cylindrical barrier, and $t_c=R_0(g'h0)^{-1/2}$ is the characteristic time, $g'=g\Delta\rho/\rho_a$ being the reduced gravitational acceleration, with g standing for the gravitational acceleration, and $\Delta\rho=\rho_0-\rho_a$ standing for density difference of salt water and fresh water. Seven cases were discussed in this study. Numerical results were well-supported by experimental observations and showed that the motion of gravity current passed through two phases: a slumping phase with constant front velocity, and a self-similar phase with the front velocity decreasing as $t^{1/2}$(Zhang & al.2010).

In (2018) Ottolenghi&al. presented numerical simulations to assess the ability of the Lattice-Boltzmann Method(LBM)(which is a class of computational fluid dynamics(CFD) methods for fluid simulation. A fluid density in this method is simulated with streaming and collision (relaxation) processes, instead of solving the Navier-Stokes equations directly) in reproducing the fundamental features of lock-exchange gravity currents. Both two- and three-dimensional numerical simulations were performed at different Reynolds numbers ($1000 \leq Re \leq 30.000$). The standard notation DnQm for m discrete velocities in n spatial dimensions is used throughout. They used two classes of

lattices, the D2Q9(for 9 discrete velocities in 2 spatial dimensions is used throughout) and the D3Q19(for 19 discrete velocities in 3 spatial dimensions is used throughout), both 4th order isotropic in two and three dimensions, respectively. Numerical results showed that for Re = 1000 there was the abrupt transition from the slumping to the viscous phase, without developing the inertial phase. Turbulence has been accounted for by implementing an equivalent Large Eddy Simulation (LES) model in the LBM framework. The advancement of the front position and the front velocity obtained by LBM numerical simulations are compared with laboratory experiments appositely performed with similar initial and boundary conditions and with previous results from literature, revealing that the dynamics of the gravity current as a whole is correctly reproduced. Lobes and clefts instabilities arising in three-dimensional simulations and the entrainment parameter are also analysed and comparisons with previous studies are presented. Numerical results showed the LBM can be considered as a valid tool for the investigation ongravity currents (Ottolenghi & al.2018).

In (2018) Issakhov& al.,investigated the effects of water on obstacles in the dam break flow problem numerically. The numerical simulation of this problem was carried out using the ANSYS Fluent software product. The numerical method was based on the Navier-Stokes equations describing the flow of an incompressible viscous fluid and the equation of state. As a numerical method for solving equations, the numerical algorithm PISO (Pressure-Implicit with Splitting of Operators)(which is is an efficient method to solve the Navier-Stokes equations in unsteady problems) was chosen. The water surface movement was captured by using the volume of fluid (VOF) method, which leads to a strict mass conservation. They were able to distinguish the models such as Realizable k-ε(which is the most common model used in computational fluid dynamics (CFD) to simulate mean flow characteristics for turbulent flow conditions. It is a two equation model that gives a general description of turbulence by means of two transport equations), SST k-ω (which is a two-equation eddy-viscosity model which has become very popular where (SST) is shear stress transport), DES models (which is called Detached Eddy Simulation, this approachis very popular in industrial applications as it helps overcoming some of the limitations of the RANS models) and for 3D problem especially the LES model, which very well describes flow behavior and pressure distribution on the dam surface. Moreover, the accuracy and reliability of the 2D and 3D models were tested using several small and large-scale laboratory experiments on dam destruction problem. The obtained free surface dynamics was compared with the experimental data and numerical results of other authors. These numerical results gave good agreement with the experimental data. Comparison of simulation results with experimental data for various turbulent models was also performed. By dam break flow problem simulation, the best turbulent models were

chosen, which describe almost the same pressure distribution. Finally, various forms of obstacles were examined, by which the pressure distributions were reduced three times on the dam (Issakhov& al.2018).

In (2018) Francisco & al. Investigated the idealized gravity currents over a flat bed for which density differences are small enough for the Boussinesq approximation(which is an approximation of the Navier-Stokes equations for incompressible free-surface flows in which there is a vertical density gradient resulting in the absence of hydrostatic equilibrium) to be valid. They presented three-dimensional highly resolved direct numerical simulations (DNS) of particle-laden gravity currents for the lock-exchange problem in an original basin configuration, similar to delta formation in lakes. The concentration of particles was described in an Eulerian fashion by using a transport equation combined with the incompressible Navier-Stokes equations, with the possibility of particles deposition but no erosion nor re-suspension. The focus of this study was on the influence of the Reynolds number and settling velocity on the development of the current which can freely evolve in the streamwise and spanwise direction. When the Reynolds number was increased, the currents exhibited a large number of curved lobe-and-cleft structures of different sizes, unevenly distributed radially, different from the straight ones observed in axisymmetric currents. Also it was showed that the settling velocity has a strong influence on the spatial extent of the current, the sedimentation rate, the suspended mass and the shape of the lobe-and-cleft structures while the Reynolds number mainly affecting the size and number of vortical structures at the front of the current, and the energy budget. One important result was that, unlike channelized gravity currents, the macroscopic dissipation E_d is not necessarily the dominant dissipation term when particles deposit at the bottom wall (Francisco&al.2018).

In (2015) Zgheib&al. They presented results from direct numerical simulations (DNS) of cylindrical particle-laden gravity currents. The DNS will allow to explore the three-dimensional struc-tures of the current from iso-surfaces of density and iso-surfaces of the swirling strength that show the intensity and structure of the coherent eddies. They considered the case of a full depth release with monodisperse particles at a dilute concentration where particle–particle interactions may be neglected. Eulerian-Eulerian model of the two-phase flow equations was implemented. They chosed a grid resolution of 680×680×109 (along the x, y, and z directions, respectively). The disperse phase was treated as a continuum and a two-fluid formulation is a dopted. They presented results from two simulations at Reynolds numbers of 3450 and 10.000. Thier results were in good agreement with previously reported experiments and theoretical models. At early times in the simulations, they observed a set of rolled up vortices that flow at varying speeds. These Kelvin-

Helmholtz (K-H) vortex tubes were generated at the surface and exhibit a counter-clockwise rotation. In addition to the K-Hvortices, another set of clockwise rotating vortex tubes initiate at the bottom surface and play a major role in the near wall dynamics. These vortex structures have a strong influence on wall shear-stress and deposition pattern. Their relations are explored as well. The results of the numerical simulation were compared wit previously reported results(Bonnecaze1995), and they matched very well(Zgheib&al.2015).

In(2018) Z.H.Gu & al., built a two-phase flow algorithm based on the interface-preserving level set method developed for three-dimensional dam-break flows on uniform staggered cartesian grids. This method solved mass transfer problems on a uniform staggered Cartesian grid (which is a simple way to avoid odd-even decoupling between the pressure and velocity. Odd-even decoupling is a discretization error that can occur on collocated grids and which leads to checkerboard patterns in the solutions). The advection equation that has been used to advect the level set function for capturing the interface was discretized by a proposed fourth-order spatial discretization scheme. This scheme was dispersion-relation-preserving and is compact-reconstruction weighted essentially non-oscillatory (DRP-CRWENO4). The scheme was compared with a previous fifth-order, weighted, essentially non-oscillatory (WENO5) scheme (which is the fifth-order WENO scheme for approximating the solution of hyperbolic conservation laws) and can represent an interface more accurately, while exactly preserving mass conservation. The level set approach introduced a mass correction term into the re-initialization equation based on local interface-preserving conditions. An explicit Adams-Bashforth algorithm (which is use to compute the approximate solution at an instant time from the solutions in previous instants, in each step of Adams–Moulton methods an algebraic matrix Riccati equation (AMRE) is obtained, which is solved by means of Newton's method) on a staggered Eulerian grid was used for the Navier–Stokes solver. The point successive over-relaxation method (SOR)(which is a variant of the Gauss–Seidel method for solving a linear system of equations, resulting in faster convergence) was then employed to solve the resulting linear system. Two one-dimensional wave propagation problems were simulated to verify the proposed DRP-CRWENO4 scheme (which is dispersion-relation-preserving and is compact-reconstruction weighted essentially non-oscillatory), which was shown to be capable of effectively capturing large gradients with fourth-order accuracy. To demonstrate their resolution, the two advection schemes (WENO5 and DRP-CRWENO4) were applied in two two-dimensional benchmark cases, i.e.,a vortex deforming problem and Zalesak’s disk problem(which is a test, a slotted circle of fluid rotates around the center of the domain in a solenoidal velocity field.it is used to assessment of the efficiency of an algorithms), where simulation results of both schemes were compared against each other. Demonstration study was then further extended to three-dimensional cases of the vortex

deforming problem and Zalesak's sphere problem, and simulation results agree well with those using hybrid particle level set method. Finally, several dam-break problems with and without obstacles were investigated to validate the coupled two-phase incompressible flow and level set method solver. The results for the predicted flow structure and mass conservation properties were compared with the reported experimental data or numerical simulations (Z.H.Gu & al 2018).

In (2020) Yiqun Ye & al.employed a mesh-free method to simulate dam-break wave spreading in different bed configurations. In the method, the pressure field is calculated by an equation to explicitly solve the pressure Poisson equation (PPE) (which is a classical elliptic partial differential equation which provides a relationship to extract the so-called pressure parameter from a distributed parameter on an enclosed domain). The mesh-free method was good at capturing the free surface in the dam-break flow. In the numerical method, an explicit calculation for the pressure field was used and the spatial operators are based on the Moving Particle Semi implicit method (MPS). The mesh-free method was validated to simulate the dam-break flow by comparing to available experimental measurements. The numerical method was also validated by modeling the dam-break wave propagating along the wet bed. The effect from the combination of dry and wet bed for the dam-break wave was also investigated by the mesh-free method. They noted that when the dam-break wave encounters the wet bed, the wave can push the downstream water body forwards while the wavefront speed is reduced. The downstream water depth can result in a more uniform bed shear stress compared to the flow with the dry bed and the large value of bed shear stress occurs in the vicinity of the wavefront. In the simulations, the flow characteristics including free surface, flow pattern, and wavefront movement, and bed shear stress are presented and discussed(Yiqun Ye & al.2020).

To understanding the gravity currents propagation at the base of a linearly stratified ambient. Dai & al.(2021) performed three-dimensional high-resolution simulations. A passive tracer was implemented in the simulations to quantitatively measure the energies associated with the gravity current and the ambient fluid. Attention was focused on the initial slumping stage of gravity currents. The dynamics of the subcritical gravity currents, and the supercritical gravity currents were qualitatively different and we examined with the help of three-dimensional and two-dimensional high-resolution simulations. For the subcritical gravity currents, the flow was dominated by the internal wave, the Kelvin–Helmholtz vortices (which are a regions in a fluid in which the flow revolves around an axis line, which may be straight or curved) were inhibited, and the two-dimensional simulation agrees well with and serves as a good surrogate model for the three-dimensional simulation in the slumping stage. For the supercritical gravity currents, the Kelvin-

Helmholtz vortices were pronounced and prone to breakup into three-dimensional structures in the slumping stage. By using two-dimensional simulation. They observed the kinetic energy associated with the supercritical gravity currents, and the potential energy associated with the ambient fluid. The transition distance for the slumping stage and dissipation rate in the system have underpredicted while the kinetic energy associated with the ambient and the potential energy associated with the current have over predicted by the two-dimensiona simulation for the supercritical gravity currents. It was understood that the internal Froude number is a logarithmic function of the stratification parameter R (i.e. Fr = 0.226+log(R)). In this study, they confirmed that the logarithmic relationship is valid only in the range$1 < R = 3$ but may fail outside this range. They also showed that the shallow-water model can appropriately describe the internal Froude number throughout the whole range $1 < R \leq 10$ in this study (Dai & al. 2021).

In (2021) Marshall&al., presented numerical simulations of the effect of high Schmidt number on three-dimensional flow. Schmidt number (Sc) is the ratio of the kinematic viscosity to the molecular diffusion coefficient. (DNS) method was used to investigate the structure and dynamics of gravity current flows by providing the instantaneous density and velocity fields. Three-dimensional direct numerical simulations of constant-influx solute-based gravity currents were presented. The spectral element solver Nek5000(which is a computational fluid dynamics code that simulates unsteady incompressible fluid flow with thermal and passive scalar transport) has been used with Reynolds numbers $100 \leq Re \leq 3000$ and Schmidt number1. The effect of Schmidt number in cases (Re, Sc) = (100,10), (100,100); and (500, 10) has been studied. These data were used to establish the effect of both Schmidt and Reynold number on different properties of gravity currents, such as density distribution and interface stability. The impact of varying the Schmidt number on both the head and body of gravity current flows have been investigated. It was shown that increasing Schmidt number from 1 leads to substantial structural changes not seen with increased Reynolds number in the range considered here. Some of the questions were answered, including: (1) how Reynolds and Schmidt numbers affect the structure of flow behind the head, in particular, the stability of the current-ambient interface, (2) How Reynolds and Schmidt numbers affect the structure of the head, in particular, the formation of lobe-and-cleft structures, (3) When assuming a low Schmidt number to reduce the computational cost of numerical investigations may be justified, and (4) Which of the changes observed with increased Schmidt number also occur with increased Reynolds number. Finally recommendations were made regarding lower Schmidt number assumptions, usually made to reduce computational cost (Marshall&al.2021).

In (2021) Dai&al. investigated gravity currents in the slumping phase from a full-depth lock-exchange configuration with a no-slip boundary by means of three-dimensional high-resolution simulations of the incompressible Navier–Stokes equations with the Boussinesq approximation. This work aimed at deepen the understanding of the vortices structure and the mechanism responsible for the merging of clefts and splitting of lobes for gravity currents propagating on the no-slip boundary. The simulations provided more detailed flow information to elucidate the merging and splitting processes. The three-dimensional domain was (L_{x1}×L_{x2}×L_{x3}) = (17×1.5×1). The front Reynolds number was in the range 383< Re_f < 3267. They symbolized the height of the gravity current head by $\tilde{d}$, mean lobe width $\tilde{b}$ and mean maximum lobe width $\tilde{b}_{max}$. These quantities were obedient to the empirical relationship:$\tilde{b}_{max}/\tilde{d} = 12.6{R_{ef}}^{-0.36}$ and $\tilde{b}/\tilde{d} = 7.4{R_{ef}}^{-0.39}$ respectively. The front Reynolds number was defined as: $R_{ef} = \widetilde{U}_f\tilde{d}/\tilde{V}$ here $\widetilde{U}$ was the front velocity and $\tilde{V}$was the fluid kinematic viscosity. With the viscous length scale, the mean lobe width and the mean maximum lobe width increase with increasing front Reynolds number. The merging process for the vortices structure inside a lobe required the interaction of three tooth-like vortices and the middle tooth-like vortex disintegrated and reconnected with the two neighbouring tooth-like vortices. Therefore, a cleft might continually merge with another neighboring cleft but might never disappear. The initiation of the splitting process could be attributed to the Brooke&Hanratty mechanism (Mechanism generating vortices near the wall) reinforced by the baroclinic production of vorticity. Depending on the orientation of the parent vortex, the resulting new cleft after the splitting process could shift laterally in the positive or negative spanwise direction along the leading edge of the gravity currents as the lobe-and-cleft structure. The researchers concluded that the results obtained were in agreement with the experimental results that had been reported earlier (Dai&al.2021).

In (2015) Ooi&al. reported the results of their numerical simulations from full three-dimensional direct numerical simulation of gravity currents propagating down a uniform slope. They presented three-dimensional direct numerical simulation by using Direct numerical simulation (DNS) method (which give complete three-dimensional and time-dependent solution of the Navier–Stokes equations to obtain results for the instantaneous fluid velocity as a function of position and time) of Boussinesq of gravity currents propagating down a uniform slope starting from a truncated cylinder initial shape. They modeled the release a finite amount of heavy fluid into an ambient environment of lighter fluid on a sloping boundary. They assumed the density difference was small. Simulations were carried out at Re=5000 and a grid resolution of (N_x,N_y,N_z)=(700,600,201) and slope angle T=5°, 10°, 15°, and 20°. The value of the Schmidt number was taken as unity for all simulations. In the experiments of (Ross&al.2002), the Schmidt number was much greater than1. However (Bonometti &al.2008) have shown that the Schmidt number only has a small effect on the

dynamics and structure of the gravity current, provided that the Reynolds number was high enough (O (10^4)). For smaller Reynolds number, diffusion effects would influence the mixing and front velocity of the gravity current. The time step was chosen such that the Courant number was always less than 0.5. Their data showed that in most cases, the gravity current evolved to a shape that was similar to a triangular wedge. The physical mechanisms leading to the formation of this triangular shape and the dynamics of such a structure was presented (Ooi&al.2015).

By using an implicit large eddy simulation (ILES) to model a gravity currents evolution, Patterson&al. (2005) presented a series of two-dimensional(2D), axisymmetric and three-dimensional(3D) numerical flow simulations. The aim was to examine at a qualitative level the suitability of an ILES to model a gravity current. In the 2D case the results were well predicted. The position and form of the gravity current. For the axisymmetric case, the form of the gravity current's head and the ring vortices above the head were accurately described by the simulations good agreement was observed between the experimental work and the simulations up to the point of vortex breakdown. Simulations based on modelling the axisymmetrical form of the Navier-Stokes equations cannot match the experimental observation after the breakdown of the ring vortex in the experiments because there is no mechanism for breakdown in the equations of motion. Examination of the 3D results shows that the lobe and cleft instability observed at the interface between the light and dense fluid were also modelled well. They concluded that the Large Eddy algorithm was successful in modeling a gravity current's large scale structure (Patterson&al.2005).

In (2016) Armenio&al. presented a contribution to the evaluation of entrainment and mixing in unsteady gravity currents, focusing on the effect of the aspect ratio between the initial water depth and the lock length (which is the horizontal distance between the barrier separating the two fluids and the adjacent edge of the tank), and the initial excess density driving the motion. Entrainment and mixing in lock-exchange gravity currents were investigated by large eddy simulations. Different methodologies were used in order to evaluate entrainment and mixing during the slumping phase. Laboratory experiments were also performed and the comparison between the numerical and experimental results showed an acceptable agreement. Nine different cases of lock-exchange gravity currents propagating over a horizontal surface were examined through both laboratory experiments and numerical simulations. These cases were obtained by varying the initial excess density driving the motion and the aspect ratio r of the initial water depth to the lock length. The aspect-ratio of the retained fluid was showed to affect the time development of the gravity current and the associated mixing. In the r = 0.5 and r =1 runs, mixing was evaluated using three different approaches. The first two methods are based on the evaluation of two entrainment parameters and

on the variation in time of the fractional area of the dense current; the third approach considers the evolution of the background potential energy. The entrainment is found to increase as r decreases. The occurrence of irreversible mixing is detected during the entire development of the flow, i.e. both in the slumping and self-similar phases. A higher amount of mixing was observed as r decreases and the initial excess density increases (Armenio&al.2016).

1.4.2 Issue and numerical project of this thesis

At the time that the study of interface instability between the gravity current and the air has received a lot of attention in the field of research, we find that the interface instability between the gravity current and ambient fluid due to the difference in density is still not well understood and has not received wide attention in the field of research. Hence this thesis came to shed light on the study of the interface instability between the gravity current and the horizontal bottom and the interface instability between the gravity current and the ambient fluid, as well as the effect of each of Reynolds and Weber numbers on the instability.

A numerical simulation was conducted to investigated the interface instability of gravity currents. The motion was treated using computational fluid dynamics (CFD), which is a branch of fluid mechanics that uses numerical methods and algorithms to solve and analyze problems involving fluids. By using Open FOAM software, the following numerical simulation were performed.

In this work we investigated the exchange wall of two immiscible fluids via the numerical simulation using a CFD package for the Reynolds numbers in the range25-7000. The flow has been driven by gravity current on a horizontal surface. The density of the gravity current was high and it is surrounded by a fluid of less density. Particular attention was given to observe two types of the interface instability. The results showed that, the first type was the interface instability between the heavy fluid and the horizontal bottom. The lower interface was seen in the form of balls containing the ambient fluid and surrounded by gravity current. We were showed that the instability between the heavy fluid and the horizontal bottom was happend when Reynolds numbers are less than or equal to 2000. The second type was the interface instability between the heavy fluid and the ambient fluid and this kind is called Holmboe instability. The numerical simulation results showed that the instability between the heavy fluid and the ambient fluid was happend when Reynolds numbers are greater or equal to 2500. OpenFOAM solver has been developed to release a specific

volume of gravity current into a static fluid of lower density. The front position points$\boldsymbol{X_f(m)}$, Weber numbers (We) and velocity front points $V_f(m/s)$for the gravity current were calculated. The velocity of front position points is equal to the hydrodynamic velocity inside the gravity current. Also, the velocity of front position points is equal to the nose velocity. Furthermore, the results were compared to non-dimensional variables and were identical.

This study was organized as follows:

(1) Description of geometrical domain: Three-dimensional geometry on horizontal plane was chosen as a test case. In this domain. The length of the case (0.8 m), the width (0.01m), the height (0.08m), The dimensions in which the gravity current is before launch were (0.08 m), (0.01 m) and (0.08 m) for its lenght, width and height respectively and the shape contains 12 vertices.

(2) Numrical Model: Equation for the interphase and Navier Stokes equations for two incompressible, isother mal immiscible fluids were used to describe two immiscible liquids.

(3) The Volume-of-Fluid (VOF) method: VOF method belongs to the Eulerian class of modeling approach. In order to surround to scientific understanding of numerical simulation, a description of this method has been presented.

(4) Results: The numerical simulation results for interface instabilities have been shown.

CHAPTER II
MODELLING

2 Chapter II Modelling

2.1 Introduction

For modelling, we consider the stability of the interface between two non-miscible liquids in the configuration presented in Figure 2.1. At initial time, a fixed volume of the denser liquid with density ρ_2 and viscosityμ_2 is released under the sole effect of gravity, over a plane smooth surface beneath a static ambient lighter one with density ρ_1 and viscosity μ_1. Such a configuration may represent the propagation of heavy oil escaping from the tank of an oil tanker that has sunk to the ocean floor. The interface is said to be stable if a small disturbance superimposed on it vanishes over time. The interface is said to be unstable if a small disturbance superimposed on it grows or remains constant over time.

Woumeni (1991) provides a comprehensive description of the effect of density gradient and viscosity gradient on interface stability. Indeed, considering a system of two liquids with different densities and viscosities, Woumeni (1991) points out four cases :

a/ Effect of density gradient

-If the lighter liquid is in the upper layer if a protusion with volume is superimposed to the system, i twill vanish because the Archimede force will be greater than its weigh.

-If the lighter liquid is in the lower layer, the weigh of the protusion overwhelms the Archimede force so, the protusion will grow and the flow is unstable.

b/ Effect of viscosity

-In the case where the moving liquid is the less viscous one, if a protusion is superimposed to the system, the isobars will be more spaced in the center than on the periphery. From Darcy's law, the local velocity being proportional to the pressure gradient, the velocity at the center will be lower than on the periphery, consequently the protusion will vanish.

-If the moving liquid is the more viscous one, the progression of the other liquid is impeded by the less mobile fluid in place. It follows a tightening of the isobars towards the center where the local velocity will become very important under Darcy's law. Therefore, any protusion will grow and the flow is unstable as shown.

More generally, an instability may occur in our flow configuration if a gradient exists between the respective velocities, densities, viscosities, temperatures or interfacial tensions of both fluid layers. In literature, different authors have modeled one or the other case. Thus, Yih (1961) among others studied the effect of viscosity and velocity stratification on horizontal interface stability. As well, Lagrée & Rossi (1997) among others present an analysis of the Kelvin-Helmholtz instability due to density and velocity stratification in presence of interfacial tension. For the first time, the general case where all gradients exist between a heavy lower layer and an upper lighter ambient liquid and the base plane is inclined is tackled in this work. Indeed, only the temperature and the

interfacial tenion gradients are not considered. Indeed, it is well known that when the temperature difference is not significant (this case), a thermo-mechanical coupling must not be brought out, while the intruding film at ocean bottom is assumed homogeneous so, the interfacial tenion between both layer is assumed constant and instabilities related to interfacial gradient such as Marangoni's effect are not considered.

In the second subsection, we present Yih's theory (1967) of viscosity-driven instability and in third subsection, we present the analysis of Guyon et al. (2001) among others, of Kelvin-Helmholtz instability. More recently, Kowal & al. (2019) considered but the internal stability of a horizontal monodirectional gravity current driven by the three gradients (Fig.2.1).

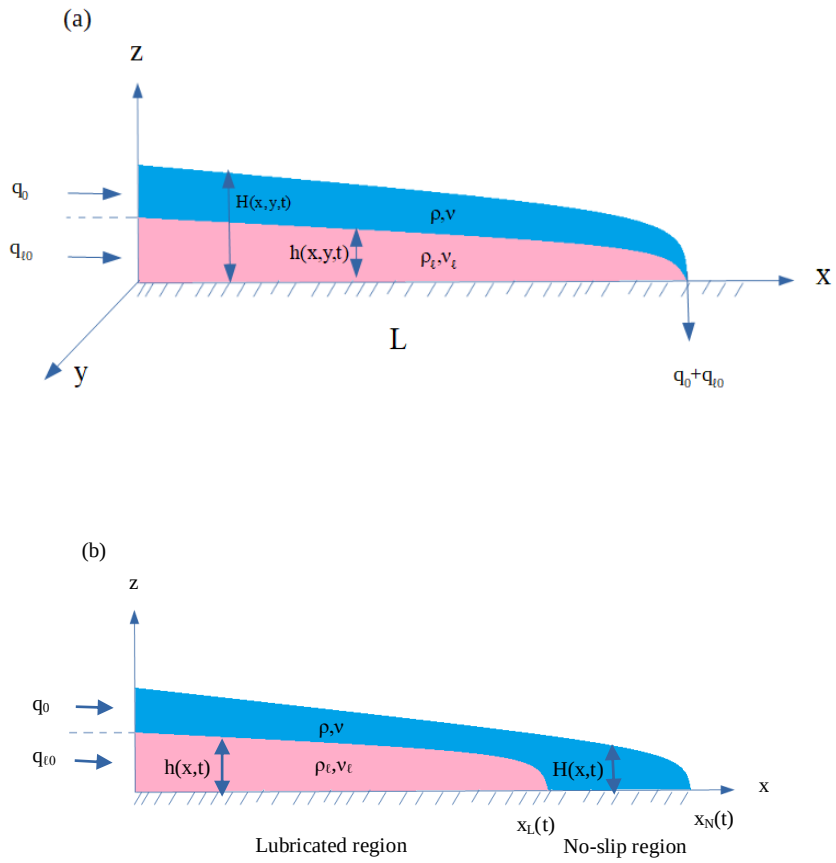

Figure 2.1: Monodirectional gravity current beneath an ambient liquid flow at (a) initial time $t = 0$ and at (b) assigned time $t = \tau$

In the fourth section, we propose an extension of the theoretical study of Kowal & al. to the case where the flow is bidirectional. Finally in the fifth subsection, we present the original model of the hydrodynamic stability of a denser gravity current over a sloping smooth plane beneath an ambient static lighter liquid in presence of velocity, viscosity and density gradients and interfacial tension as well.

2.2 Instability due to viscosity stratification (Yih, 1967)

We consider the stability of the horizontal interface between an upper liquid layer with viscosity μ_1 and a lower layer liquid with viscosity μ_2 flowing between two fixed and parallel solid plates. Both liquids have the same density ρ and the same thickness d. Figure 2.1 presents the flow configuration.

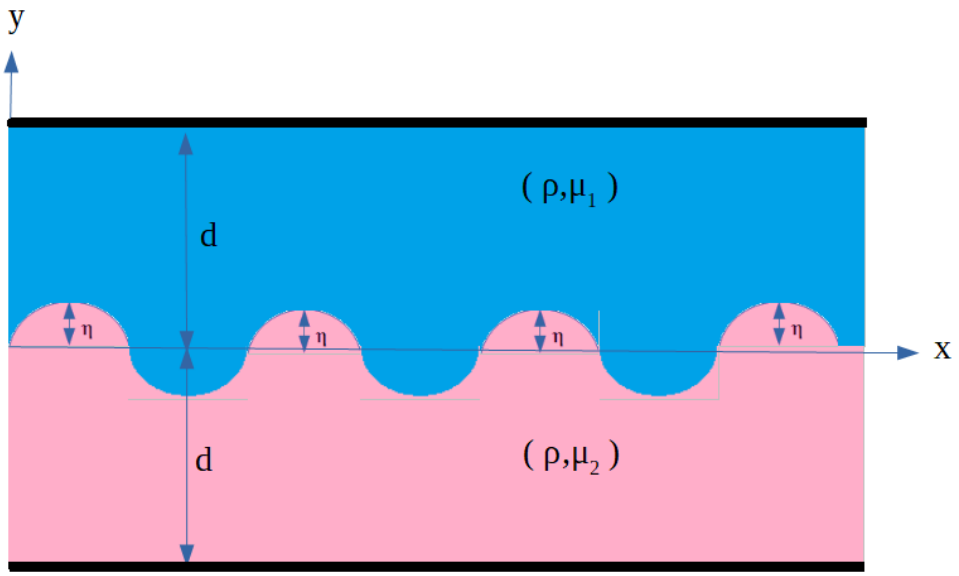

Figure 2.2: Instability occurring at the horizontal interface of two liquids of equal density and different viscosities in plane Poiseuille flow

2.2.1 Laminar steady basic flow

The laminar steady basic flow in $(X \quad -Y \quad)$ plane in each layer is governed in one hand by the equation of conservation of the mass

$$\mathrm{div}\left(\overrightarrow{V_{b\ (\iota)}}\right) = 0 \tag{2.1}$$

and in the other hand by the equations of conservation of the momentum

$$\rho \frac{\overrightarrow{dV_{b\ (\iota)}}}{\mathrm{dt}} = -\vec{\nabla} P_{b}^{\ (i)} + \mu_i \Delta \overrightarrow{V_{b\ (\iota)}} \tag{2.2}$$

where $i = 1$ refers to the upper layer and $i = 2$ to the lower layer. Operators $\mathrm{div}\left(\overrightarrow{V_{b}^{\ (\iota)}}\right)$, $\frac{\overrightarrow{dV_{b\ (\iota)}}}{\mathrm{dt}}$ and $\left(\vec{\Delta}\overrightarrow{V_{b\ (\iota)}}\right)$ on vector $\overrightarrow{V_{b\ (\iota)}} = U_{b}^{\ (i)}\overrightarrow{e_X} + V_{b}^{\ (i)}\overrightarrow{e_Y}$ are respectively defined as :

$$\mathrm{div}\overrightarrow{V_{b}^{\ (\iota)}} = \frac{\partial U_{b}^{\ (i)}}{\partial X} + \frac{\partial V_{b}^{\ (i)}}{\partial Y} \quad ; \quad \frac{\overrightarrow{dV_{b}^{\ (\iota)}}}{\mathrm{dt}} = \frac{\mathrm{dU}_{b}^{\ (i)}}{\mathrm{dt}}\overrightarrow{e_X} + \frac{\mathrm{dV}_{b}^{\ (i)}}{\mathrm{dt}}\overrightarrow{e_Y} - \rho\vec{g} \tag{2.3}$$

$$\frac{d}{\mathrm{dt}} \cdot \left[\frac{\partial}{\partial t} + U_b \frac{\partial}{\partial X} + V_b \frac{\partial}{\partial Y}\right] \cdot \quad ; \quad \vec{\Delta}\overrightarrow{V_b} = \Delta U_b \overrightarrow{e_X} + \Delta V_b \overrightarrow{e_Y} \; ; \; \Delta \cdot \left[\frac{\partial^2}{\partial X^{\ 2}} + \frac{\partial^2}{\partial Y^{\ 2}}\right] \cdot \tag{2.4}$$

where $\vec{g}$ denotes the gravity and the gradient of the pressure-field is defined as

$$\nabla P_b = \frac{\partial P_b}{\partial X}\overrightarrow{e_X} + \frac{\partial P_b}{\partial Y}\overrightarrow{e_Y} \quad (2.5)$$

Assuming a one-dimensional flow in X −direction, in each layer the previous continuity and Navier-Stokes equations, i.e. Eqs. (2.1)-(2.2) respectively reduce to

$$\frac{\partial U_b}{\partial X} = 0 \quad (2.6)$$

$$0 = \frac{-\partial P_b}{\partial X} + \mu \frac{d^2 U_b}{\mathrm{dY}^2} \quad (2.7)$$

$$0 = \frac{-\partial P_b}{\partial Y} - \rho g \quad (2.8)$$

With the help of the equation of continuity, Equ. (2.7) indicates that $\frac{-\partial P_b}{\partial X} = K$ where K is a true constant, then Equ.(2.7) can be written as

$$\frac{d^2 U_b}{\mathrm{dY}^2} = \frac{-K}{\mu} \quad (2.9)$$

Equ. (2.9) must be solved in each layer with the viscosity μ taking the value $\mu_1$in the upper layer and μ_2 in the lower layer with the boundary layers stating

-the no slip condition on both limiting plates

-the continuity of velocity and shear at the interface

Defining the non dimensional coordinates and velocities respectly as follows :

$$X = \frac{X}{d} \quad ; \quad Y = \frac{Y}{d} \quad ; \quad U_{b(1)} = \frac{U_{b(1)}}{U_b\ (0)} \quad ; \quad U_{b(2)} = \frac{U_{b(2)}}{U_b\ (0)} \quad (2.10)$$

The solution of Equ. (39) associated with the boundary conditions given by Equ.(3.10) write as follows in non dimensional form

$$U_i = 1 + a_i y + b_i y^2 \quad (2.11)$$

where subscript $i = 1$refers to the upper layer and $i = 2$ refers to the lower layer. Noting the viscosity ratio as

$$m = \frac{\mu_2}{\mu_1}$$

the constants $a_i$and $b_i$are given by

$$a_1 = \frac{1}{2}(m-1) \quad ; \quad b_1 = \frac{-1}{2}(m+1) \quad ; \quad a_2 = \frac{1}{2}\left(1 - \frac{1}{m}\right) \quad ; \quad b_2 = \frac{-1}{2}\left(1 + \frac{1}{m}\right) \quad (2.12)$$

2.2.2- Equation governing the flow stability

Let us superimpose on the latter laminar steady base flow a small disturbance with hydrodynamic field in the i^{th}layer $(\hat{u}_i, v_i, p_i)$ and that can be made non dimensional by the use of the following statements

$$u_i = \frac{u_i}{U_b(0)} \quad ; \quad v_i = \frac{v_i}{U_b(0)} \quad ; \quad p_i = \frac{p_i}{\rho\left(U_b(0)\right)^2} \quad ; \quad \tau = \frac{\mathrm{tU}_b(0)}{d} \quad (2.13)$$

Therefore, the resulting flow with hydrodynamic field

$$\left(U_i = U_{b(i)} + u_i, v_i, P_i = P_{b(i)} + p_i\right) \quad ; \quad u_i, v_i << U_{b(i)} \quad (2.14)$$

is governed both by the Navier Stokes equations and the continuity that respectively write

$$\frac{\mathrm{dU}_i}{\mathrm{dt}} = \frac{-\partial P_i}{\partial x} + \frac{1}{\mathrm{Re}}\Delta U_i \quad (2.15)$$

$$\frac{\mathrm{dv}_i}{\mathrm{dt}} = \frac{-\partial P_i}{\partial y} + \frac{1}{\mathrm{Re}}\Delta v_i \quad (2.16)$$

$$\frac{\partial U_i}{\partial x} + \frac{\partial v_i}{\partial y} = 0 \quad (2.17)$$

Where $\mathrm{Re} = \frac{\rho U(0) d}{\mu_1}$ stands for the Reynolds number. As the basic laminar steady flow obeys the continuity equation, we can see that Equ. (2.17) reduces to

$$\frac{\partial u_i}{\partial x}+\frac{\partial v_i}{\partial y}=0 \qquad (2.17b)$$

Which suggests us to introduce a stream function ψ_i in the i^{th} layer, defined as follows

$$u_i=\frac{\partial \psi_i}{\partial y} \quad ; \quad v_i=\frac{-\partial \psi_i}{\partial x} \qquad (2.18)$$

If a choice of an exponential time-dependence of the stream function and the pressure, i.e.

$$\{\psi_i(x,y,t),p_i'(x,y,t)\}=\{\varphi_i(y),f_i(y)\}\cdot\exp[i\alpha(x-c\tau)] \qquad (2.19)$$

Where c is complex and α is real

The flow is stable if a small disturbance vanishes with time, i.e. if c_i is is negative while

The flow is unstable if a small disturbance grows or remains constant with time, i.e. if c_i is positive or nul.

Then, we introduce the expressions assumed for the disturbance, say Equs. (2.14) ; (2.18) ; (2.19) into the equations of motion given by Equs.(2.15)-(2.17). Noting that the basic laminar static flow itself obeys these same equations, the equations governing the disturbance in the upper layer $(i=1)$ are derived in the following form after linearization

$$i\alpha\left[\left(U_{b(i)}-c\right)\varphi_1'-U_{b(i)}'\varphi_1\right]=-i\alpha f_1+\mathrm{Re}^{-1}\left(\varphi_1'''-\alpha^2\varphi'\right) \qquad (2.20)$$

$$\alpha^2\left(c-U_{b(1)}\right)\varphi_1=f_1'+\left(\frac{i\alpha}{\mathrm{Re}}\right)\left(\varphi_1''-\alpha^2\varphi_1\right) \qquad (2.21)$$

Where the primes appearing on $f, U_{b(1)}$ and φ indicate derivation with respect to variable y.

Introducing Equ. (2.20) into Equ.(2.21) leads to the following Orr-Sommerfeld type equation

$$\varphi_1^{(4)}-2\alpha^2\varphi_1''+\alpha^4\varphi_1=i\alpha\mathrm{Re}\left[\left(U_{b(1)}-c\right)\left(\varphi_1''-\alpha^2\varphi_1\right)-U_{b(1)}''\varphi_1\right] \qquad (2.22)$$

Equs. (2.20)-(2.22) refer to the upper layer layer $(i=1)$. For the lower layer $(i=2)$, the corresponding Orr-Sommerfeld type equation writes

$$\varphi_2^{(4)}-2\alpha^2\varphi_2''+\alpha^4\varphi_2=\frac{i\alpha\mathrm{Re}}{m}\left[\left(U_{b(2)}-c\right)\left(\varphi_2''-\alpha^2\varphi_2\right)-U_{b(2)}''\varphi_2\right] \qquad (2.23)$$

Equs. (2.22) and Equ.(2.23) govern the flow stability associated to the corresponding boundary conditions govern the flow stability in the upper and in the lower layer respectively.

2.2.2 Boundary conditions

The associated boundary conditions are the following :

a/No slip condition on the solid plates

$$\varphi_1(1)=0 \quad ; \quad \varphi_1'(1)=0 \qquad (2.24)$$

$$\varphi_2(-n)=0 \quad ; \quad \varphi_2'(-n)=0 \qquad (2.25)$$

b/Continuity of velocity, for v and u write respectively

$$\varphi_1(0)=\varphi_2(0)$$

$$\varphi_1'(0)-\varphi_2'(0)=\frac{\varphi_1(0)}{c'}U_{b(2)}'(0) \qquad (2.26)$$

Where

$$c'=c-U(0) \qquad (2.27)$$

c/Continuity of shear stress

$$\varphi_1''(0)+\alpha^2\varphi_1(0)=m\left[\varphi_2''(0)+\alpha^2\varphi_2(0)\right] \qquad (2.28)$$

d/Normal stress condition

$$m\left(\varphi_2'''-3\alpha^2\varphi_2'\right)-\left(\varphi_1'''-3\alpha^2\varphi_1'\right)=\frac{i\alpha^3\mathrm{Re}S\varphi_1}{c'} \quad \text{at} \quad y=0 \qquad (2.29)$$

Where

$$S=\frac{T}{\rho \mathrm{dV}^2} \qquad (2.30)$$

and T denotes the interfacial tension.

2.2.3 Solution

Assuming that αRe<<1, the previous set of differential equations can be solved by successive approximations (Yih, 1967). This is a non-singular perturbation method around the case $\alpha = 0$, which corresponds to long waves.

-In the first approximation, all the terms containing α are neglected in the differential system. Therefore, Equs (2.22) - (2.23) write

$$\varphi_{i(0)}^{(4)} = 0 \quad \text{with} \quad i = 1,2 \tag{2.31}$$

All the boundary conditions remain unchanged except for the continuity of the shear stress given by Equ. (2.28) and for the normal stress condition given by Equ. (2.29) which respectively reduce to

$$\varphi_{1(0)}^{''}(0) - m\varphi_{2(0)}(0) = 0 \tag{2.31}$$

$$\varphi_{1(0)}^{'''}(0) - m\varphi_{2(0)}^{'''}(0) = 0 \tag{2.32}$$

The solution for this differential system writes

$$\varphi_{1(0)} = 1 + B_1 y + C_1 y^2 + D_1 y^3 \tag{2.33}$$

$$\varphi_{2(0)} = 1 + B_2 y + C_2 y^2 + D_2 y^3 \tag{2.34}$$

Where

$$B_1 = \frac{7+m}{4} \; ; \qquad B_2 = \frac{1+7m}{4m} ; \qquad C_1 = \frac{1+m}{2} \tag{2.35}$$

$$C_2 = \frac{C_1}{m} \qquad ; \qquad D_1 = \frac{1-m}{4} \; ; \qquad D_2 = \frac{D_1}{m} \tag{2.36}$$

while the eigenvalue writes

$$c_0 = 1 + \frac{2(m-1)^2}{(m^2+14m+1)} \tag{2.37}$$

-In the second approximation, all the terms containing α^2 or of higher order than 2 are neglected, the differential system then reduce to

$$\varphi_{1(1)}^{(4)} = i\alpha\mathrm{Re}\left[(U_0 - c_0)\varphi_{1(0)}^{''} - U_{b(1)}^{''}\varphi_{1(0)}^{''}\right] \tag{2.38}$$

$$\varphi_{2(1)}^{(4)} = i\alpha\mathrm{Re}\cdot m^{-1}\left[(U_0 - c_0)\varphi_{2(0)}^{''} - U_{b(2)}^{''}\ddot{o}_{2(0)}^{''}\right] \tag{2.39}$$

Whose solution writes

$$\varphi_{1(1)} = \Delta B_1 y + \Delta C_1 y^2 + \Delta D_1 y^3 + i\alpha\mathrm{Re}h_1(y) \tag{2.40}$$

$$\varphi_{2(1)} = \Delta B_2 y + \Delta C_2 y^2 + \Delta D_2 y^3 + i\alpha\mathrm{Re}\cdot m^{-1}h_2(y) \tag{2.41}$$

Where

$$h_1(y) = \frac{m^2-1}{1680}y^7 - \frac{(m-1)^2}{480}y^6 + \frac{m^4+18m^3-156m^2-98m-21}{480(m^2+14m+1)}y^5 - \frac{m^3-17m^2-17m+1}{24(m^2+14m+1)}y^4$$

$$h_2(y) = \frac{m^2-1}{1680}y^7 - \frac{(m-1)^2}{480}y^6 + \frac{21m^4+98m^3+156m^2-18m-1}{480m^2(m^2+14m+1)}y^5 - \frac{m^3-17m^2-17m+1}{24m(m^2+14m+1)}y^4$$

The constants $\Delta B_1, \Delta B_2, \Delta C_1, \Delta C_2, \Delta D_1, \Delta D_2$ are determined using the boundary conditions. The boundary conditions lead to

$$c = c_0 + \Delta c \qquad ; \qquad \Delta c = \mathrm{i}c_i \qquad ; \qquad c_i = 8\alpha\mathrm{Re}H_3 \tag{2.44}$$

$$H_3 = \left(\frac{1-m}{m^2+14m+1}\right)^2\left[\frac{-(m+1)}{2}\{h_1(1) + h_2(-1) + h_2'(-1) - h_1'(1)\} - A\right] \tag{2.45}$$

$$A = \frac{-(m-1)}{4}[h_1(1) - h_1'(1) - h_2(-1) - h_2'(-1)] - \mathrm{m}h_1(1) - h_2(-1) \tag{2.46}$$

The variation of H_3 vs**.** m is presented below in Fig. (2.3) using Equ. (2.45). The graph obtained shows that H_3 is always positive, whatever the value of m**.** It means that the plane Poiseuille flow of 2 liquids of equal density with a horizontal interface is always unstable, for any value of the Reynolds number.

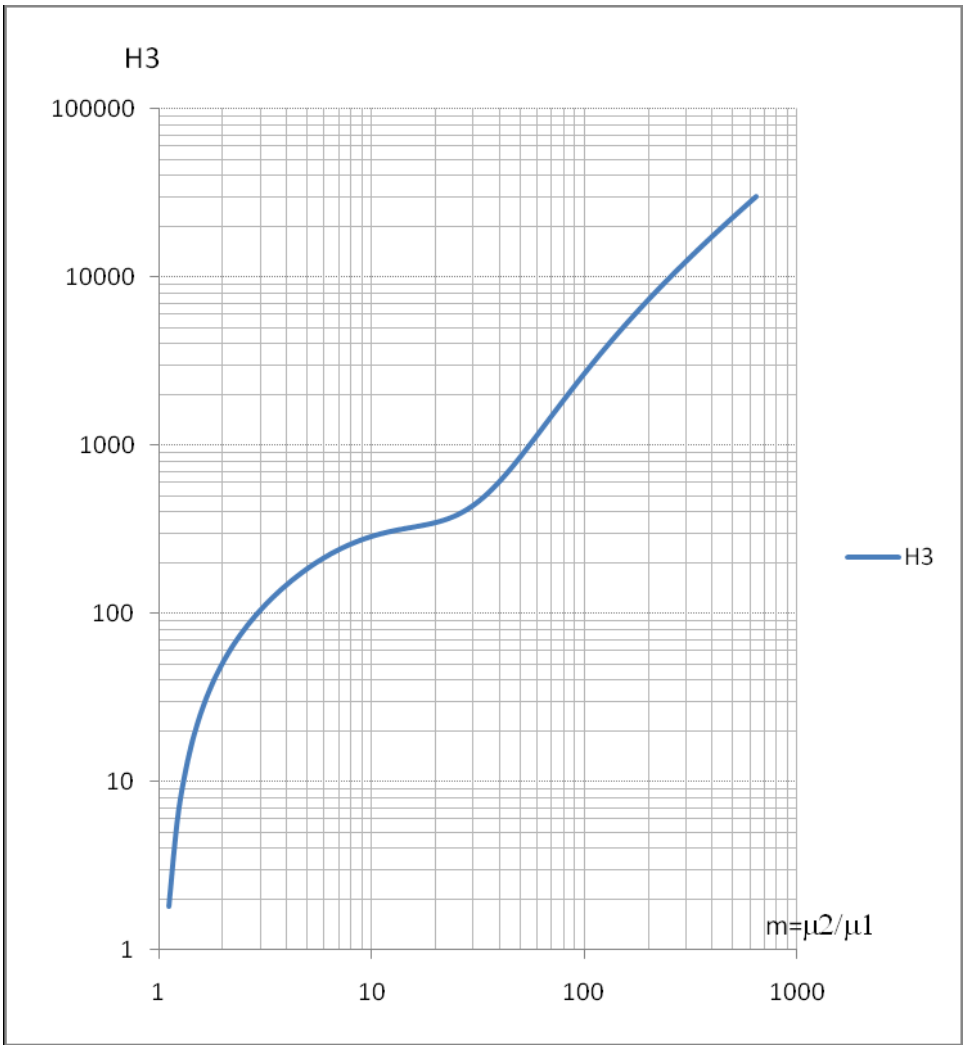

Figure 2.3 : Variation of H_3 vs. m (Yih, 1967)

2.3 The Kelvin-Helmholtz instability

2.3.1 Problem statement

Consider a system of two inviscid and non miscible fluids with different densities. The system is submitted to a plane shear flow under gravity action as shown in Figure 2.4 and the interface is assumed horizontal with a constant surface tension. Note that as the interface is assumed horizontal, the surface tension does not intervene explicitly because it is associated with a curvature of the interface. The density of the upper fluid is ρ_1 and its velocity U is constant while the lower fluid is gifted with a density ρ_2 and a velocity $-U$. Finally, we assume that both velocities derive from a potential, i.e.

$$U = \text{grad}(U \cdot x) \quad ; \quad -U = \text{grad}(-U \cdot x) \tag{2.47}$$

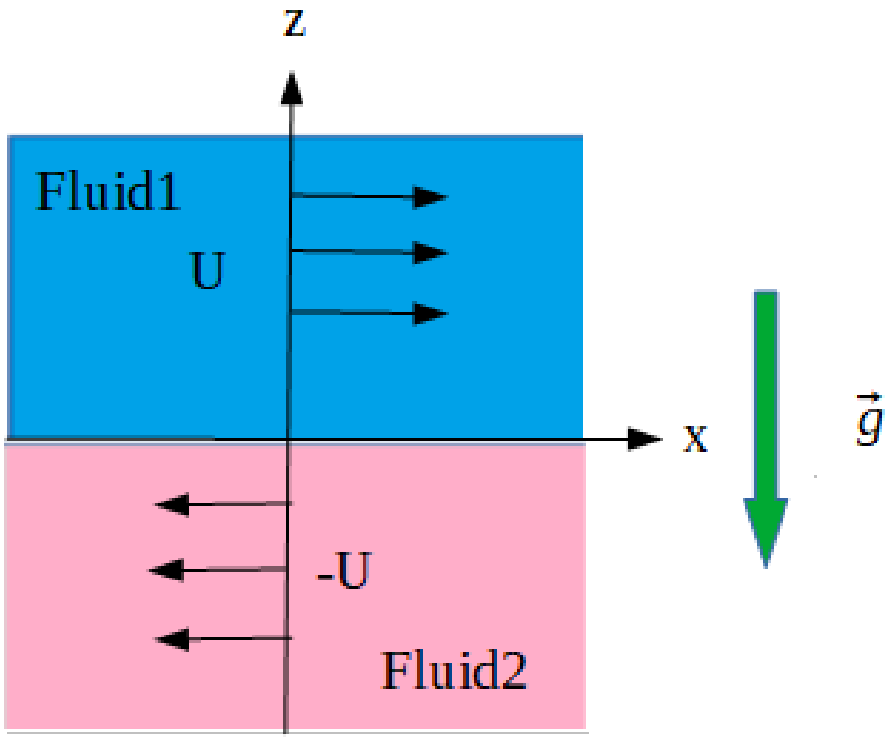

Figure 2.4 : The basic laminar steady flow

Notice that if the velocity distribution is more generally given by $U_{b(1)}$ in the upper layer and $U_{b(2)}$ in the lower layer as shown in Figure 2.5, the latter configuration used for the present model can be recovered by putting

$$U = \frac{U_{b(2)} - U_{b(1)}}{2} \tag{2.48}$$

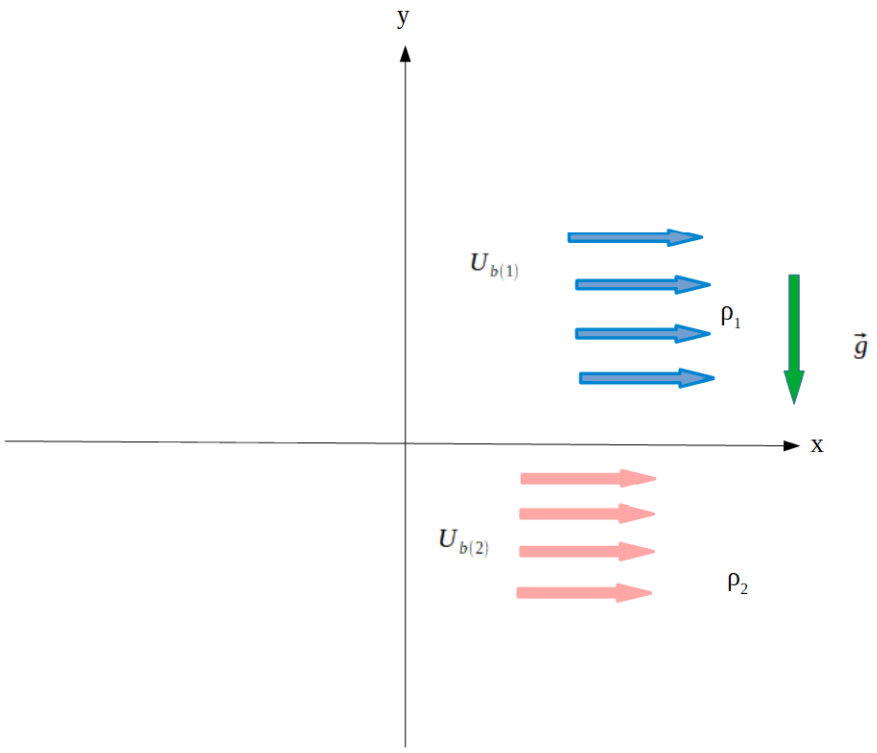

Figure 2.5 : Sketch of more general basic configuration

A linear study of the stability of that flow is now proposed.

2.3.2 Stability analysis

a/Equations

A small disturbance is superimposed to the interface. Therefore, the interface is no more horizontal but has the height $\xi(x,t)$.

As well, a small angle $\alpha(x,t)$ is defined between the horizontal axis and the tangent to the interface at abscissa x and time t, as shown in Figure 2.6.

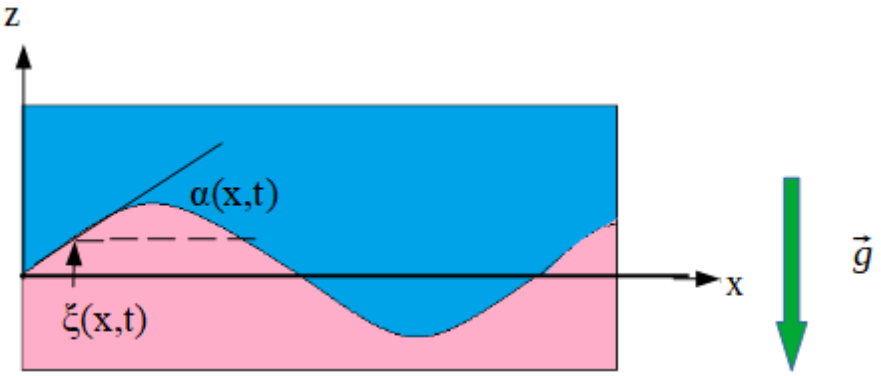

Figure 2.6 : Sketch of the small disturbance superimposed to the basic steady laminar flow

The resulting velocity field in lower and in upper layer is respectively given by :

$\vec{V}_1(x,z,t) = -\vec{U} + \vec{v}_1(x,z,t)$ with $v_1 = \text{gra}\setminus\{\vec{d}(\varphi_1)$ (2.49)

$\vec{V}_2(x,z,t) = \vec{U} + \vec{v}_2(x,z,t)$ with $v_2 = \text{gra}\setminus\{\vec{d}(\varphi_2)$ (2.50)

Now, let us adopt the following assumptions :

*$\xi(x,t)$ together with its space and time derivatives are infinitely small quantities to 1st order

*$|\vec{v}_1| << U$ and $|\vec{v}_2| << U$ (2.51)

*$\alpha << 1$ (2.52)

*$\left|\frac{\xi}{L}\right| << 1$ (2.53)

Where L is a characteristic length of the flow, the wavelength in this case.

So, the following consequences can be derived

*$\sin(\alpha) \approx \tan(\alpha) \approx \alpha \approx \frac{\partial \xi}{\partial x}$ (2.54)

*To 1st order, the normal to the interface can be written as :

$\vec{n}_{\text{interface}} = \cos(\alpha)\vec{e}_z - \sin(\alpha)e_x \approx \vec{e}_z - \alpha\vec{e}_x$ (2.55)

As both fluids are non miscible and inviscid, the normal components of the velocity fields of both fluids must be equal at the interface, i.e.

$\left[\vec{V}_1(x,\xi,t) - \vec{V}_2(x,\xi,t)\right] \cdot \vec{n}_{\text{interface}} = 0$ (2.56)

The normal velocities being defined as the interface velocity, i.e. the time derivatives of $\xi(x,t)$ we get

$v_{\text{jz}} - \alpha v_{\text{jx}} - \alpha U = \frac{\partial \xi}{\partial t}$ with $j \in \{1,2\}$ (2.57)

Taking into account the definitions of the different terms appearing in Equ. (3.57), it can be rewritten as

$\frac{\partial \varphi_j}{\partial z}(x,\xi,t) - \frac{\partial \xi}{\partial x}(x,t)\frac{\partial \varphi_j}{\partial x}(x,\xi,t) - \frac{\partial \xi}{\partial x}(x,t) \cdot U = \frac{\partial \xi}{\partial t}(x,t)$ (2.58)

In Equ. (2.58), the 2nd term in the left hand side being the product of two terms of the 1st order, it is of the 2nd order while the other terms of the equation are of the 1st order. Therefore, it can be neglected. So, Equ. (2.58) is simplified in the form

$\frac{\partial \varphi_j}{\partial z}(x,\xi,t) - U \cdot \frac{\partial \xi}{\partial x}(x,t) = \frac{\partial \xi}{\partial t}(x,t)$ (2.59)

The system of 2 partial differential equations (3.59) with 3 unknowns $\varphi_1(x,\xi,t), \varphi_2(x,\xi,t), \xi(x,t)$ must be completed by a complementary 3rd equation in order to form a well posed mathematical problem.

For this, we recall the following assumptions :

-the fluids are inviscid

-the velocities derive from a potential

-the flow is incompressible

-the only volumic force is weight which itself also derives from a potential.

Consequently, Bernoulli's theorem can be applied to the upper layer and to the lower layer separately, say :

$$\begin{cases} P_1 + \rho_1\left(\frac{\partial \varphi_1}{\partial t}_{z=\xi} + g\xi + \frac{V_1^2}{2}\right) = C_1 \\ P_2 + \rho_2\left(\frac{\partial \varphi_2}{\partial t}_{z=\xi} + g\xi + \frac{V_2^2}{2}\right) = C_2 \end{cases} \quad (2.60)$$

Equating at the interface ($z = \xi$), the pressure in each field derived from Equ. (3.60), we get

$\rho_1\left(\frac{\partial \varphi_1}{\partial t}_{z=\xi} + g\xi + \frac{V_1^2}{2}\right) - \rho_2\left(\frac{\partial \varphi_2}{\partial t}_{z=\xi} + g\xi + \frac{V_2^2}{2}\right) = C_1 - C_2$ (2.61)

Recalling that V_1 and V_2 are the resulting velocity fields in the upper and in the lower layer respectively, i.e.

$V_1 = U + v_1$; $V_2 = -U + v_2$ (2.62)

there comes

$$V_1^2 = U^2 + 2U \cdot \vec{v}_1 + v_1^2 \quad ; \quad V_2^2 = U^2 - 2U \cdot \vec{v}_1 + v_2^2 \tag{2.63}$$

Moreover, the disturbance being assumed small, the following approximations can be made from Equ. (2.63)

$$V_1^2 = U^2 + 2U\frac{\partial \varphi_1}{\partial x} \quad ; \quad V_2^2 = U^2 - 2U\frac{\partial \varphi_2}{\partial x} \tag{2.64}$$

Substituting these expressions of V_1^2 and V_2^2 in Equ. (2.62), we obtain

$$\rho_1\left(\frac{\partial \varphi_1}{\partial t}_{\quad z=\xi} + \frac{U^2}{2} + U\frac{\partial \varphi_1}{\partial x}\right) - \rho_2\left(\frac{\partial \varphi_2}{\partial t}_{\quad z=\xi} + \frac{U^2}{2} - U\frac{\partial \varphi_2}{\partial x}\right) + g(\rho_1 - \rho_2)\xi = C_1 - C_2$$

Finally, we recall that C_1 and C_2 in Bernoulli's equation are arbitrary constants so, we must choose a gauge for the potentials in order to identify the streamlines in the flow field. The gauge is chosen such that

$$\rho_1\left(\frac{\partial \varphi_1}{\partial t}_{\quad z=\xi} + g\xi\right) = \rho_2\left(\frac{\partial \varphi_2}{\partial t}_{\quad z=\xi} + g\xi\right) \tag{2.66}$$

So, we find

$$C_1 - C_2 = \rho_1\left(\frac{U^2}{2} + U\frac{\partial \varphi_1}{\partial x}\right) - \rho_2\left(\frac{U^2}{2} - U\frac{\partial \varphi_2}{\partial x}\right) \approx (\rho_1 - \rho_2)\frac{U^2}{2} \tag{2.67}$$

Consequently, Equ. (2.65) takes the following simplified form

$$\rho_1\left(\frac{\partial \varphi_1}{\partial t}_{\quad z=\xi} + U\frac{\partial \varphi_1}{\partial x}\right) - \rho_2\left(\frac{\partial \varphi_2}{\partial t}_{\quad z=\xi} - U\frac{\partial \varphi_2}{\partial x}\right) + g(\rho_1 - \rho_2)\xi = 0 \tag{2.68}$$

b/Assumptions

Assume a time and space exponential form for $\varphi_1(x,\xi,t), \varphi_2(x,\xi,t), \xi(x,t)$ as follows

$$\begin{cases}\varphi_1(x,z,t) = B_1 e^{\mathrm{ikx}+\sigma t-\mathrm{kz}}\\ \varphi_2(x,z,t) = B_2 e^{\mathrm{ikx}+\sigma t+\mathrm{kz}}\end{cases} \tag{2.69}$$

Substituting these expressions for the corresponding functions $\varphi_1(x,\xi,t), \varphi_2(x,\xi,t), \xi(x,t)$ in Equ. (2.59), we get

$$\{-\mathrm{kB}_1 e^{-k\xi} - \mathrm{AUik} = A\sigma \tag{2.70}$$

Moreover, the disturbance being assumed very small, we have

$$e^{-k\xi} \approx 1 \tag{2.71}$$

So, Equs. (2.70) take the following simplified form

$$\{\mathrm{kB}_1 + (\sigma + \mathrm{ikU})A = 0 \tag{2.72}$$

while the 3rd complementary equation (2.68) becomes

$$\rho_1(\sigma + \mathrm{ikU})B_1 - \rho_2(\sigma - \mathrm{ikU})B_2 + g(\rho_1 - \rho_2)A = 0 \tag{2.73}$$

Finally, the flow stability is governed by Equs. (2.72) -(2.73) which is a set of 3 algebraic equations.

c/Solution

Substituting B_1 and B_2 in Equ. (3.73), for their expressions derived from Equ. (2.72) we get the following secular equation

$$\rho_1\frac{(\sigma+\mathrm{ikU})^2}{k} + \rho_2\frac{(\sigma-\mathrm{ikU})}{k} + g(\rho_1 - \rho_2) = 0 \tag{2.74}$$

Where a new unknown can be sorted in the form

$$X = \frac{\sigma}{k} \tag{2.75}$$

And the secular equation then writes

$$X^2 + 2\mathrm{iU}\frac{\rho_1-\rho_2}{\rho_1+\rho_2}X - U^2 + \frac{g}{k}\frac{\rho_1-\rho_2}{\rho_1+\rho_2} = 0 \tag{2.76}$$

Equ. (2.76) is a 2nd order algebraic equation whose solutions write

$$X = \frac{\sigma}{k} = i\frac{(\rho_2-\rho_1)U}{\rho_1+\rho_2} \pm \sqrt{\frac{4\rho_1\rho_2U^2}{(\rho_1+\rho_2)^2} - \frac{g}{k}\frac{\rho_1-\rho_2}{\rho_1+\rho_2}} \tag{2.77}$$

The Kelvin-Helmholtz instabilities appear if the waves exist, i.e. if their amplitude follows an exponential variation with time. So, the 2nd term of Xin Equ. (2.77) must be real. Therefore, the condition for the instabilities to appear writes

$$\frac{4\rho_1\rho_2U^2}{(\rho_1+\rho_2)^2} > \frac{g}{k}\frac{\rho_1-\rho_2}{\rho_1+\rho_2} \quad (2.78)$$

The only condition for the appearance of instabilities is that the condition posed by Equ. (2.78) is satisfied. Only 3 parameters are driving the phenomenon : the fluids velocity $U$and the densities of the different layers : $\rho_1$and ρ_2.

Finally, we notice that the greater the difference in the speeds of the 2 fluid layers, the more Kelvin-Helmholtz instabilities are likely to appear.

2.4 Extension of Kowal's model to the stability analysis of lubricated viscous bidirectional gravity current

Kowal et al. (2019) addressed the question to determine whether the resulting instability was an internal instability resulting from the internal movement of fluid particles, or a frontal instability resulting from the movement of the head and intrusions into the surrounding fluid, as shown in figure 2.1. This subsection is to extend Kowal's model to the bidirectional case. In this aim, we analyze the stability of a lubricated viscous bidirectional gravity current. A local stability analysis in an inner region near the lubrication front in two directions is performed. The linear stability analysis of the steady basic flow is brought out and the perturbation fluxes and normal-mode solutions are derived. Exploring the asymptotic behavior of the perturbations in an inner region of size ε (the small parameter) and expanding the solution as a series ε, three flow control parameters are pointed out, say the relative density difference, the viscosity ratio and the flux ratio. Moreover, we show that the system is stable to all perturbations, whatever the choice of these three dimensionless parameters. In order to generalize this unexpected result, it was checked numerically in the case of two miscible liquids. The numerical simulations of a viscous miscible gravity current show that the flow is stable.

2.4.1 Introduction

Oil spills are health, ecological and economic disasters (Tansel, 2014, French-McCay, 2004). They can be caused by the accidental (ruin of the material constituting the tank) or intentional (degassing or act of war) spillage of a large quantity of oil from an oil tanker into the ocean. An oil spill then undergoes the distribution of oil on the water surface, on shorelines, in the water column and in the sediments accounting for spreading, evaporation, transport, dispersion, emulsification, entrainment, dissolution, volatilization, partitioning, sedimentation and degradation. The collection, destruction, and storage of the oil that ran aground on the coast, as well as the coast cleaning are arduous, dangerous and penalizing tasks. Moreover, oil spills are health, ecological and economic disasters for the populations living in these soiled territories (Reed et al., 1999).

All models seek to describe the key physical and chemical processes that transport and weather the oil on and in the sea. Two models purporting to contain the same algorithms may give quite different results from the same input data and namely give quite different ratios between spreading, evaporation, emulsification and natural dispersion. This is the proof that oil spill is a complex

phenomenon of which each process (advection, spreading, evaporation, dispersion, emulsification) must firstly be controlled before they are put into competition by a relevant modeling.

In this paper, we study the 2D propagation of a dense fluid (with density ρ and kinematic viscosity ν) plunging from a reservoir to the bottom of a large body of ambient liquid, static water in this case (with density ρ_0 and kinematic viscosity ν_0). Based on this description, the phenomenon studied is defined as a lubricated (a flow in which one dimension is significantly smaller than the others) gravity current (a flow of one fluid driven by the gravity into another fluid with a different density). The ocean is not flat but for modelling purpose in the present pioneering study, a basic configuration where the ocean bottom is horizontal is considered as a model case and is not applied to a particular real ocean bottom topography.

The lubricated gravity flow of one liquid in another liquid upon a horizontal plane was investigated earlier in a unidirectional configuration (figure 2.7) by Fay (1969), Hoult (1986), Britter (1979), Didden & Maxworthy (1982) and Huppert (1982), Kowal & Worster (2019).

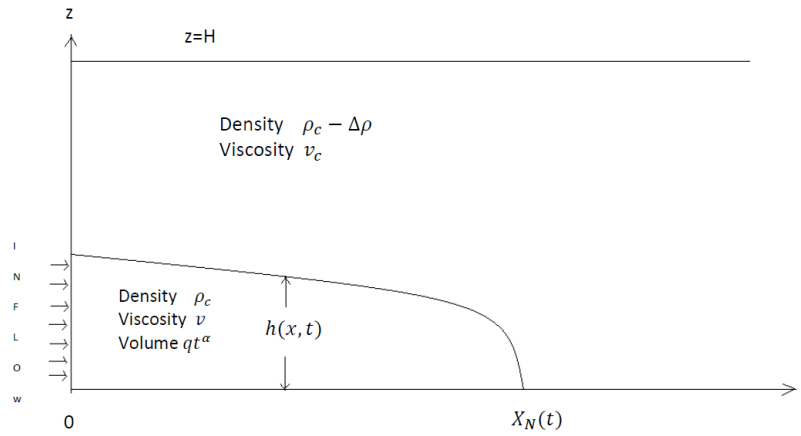

Figure 2.7: Intrusion of a dense liquid in a lighter ambient liquid upon a horizontal plane

For modeling in lubrication theory, the vertical velocity w is negligibly small as compared to the horizontal velocity u, then the longitudinal pressure gradient in the current can be written

$$\frac{\partial p}{\partial x} = (\Delta\rho) g \frac{\partial h(x,t)}{\partial x} \tag{2.79}$$

where $\Delta\rho = \rho - \rho_0$ (2.80)

while the Navier Stokes equations reduce to its projection in the x-direction in the following form:

$$0 = -\frac{1}{\rho}\frac{\partial p}{\partial x} + \nu \frac{\partial^2 u}{\partial z^2} \tag{2.81}$$

Inserting Equ.(2.79) in the latter,

$$0 = -\frac{\Delta\rho}{\rho} g \frac{\partial h}{\partial x} + \nu \frac{\partial^2 u}{\partial z^2} \tag{2.82}$$

Self-similar solutions are then sought in the following form

$$x_N = Kt^{\beta}\ ;\ h = \frac{q}{K} t^{\alpha-\beta} f\left(\frac{x}{x_N(t)}\right) \tag{2.83}$$

where x_N is the abscissa of the current front.

The configuration considered in this paper is more realistic. Oil escaping from tanker tanks lying on the ocean floor (e.g. the Prestige oil spill, S. Castanedo et al. (2005)) spreads in two opposite directions, left (index l) and right (index r) as shown in figure 2 and the stability of the flow is investigated, i.e. the decay or the growth of a small disturbance introduced in that basic flow.

The paper is organized as follows. First, the equations governing the steady basic flow are stated and solved. Then a linear stability stability is proposed. In the fourth section, numerical simulations are presented in the case of a miscible system for generalization and finally, the fifth section is devoted to discussion of the results and conclusions.

2.4.2 Basic steady flow

We consider the bi-directional lubricated flow with one right-moving lane and another left-moving lane over a horizontal plane, as shown in figure 2.8. We denote the height of the interface between the lower fluids (gravity current) and the upper one (ambient fluid) by $h(x,y,t)$, which includes $\vec{h}(x,y,t)$ for the right-moving lane interface and $\overleftarrow{h}(x,y,t)$ for the left-moving lane interface such that $h(x,y,t) = \vec{h}(x,y,t) + \overleftarrow{h}(x,y,t)$. Similarly, we denote the upper surface height by $H(x,y,t)$ which includes $\vec{H}(x,y,t)$ for the right-moving lane upper surface and $\overleftarrow{H}(x,y,t)$ for the left-moving lane upper surface, such that $H(x,y,t) = \vec{H}(x,y,t) + \overleftarrow{H}(x,y,t)$.

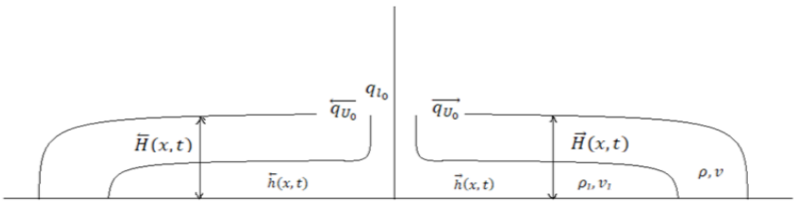

Figure 2.8: Flow configuration

a) Equations of motion

The fluxes in the lower (index l) and in the upper layer (index u) are obtained from the equations of conservation of mass and momentum in the right-moving lane write:

$$\frac{\partial \vec{h}}{\partial t} = -\frac{\partial \vec{q}_l}{\partial x} \quad ; \quad \frac{\partial\left(\vec{H} - \vec{h}\right)}{\partial t} = -\frac{\partial \vec{q}_u}{\partial x} \tag{2.84}$$

$$\mu \frac{\partial^2 u_u}{\partial z^2} = \frac{\partial p_u}{\partial x} \quad ; \quad \mu_l \frac{\partial^2 u_l}{\partial z^2} = \frac{\partial p_l}{\partial x} \tag{2.85}$$

The left-moving lane is described by analogous equations.
Three dimensionless parameters arise from this system of equations, namely the dynamic viscosity ratio $\omega = \frac{\mu}{\mu_l}$, the dimensionless density difference $D = \frac{\rho_l - \rho}{\rho}$

and the flux ratio between the two sheets given by $Q_1 = \frac{\vec{q}_{l0}}{\vec{q}_0}$ in the left-moving lane and $Q_2 = \frac{\overleftarrow{q}_{l0}}{\overleftarrow{q}_0}$.
The solution to this system gives the fluxes in the different lanes respectively as:

$$q_l = -\left[\frac{\omega}{3}h^3\left(D\frac{\partial h}{\partial x} + \frac{\partial H}{\partial x}\right) + \frac{\omega}{2}h^2(H-h)\frac{\partial H}{\partial x}\right] \tag{2.86}$$

$$q_u = -\left[\frac{1}{3}(H-h)^3\frac{\partial H}{\partial x} + \frac{\omega}{2}h^2(H-h)\left(D\frac{\partial h}{\partial x} + \frac{\partial H}{\partial x}\right) + \omega h(H-h)^2\frac{\partial H}{\partial x}\right] \tag{2.87}$$

b) Steady solution
The mass conservation equation can be solved analytically to get the two-dimensional steady solution (index s) in the following form:

$$\vec{H}_s = A(1-x)^{1/4} \quad ; \quad \vec{h}_s = a(1-x)^{1/4} \tag{2.88}$$

we get the steady state solution from Equ. (2.84) in the form:

$$\vec{q}_l = \frac{1}{4}\left[\frac{\omega}{3}a^3(Da + A) + \frac{\omega}{2}a^2A(A-a)\right] \tag{2.89}$$

$$\vec{q}_u = \frac{A^4 - aA^3 + 3a^2A^2 - a^3A}{12} + \frac{\omega a\left[4A^3 + aA^2(1-4D) + a^2A(3+D) - Da^3\right]}{8} \tag{2.90}$$

where a and A depend on the dimensionless parameters via the following system:

$$\frac{1}{4}\left[\frac{\omega}{3}a^3(Da + A) + \frac{\omega}{2}a^2A(A-a)\right] = Q \tag{2.91}$$

$$\frac{1}{4}\left[\frac{1}{3}(A-a)^3A + \frac{\omega}{2}a^2(A-a)(Da + A) + \omega aA(A-a)^2\right] = 1 \tag{2.92}$$

The interdependence between a and A is shown in fig.2.9a and fig.3.9b for where $\vec{q}_l$ and $\vec{q}_u$ respectively, and with the following arbitrary set of values for the dimensionless parameters: $D = 0.004$; $\mu = 0.5$ and $Q = 10$ and A.

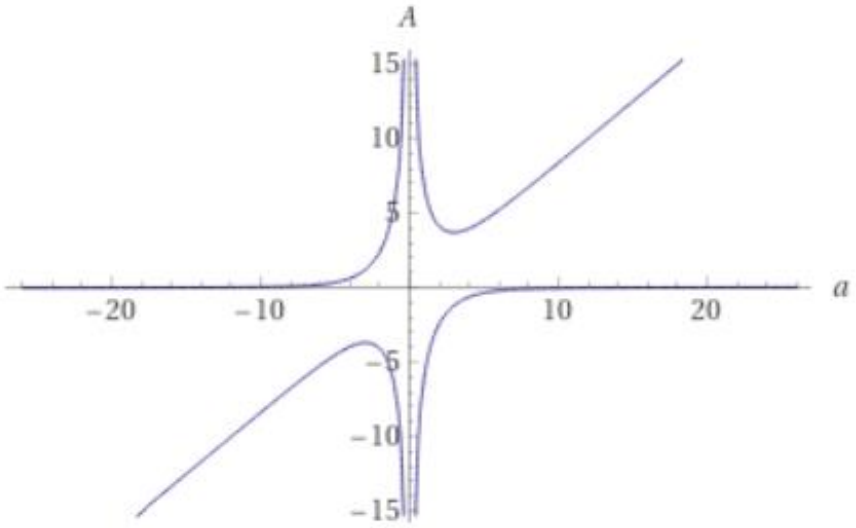

Figure 2.9a: Interdepence between a and A in $\vec{q}_l$ for assigned values to the non dimensional parameters

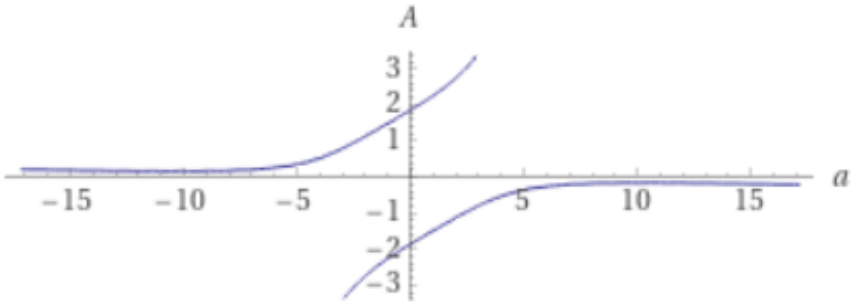

Figure 2.9b: Interdepence between a and A in $\vec{q}_u$ for assigned values to the non-dimensional parameters

2.4.3 Stability analysis

To analyze the local stability, a small perturbation is superimposed on the steady basic flow then normal-mode solutions and asymptotic solution near the singular front are sought.

a) Linear perturbation equations

In the right-moving lane, we superimpose small perturbations (index p) such that $\vec{H}_p, \vec{h}_p << 1$ to the previous steady solution. Substituting the heights of the resulting flow, say $\vec{H} = \vec{H}_s + \vec{H}_p$ and $\vec{h} = \vec{h}_s + \vec{h}_p$ in Equs.(2.86)-(2.89), we get:

$$\vec{q}_{lp} = -\left[\frac{\omega}{3}\vec{h}_s^3\left(D\frac{\partial \vec{h}_p}{\partial x} + \frac{\partial \vec{H}_p}{\partial x}\right) + \frac{\omega}{2}\vec{h}_s^2\left(\vec{H}_s - \vec{h}_s\right)\frac{\partial \vec{H}_p}{\partial x}\right]...$$

$$-\left[\omega\vec{h}_s^2\vec{h}_p\left(D\frac{\partial \vec{h}_s}{\partial x}\right) + \frac{\omega}{2}\left(\vec{h}_s^2\left(\vec{H}_p - \vec{h}_p\right) + 2\vec{h}_s\vec{h}_p\left(\vec{H}_s - \vec{h}_s\right)\right)\frac{\partial \vec{H}_s}{\partial x}\right] \qquad (2.93)$$

$$\vec{q}_{up} = -\left[\frac{1}{3}\left(\vec{H}_s - \vec{h}_s\right)^3\frac{\partial \vec{H}_p}{\partial x} + \frac{\omega}{2}\vec{h}_s^2\left(\vec{H}_s - \vec{h}_s\right)\left(D\frac{\partial \vec{h}_p}{\partial x} + \frac{\partial \vec{H}_p}{\partial x}\right)\right]...$$

$$-\left[\omega\vec{h}_s\left(\vec{H}_s - \vec{h}_s\right)^2\frac{\partial \vec{H}_p}{\partial x} + \left(\vec{H}_s - \vec{h}_s\right)^2\left(\vec{H}_p - \vec{h}_p\right)\frac{\partial \vec{H}_s}{\partial x}\right]...$$

$$-\left[\frac{\omega}{2}\left(2\vec{h}_s\vec{h}_p\left(\vec{H}_s - \vec{h}_s\right) + \vec{h}_s^2\left(\vec{H}_p - \vec{h}_p\right)\right)\left(D\frac{\partial \vec{h}_s}{\partial x} + \frac{\partial \vec{H}_s}{\partial x}\right)\right]...$$

$$-\left[\omega\left(\vec{h}_p\left(\vec{H}_s - \vec{h}_s\right)^2 + 2\vec{h}_s\left(\vec{H}_s - \vec{h}_s\right)\left(\vec{H}_p - \vec{h}_p\right)\right)\frac{\partial \vec{H}_s}{\partial x}\right] \qquad (2.94)$$

b) Normal-mode Solutions

Let the small perturbations take the form $\vec{h}_p = \tilde{\vec{h}}(x)e^{\sigma t + iky}$ and $\vec{H}_p = \tilde{\vec{H}}(x)e^{\sigma t + iky}$. Substituting now Equs. (2.90) in the previous linearized flux equation and mass conservation equation, if we set $\xi = 1 - x$ and we write the system compactly in matrix form, we obtain the following system

$$\sigma C v = \left(\xi^{3/4}\vec{E}v' - \frac{1}{4}\xi^{-1/4}\vec{F}v\right)' - K^2\xi^{3/4}\vec{E}v \qquad (2.95)$$

where

$$E = \begin{bmatrix} \frac{\omega D}{3}a^3 & \left\{\frac{\omega}{3}a^3 + \frac{\omega}{2}a^2(A-a)\right\} \\ \frac{\omega D}{2}a^2(A-a) & \left\{\frac{1}{3}(A-a)^3 + \frac{\omega}{2}a^2(A-a) + \omega a(A-a)^2\right\} \end{bmatrix} \qquad (2.96)$$

$$C = \begin{bmatrix} 1 & 0 \\ -1 & 1 \end{bmatrix} \quad ; \quad \vec{F} = \begin{bmatrix} \vec{F}_{11} & \vec{F}_{12} \\ \vec{F}_{21} & \vec{F}_{22} \end{bmatrix} \quad ; \quad \vec{F}_{12} = \frac{\omega}{2}a^2A \qquad (2.97)$$

$$F_{11} = \omega a^2(Da + A) + \frac{\omega}{2}\left[-a^2A + 2aA(A-a)\right] \qquad (2.98)$$

$$\vec{F}_{21} = -(A-a)^2A + \frac{\omega}{2}\left[2a(A-a) - a^2\right](Da + A) + \omega(A-a)\left[(A-a) - 2a\right]A$$

$$F_{22} = A(A-a)^2 + \frac{\omega}{2}a^2(Da + A) + 2\omega a(A-a)A \qquad (2.99)$$

c) Asymptotic solution near the singular front

For the right-moving lane, let us explore the asymptotic behavior of the perturbations in an inner region of size $\varepsilon \ll 1$ about $\xi = 0$, and define an inner variable

$$\varsigma = \xi / \varepsilon \tag{2.100}$$

By using Equ. (2.97) and **e**xpanding the solution as a series with the form

$$v = v_0 + \varepsilon v_1 + \varepsilon^2 v_2 ... \tag{2.101}$$

gives

$$\left(\sigma C \varepsilon^{5/4} + K^2 \varsigma^{3/4} \varepsilon^2 \vec{E}\right)\left(v_0 + \varepsilon v_1 + \varepsilon^2 v_2 + ...\right)$$

$$= \frac{d}{d\varsigma}\left[\varsigma^{3/4}\vec{E}\left(\frac{d}{d\varsigma}v_0 + \varepsilon\frac{d}{d\varsigma}v_1 + ...\right)\right] + \frac{d}{d\varsigma}\left[\frac{1}{4}\varsigma^{-1/4}\vec{F}\left(v_0 + \varepsilon v_1 + \varepsilon^2 v_2 + ...\right)\right] \tag{2.102}$$

At leading order in ε, Equ. (3.102) reduces to

$$\frac{d}{d\varsigma}\left(\varsigma^{3/4}\vec{E}\frac{d}{d\varsigma}v_0 + \frac{1}{4}\varsigma^{-1/4}\vec{F}v_0\right) = 0 \tag{2.103}$$

with general solution

$$v_0 = \varsigma^{1/4}A_0 + \varsigma^{-M}B_0 \tag{2.104}$$

d) Analytical results

A flow is said to be stable if a small disturbance introduced into it increases and unstable if it decreases. In order to decide in the present case, we need to determine the sign of the growth rate of the disturbance. In this aim, we must solve the following equation for σ:

$$\sigma C v = \left(\xi^{3/4}\vec{E}v' - \frac{1}{4}\xi^{-1/4}\vec{F}v\right)' - K^2\xi^{3/4}\vec{E}v \tag{2.105}$$

After algebraic calculations, we find that $\sigma \leq 0$, which means that the system is stable to all perturbations whatever the choice of the three dimensionless parameters ω, D and Q. This result is in agreement with that obtained by Kowal & Worster (2019).

2.4.4 Numerical simulations

In order to get a first idea of the numerical simulations that will be carried out during the work. We present an overview of the OpenFOM structure.
OpenFoam is an acronym for (Open Field Operation and Manipulation), It can be defined as an open-source software suite written in C++, was originally developed in the late 1980's at Imperial College, London, to solve continuum mechanics problems. It contains many solvers to address fluid motion problems, these programs can be implemented after making some changes to suit for the problems we wish to address.

The structure of OpenFOAM is consisit of: pre-processing, solving and post-processing as shown in the following diagram:

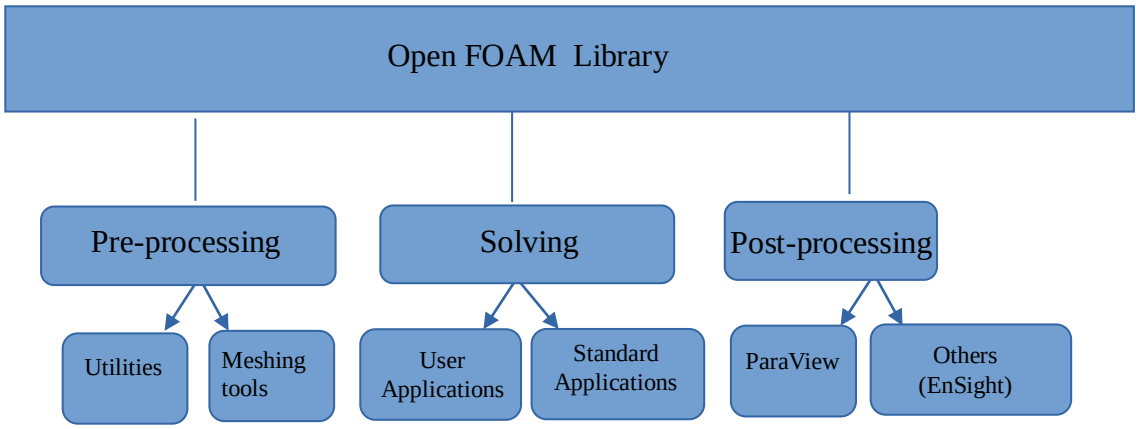

Figure 2.10 .The structure of OpenFOAM.

The pre processing environment gives the possibility to create a mesh (block Mesh utility), selection of the physical phenomena that need to be modelled definition of fluid properties and specification of appropriate boundary conditions at cells.

A solver environment, which is used to solve the governing equations of the flow subject to the conditions provided. The method used as a flow solver is finite volume method.
The post-processing environment supplied with OpenFOAM is ParaView, an open source visualization application. post-processing utilities allow us to display the simulation results as desired by the user and allow user to convert the results of simulations into data or graphs.Also there is a plugin (paraFoam) for visualisation of solution data and meshes in ParaView.

Every OpenFOAM case consists of a directory structure containing specific files that are required to run the simulation.We can describe the Directory tree of a generic OpenFOAM case as follows:

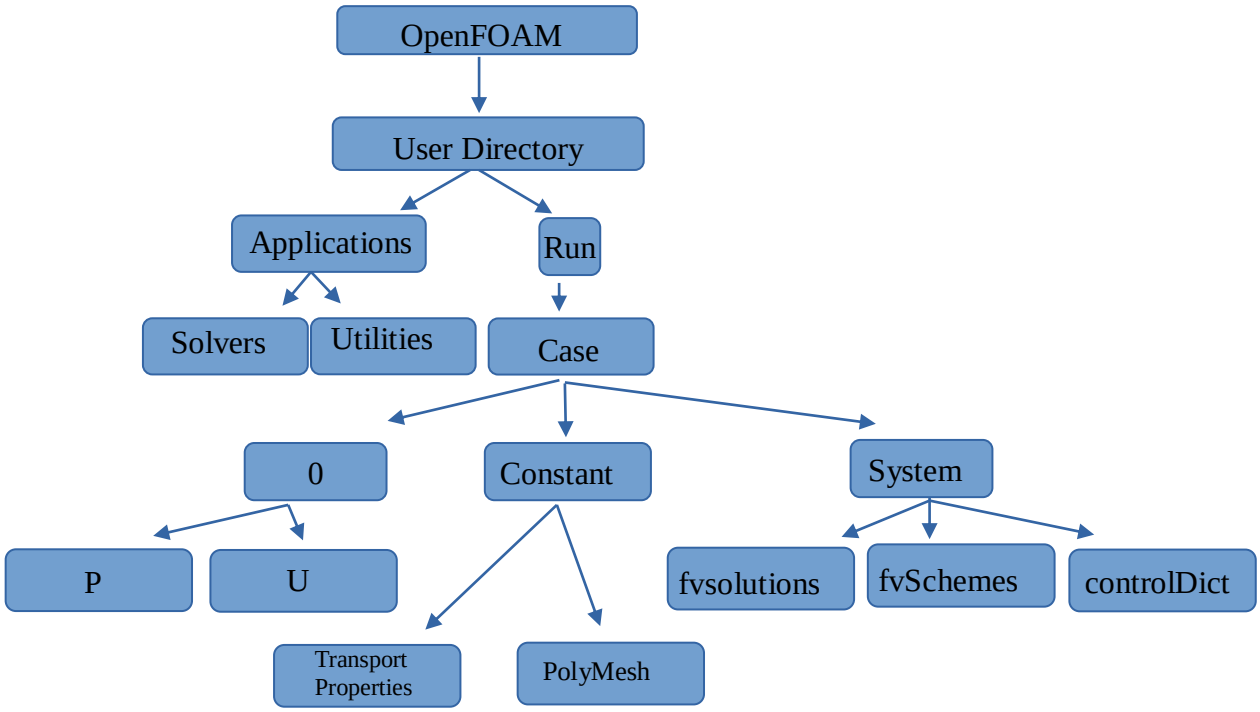

Figure 2.11 Directory tree of a generic OpenFOAM case

2.4.4.1 OpenFOAM Case

To simulate any problem using OpenFOAM, we always need three folders to be present: system, constant, and "time" folders. These three folders contain all the information needed to run a simulation and each directory is responsible for an important part of the simulation process.

1- A system folder contains the specifications for the simulation and includes at least the following three files: controlDict, fvSchemes, fvSolution. Each directory has the following task:

ControlDict is used to determine time the start and end time, time steps, and data output parameters are set. fvSchemes contains the discretization schemes and the algorithms which is used in the simulation. where discretisation schemes used in the solution may be selected at run-time.

fvSolution contains the linear solvers for the sequential equations, tolerances and other algorithm controls, where the equation solvers, tolerances and other algorithm controls are set for the run.
This is in addition tothe blockMesh tool is being used to prepare the mesh.

2- A constant folder contains files that are related to the physics of the problem, It contains two important sub-directories-the polyMesh folder, which contains the mesh information, and at least one file containing the physical properties of the system, typically the transportProperties file. This folder contains specifications for turbulence and fluid properties. Depending on the solver chosen, and the type of turbulence model applied is determined in turbulenceProperties where either LES, RAS or laminar model can be chosen. For incompressible solvers the file transportProperties determines the behavior of the kinematic viscosity ν.

3- The 0 directory is a special time directory that contains the initial condition(s) for the simulation. zero folder (or 'time' folder) contain the data files in time step 0 file, these data can either be initial or boundary conditions that the user has specified.

2.4.5 Numerical Model

In order to generalize the previous analytical result, the intrusion of a dense gravity current beneath a lighter miscible ambient liquid has been simulated numerically. The Navier-Stokes equations coupled to the advection-diffusion equation for the volume of the salt water fraction are used to describe the dynamics of the mixture density and the viscosity of the flow. The open-source code provided in OpenFOAM with a collection of C++ libraries was used to compute the flow. Specifically, the (TwoLiquidMixingFoam) solver was used in our simulations (Ahmed et al., 2018).

a) Equations

The Navier-Stokes equations coupled to the advection-diffusion equation for such miscible system (e.g. intrusion of a volume of salt water beneath a large volume of fresh water) are used to describe the dynamics of the mixture density and the viscosity of the fluid.

$$\frac{\partial u_i}{\partial x_i} = 0 \tag{2.106}$$

$$\frac{\partial(\rho u_i)}{\partial t} + \frac{\partial(\rho u_i u_j)}{\partial x_j} = -\frac{\partial p}{\partial x_i} + \frac{\partial}{\partial x_j}\left(\mu \frac{\partial u_i}{\partial x_j}\right) - \rho g \delta_{i3} \tag{2.107}$$

$$\rho = c(\rho + \Delta\rho) + (1-c)\rho \tag{2.108}$$

$$\frac{\partial c}{\partial t} + \frac{\partial(u_i c)}{\partial x_i} = \frac{\partial}{\partial x_i}\left(D_m \frac{\partial c}{\partial x_i}\right) \tag{2.109}$$

where u_i denotes the velocity in the x_i -directions (also referred as x , y and z); p is the pressure field; μ and ρ are the density and the density of the saline mixture, respectively; g is the gravitational acceleration acting along the x_3 (or z) direction, δ_{ij} is the Kronecker delta and $D_m = 1.5\times10^{-9} m^2 s^{-1}$ is the molecular diffusion of the salt water.

The flow domain consists of a parallelepiped with a small inlet of rectangular section (red colour in figure 4), with length $5\times10^{-1} m$, width $15\times10^{-2} m$ and height $7\times10^{-2} m$.

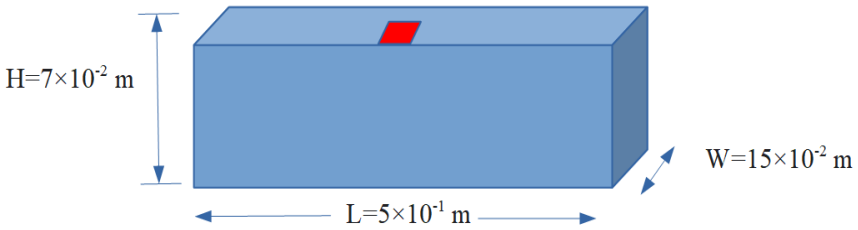

Figure 2.12a: Global view of the flow domain

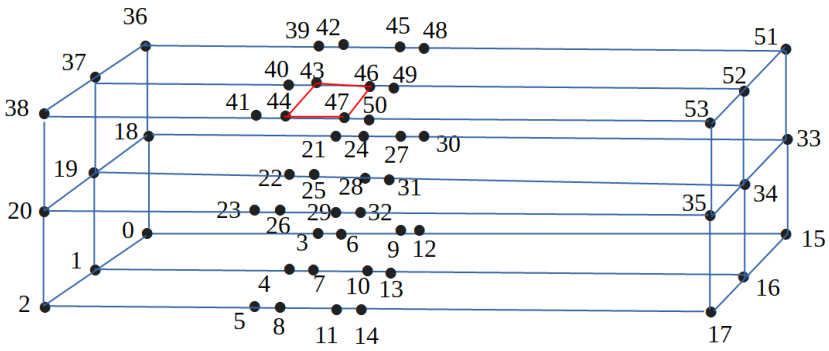

Figure 2.12b: Edges and vertices of the flow domain

b) Numerical procedure

The previous set of equations was solved using the volume of fluid method (VOF). The density ρ and the viscosity μ were determined in each cell by the volume fraction of the salt water c as follows. The density variation in a cell is due only to the difference in density between salt water and fresh water because the temperature is kept constant. Consequently, the state equation governing the viscosity reads as:

$$\mu = c\mu_1 + (1-c)\mu_2 \qquad (2.110)$$

where $\mu_1 = 1.04\times10^{-3} Pa\cdot s$ and $\mu_2 = 10^{-3} Pa\cdot s$ and subscripts 1 and 2 stand for salt water and fresh water respectively.

A similar procedure was used for the density. According to the state equation of the density, the mixture density varies linearly with the volume fraction because ρ_1 and ρ_2 were kept constant in the numerical calculations.

The (TwoLiquidMixingFoam) solver was used to solve the set of equations described previously with start time = 0, end time=$10s$ and time increment = $0.5s$. The velocity was uniform in the inlet with components U (0 ; -0.1m/s ; 0) while the non-slip condition was applied at the flow boundaries: left and right edges, bottom and atmosphere as well. The kinematic viscosity and density were taken

as $\nu_1 = 10^{-6} m^2 s^{-1}$ and $\rho_1 = 1040 kg/m^3$ for salt water and $\nu_2 = 2 \times 10^{-6} m^2 s^{-1}$ and $\rho_2 = 1000 kg/m^3$

c) Numerical results

Figure2.13presents the propagation of the gravity current from the top view, i.e. in the $(x - y)$ plane.

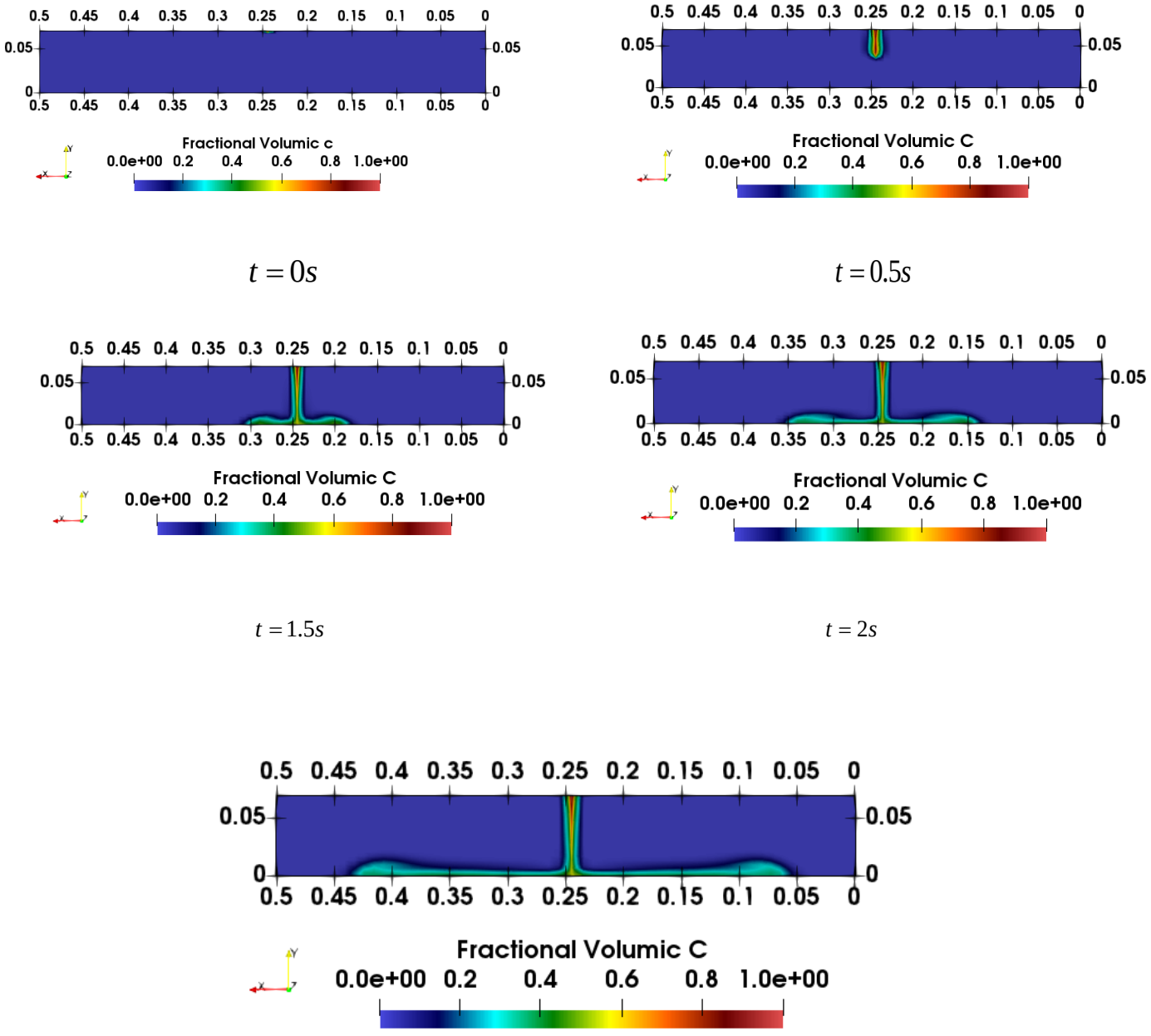

$t = 0s$ $t = 0.5s$

$t = 1.5s$ $t = 2s$

$t=2.5s$

Figure 2.13: Numerical simulations of the propagation of a bidirectional gravity-current in a miscible lighter liquid

The flow is uniform in the inlet and as it reaches the bottom, it breaches off in a two-way flow called bidirectional gravity-current. Then it drains into the ambient lighter fluid in both a left-moving lane and right-moving lane.

It was notably found that the velocity of the inner layer is less than the flow velocity of the outer layer and therefore, the inner layer remains behind the outer layer throughout the flow period as found also by Dhafar et al. (2018).

Moreover, it was found that the maximum depth of the head of the gravity-current depends both on spatiotemporal evolution and on density threshold, while the head of the gravity current does not show any show from the bottom of the basin so, the hydroplaning phenomenon was not observed in these numerical simulations. In contrast, the hydroplaning phenomenon on gravity currents was observed experimentally by La Rocca (2008) and was examined in detail by Mohrig et al. (1998) for subaqueous debris flow.

Finally, as can be observed in figure 5, no waves appeared in the flow, which shows that the flow is stable as stated for non miscible system in the previous section.

2.4.6 Discussion and Conclusions

In this paper, the stability of a lubricated viscous bidirectional gravity current on a horizontal plane was considered as model configuration. In this aim, a local analysis in an inner region near the lubrication front in the two directions was performed and matched asymptotically. Notably, the large wavenumber stabilization by transverse shear stress was investigated in two dynamical regimes: i/ a regime in which the wavelength of the perturbations is much smaller than the thickness of both layers and of both directions in which case the perturbations are resisted dominantly by horizontal shear stress and an intermediate regime in which both vertical and horizontal shear stresses are important; ii/ the origins of the internal instability arising from internal dynamics are analyzed. Then the linear stability of the steady basic flow was brought out in terms of normal-mode solutions. Notably, it was shown that the flow is stable to all perturbations, whatever the choice of the three dimensionless parameters.

2.5 Stability of viscous lubricated thin film down an inclined plane beneath ambient lighter non miscible static liquid

This subsection considers the stability of a thin film propagating beneath a large quantity of ambient static non miscible lighter liquid and over a sloping plane. Such configuration that has never been considered earlier can model the spill of a heavy hydrocarbon into the ocean by a tanker. Equations of conservation of the mass and the momentum were appropriately made non dimensional and a similar solution is proposed in this paper. In this way, an analytical expression of the hydrodynamic field, say velocity field and pressure field is provided. Then, the equation governing the spatiotemporal evolution of the water-oil interface was built and solved by a perturbation method. Also, the time evolution of the wave front position along the inclined plane was built. Finally, the effect of the control parameters on the linear stability of the flow was investigated.

2.5.1 Introduction

Oil spills can be caused by the accidental (ruin of the material constituting the tank) or intentional (degassing or act of war) spillage of a large quantity of oil from an oil tanker into the ocean. The collection, destruction, and storage of the oil that ran aground on the coast, as well as the coast cleaning are arduous, dangerous and expensive tasks for the populations living in these soiled territories (Tansel, 2014; French-McCay, 2004; Reed et al., 1999).

The oil which is spilled in the ocean undergoes three main phenomena: entrainment on the ocean surface on the one hand and at the ocean bottom on the other hand and evaporation as well as physico-chemical reactions with the medium in which it evolves. Moreover, to date, no universal law makes it possible to determine a priori the respective proportions of oil in these three processes. Therefore, an oil spill is a complex phenomenon of which each process must firstly be controlled before they are put into competition by a relevant modeling.

In this work, we study the 1D propagation of a fixed volume of dense fluid (with density ρ_2 and kinematic viscosity ν_2) released from a reservoir to the bottom of a large body of ambient lighter non miscible liquid, static water in this case (with density ρ_1 and kinematic viscosity ν_1). Based on this description, the phenomenon studied is defined as a lubricated (a flow in which one dimension, thickness in this case, is significantly smaller than the others) viscous (the inertial terms in the momentum equation can be neglicted versus the viscous ones) film flow. The ocean is not flat so, for modelling purpose in the present pioneering study, a basic configuration where the ocean bottom is an inclined plane is considered as a basic case and is not applied to a particular real ocean bottom topography. Consequently, the flow is controlled by gravity, oil/water density difference, oil viscosity and surface tension.

The lubricated gravity flow of one liquid in another liquid upon a horizontal plane (termed as gravity current) was investigated earlier in a unidirectional configuration (figure 3.12) by Fay (1969), Hoult (1986), Britter (1979), Didden & Maxworthy (1982) and Huppert (1982), Kowal & Worster (2019).

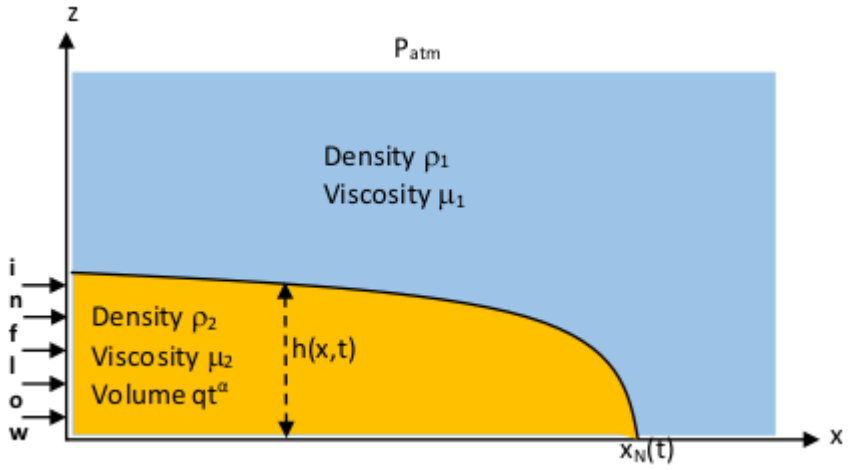

Figure 2.14: Intrusion of a dense liquid in a lighter ambient liquid upon a horizontal plane (Huppert, 1982)

In lubrication theory, the Navier Stokes equations describing the one-dimensional lubricated intrusion (in x-direction) of a dense gravity current beneath a static large volume of lighter static ambient liquid reduce to its projection in the x-direction in the following form :

$$0 = -\frac{1}{\rho}\frac{\partial p}{\partial x} + \nu\frac{\partial^2 u}{\partial z^2} \tag{2.111}$$

where the longitudinal pressure gradient in the current can be written

$$\frac{\partial p}{\partial x} = (\Delta\rho) g \frac{\partial h(x,t)}{\partial x} \tag{2.112}$$

with $\Delta\rho = \rho - \rho_0$ (2.113)

Inserting Equ. (2.112) in Equ. (2.111), we get

$$0 = -\frac{\Delta\rho}{\rho} g \frac{\partial h}{\partial x} + \nu\frac{\partial^2 u}{\partial z^2} \tag{2.114}$$

Self-similar solutions are then sought in the following form

$$x_N = Kt^{\beta} \; ; \; h = \frac{q}{K} t^{\alpha-\beta} f\left(\frac{x}{x_N(t)}\right) \tag{2.115}$$

where x_N is the abscissa of the current front.

Hydrodynamic stability is a fundamental topic of the fluid dynamics curriculum in schools of engineering. A laminar flow is said to be stable if a small disturbance superimposed on it vanishes over time. The flow is unstable if this small disturbance increases or remains constant over time. The aim of this work is to point out the control parameters that promote instability in order to provide reliable information to contribute to the protection of the ocean. Since Kapitza's original work on stability of film flow over an inclined plane (Kapitza &Kapitza, 1949), many papers have been published on this topic (e.g.: Yih, 1955; 1963, Benjamin, 1957; Kao, 1964 among others). They found that the critical Reynolds number Re_c, i.e. the threshold above which some disturbances will be amplified depends only on the slope and is given by

$$\mathrm{Re}_c = \frac{5}{6}\cot\theta \tag{2.116}$$

Moreover, very short waves are damped by surface tension. Kao (1964) extended that basic configuration to flow of a binary system of two layers of viscous fluids of different densities. More recently, the shallow water models (e.g. : Ruyer-Quil & Manneville, 1998 ; 2000) provide a good understanding of the stability of Newtonian fluids. For power-law fluids, Ng. & Mei (1994) as well as Hwang & al. (1994) built lubrication models while Nsom et al. (2019) proposed a generalized Orr-Sommerfeld model with appropriate definition of non-dimensional numbers. All of the models existing in literature were restricted to the case where the flow develops in the atmosphere, while in the present paper, the case where the ambient fluid is a large volume of static non miscible liquid is tackled.

The work is organized as follows. In the second section, the flow configuration is presented and the equations of motion are presented and made non-dimensional. These equations of motion are solved and the hydrodynamic field as well as the interface profile are derived in the third section. The fourth section is devoted to the linear stability where Orr-Sommerfeld equation is built and solved by the method of perturbation and notably the effects of the different control parameters on the linear stability of the flow are respectively pointed out. Finally, the fifth presents a discussion and the conclusions.

2.5.2 Problem statement

a) Flow configuration

We consider a fixed quantity of a dense viscous Newtonian fluid (heavy crude oil) spilled at time $t = 0^-$ upon an inclined plane in the form of a thin film beneath a large quantity of static lighter non miscible liquid (sea water in this case) between abscissa film tail $(x = -l)$and film front $(x = 0)$. Downstream, the film front is occupied by the ambient static liquid. At initial time, $t = 0^+$ the film flows downstream the sloping plane with slope θ and length L, with $L >> l$ and beneath the ambient static liquid. The width of the flow system is infinite.

The quantities referring to lighter ambient static liquid have the subscript 1, while those referring to the heavy viscous liquid contained in the reservoir at negative time and that will undergo the flow have the subscript 2. Typically, we have $\rho_2 > \rho_1$.

The flow configuration is presented on figure 2.13.

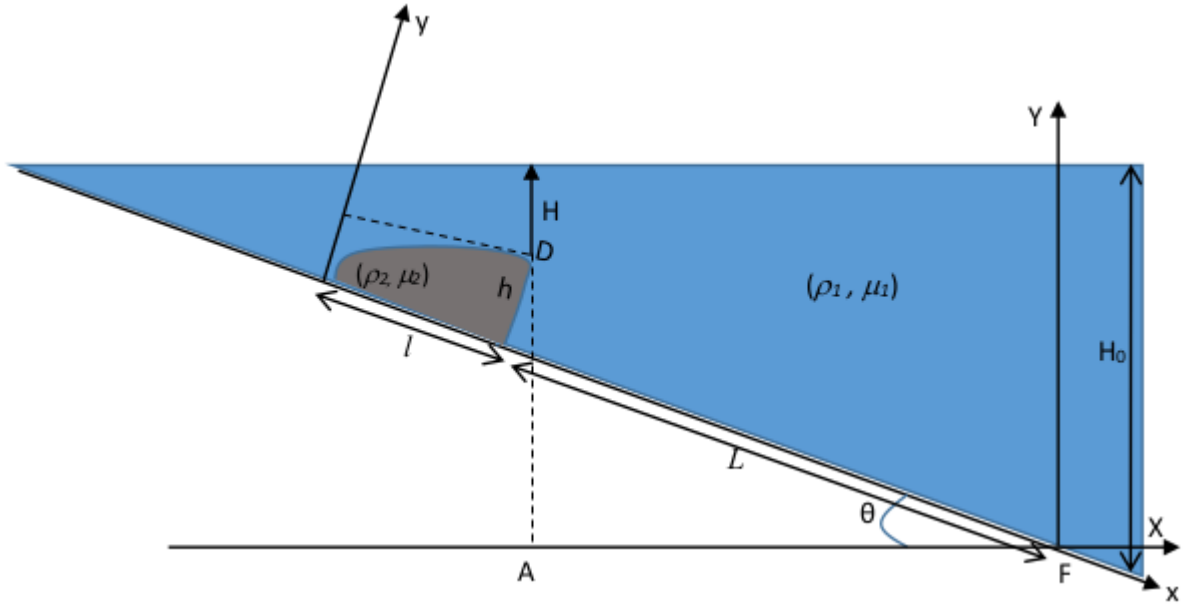

Figure 2.15: Flow configuration

b) Equations of motion

If $\vec{V}_b^*(U_b^*,0,0)$ and P_b^* denote the velocity field and the pressure field in the gravity current that propagates downstream the inclined plane, the 1D flow in hand is governed by the conservation equations of the mass (Equ. (2.117)) and of the momentum (Equs.(2.118)-(2.119)). They write:

$$\frac{\partial U_b^*}{\partial x^*} = 0 \qquad (2.117)$$

which brings that $U_b^* = U_b^*(y)$

$$\rho_2\left(U_b^*\frac{\partial U_b^*}{\partial x^*}\right) = -\frac{\partial P_b^*}{\partial x^*} + \mu_2\left(\frac{\partial^2 U_b^*}{\partial (x^*)^2} + \frac{\partial^2 U_b^*}{\partial (y^*)^2}\right) + \rho_2 g \sin\theta \qquad (2.118)$$

$$0 = -\frac{\partial P_b^*}{\partial y^*} - \rho_2 g\cos\theta \qquad (2.119)$$

2.5.3 Basic laminar flow

a) Hydrodynamic field

Equ. (2.119) shows that the pressure field is hydrostatic so it writes

$$P_b^*(y) = -\rho_2 g y^* \cos\theta + B \qquad (2.120)$$

Denoting the atmospheric pressure by P_{atm}, the constant of integration B is determined by equating at the interface, the pressure in ambient liquid given by Pascal law as $P_1\,(\text{int}\,erface) = \rho_1 gH + P_{atm}$ with its value in the denser liquid given by Equ.(2.120) as $P_2\,(\text{int}\,erface) = B$. Consequently, the pressure field in the gravity current has the following expression:

$$P_b^*(y) = -\rho_2 g y^* \cos\theta + \rho_1 g\left[\left(H_0 - L\sin\theta\right) - h^*(x^*)\cos\theta\right] + P_{atm} \qquad (2.121)$$

Introducing that expression of the pressure field in Equ. (2.118), we get

$$\mu_2 \frac{d^2 U_b^*}{d(y^*)^2} = -\rho_1 g\cos\theta \frac{\partial h^*}{\partial x} - \rho_2 g \sin\theta \qquad (2.122)$$

whose general solution writes

$$\mu_2 U_b^*(y) = -g\frac{(y^*)^2}{2}\left[\rho_1 \cos\theta \frac{\partial h^*}{\partial x^*} + \rho_2 \sin\theta\right] + K_1 y^* + K_2 \qquad (2.123)$$

The constants of integration K_1 and K_2 are determined by the boundary conditions. The first boundary condition is the no slip condition at channel bed, i.e.

$$U_b^* = 0 \quad \text{at} \quad y^* = -h^* \qquad (2.124)$$

while the second boundary condition expresses the continuity of the shear stress at the interface. Assuming the ambient liquid (water) to be a perfect fluid, it writes

$$\mu_2 \frac{dU_b^*}{dy^*} = 0 \quad \text{at} \quad y^* = 0 \qquad (2.125)$$

After straightforward calculations, the velocity field is obtained with the following expression

$$U_b^*(y) = -\frac{g}{2\mu_2}\left[\rho_1 \cos\theta \frac{dh^*}{dx} + \rho_2 \sin\theta\right]\left[(y^*)^2 - (h^*)^2\right] \qquad (2.126)$$

b) Evolution equation of the interface

To form the evolution equation of the interface, the continuity equation is written in its global form, i.e.

$$\frac{\partial h^*}{\partial t^*} + \frac{\partial}{\partial x^*}\left[\int_0^h U_b^*(y^*)dy^*\right] = 0 \qquad (2.127)$$

Using the expression of the velocity field given by Equ. (2.126), the integral appearing in Equ. (2.127) writes

$$\int_0^h U_b^*(y)dy = -\frac{(\rho_2 - \rho_1)g\cos\theta}{3\mu_2}\left[(h^*)^3 \frac{\partial h^*}{\partial x} - \frac{\sin\theta}{\cos\theta}(h^*)^3\right] \qquad (2.128)$$

So, equation of continuity takes the form

$$\frac{\partial h^*(x^*,t^*)}{\partial t^*} - \frac{(\rho_2 - \rho_1)g\cos\theta}{12\mu_2}\left\{\frac{\partial^2}{\partial(x^*)^2}\left[(h^*)^4(x^*,t^*)\right] - 4tg\theta\frac{\partial}{\partial x^*}\left[(h^*)^3(x^*,t^*)\right]\right\} = 0 \qquad (2.129)$$

Assuming the following set of non-dimensional functions and variables in which the characteristic height of the gravity current H ; the characteristic abscissa is L and the characteristic longitudinal velocity U

$$h=\frac{h^*}{H} \quad ; \quad x=\frac{x^*}{L} \quad ; \quad U_b=\frac{U_b^*}{\hat{U}} \quad ; \quad \hat{U}=\frac{\left(\rho_2-\rho_1\right)H^3 g\cos\theta}{12\mu_2 L} \tag{2.130}$$

with the lubrication assumption $H << L$ and the characteristic time is derived as $T=\frac{L}{\hat{U}}$

Equ. (2.128) takes the following non-dimensional form

$$\frac{\partial h}{\partial t}-\frac{\partial^2\left[h^4\right]}{\partial x^2}+4\lambda\frac{\partial\left[h^3\right]}{\partial x}=0 \tag{2.131}$$

Parameter λ is defined as

$$\lambda=\frac{L}{H}tg\theta \tag{2.132}$$

c) Interface profile

**Spatiotemporal equation of interface profile*

Flow upon an inclined plane is governed by Equs. (2.131) whose meaning is that the convective term is balanced by the summ of the two others. Meanwhile these two tems are not of the same order of magnitude. The order of magnitude of the second term of Equ. (2.131) is $\frac{H^4}{L^2}$ while the order of magnitude of the third term is $\frac{H^3}{L}$. From the lubrication assumption the second term of Equ. (2.131) is much smaller than the third one so, it can be neglected. Consequently, Equ. (2.131) becomes

$$\frac{\partial h}{\partial t}+4\lambda\frac{\partial\left[h^3\right]}{\partial x}=0 \tag{2.133}$$

We seek similar solutions to Equ. (2.133) of the form

$$h(x,t)=D\cdot x^{\beta}\cdot t^{-\gamma} \tag{2.134}$$

where D,β,γ are constants that we can determine by inserting the form assumed for the solution Equ. (2.134) in the equation of motion (Equ. (2.133) we find

$$\beta=\gamma=1/2 \quad ; \quad D=\frac{1}{2\sqrt{3\lambda}} \tag{2.134b}$$

Inserting these values in Equ. (2.134b), the interface evolution equation writes

$$h(x,t)=\frac{1}{2\sqrt{3\lambda}}\sqrt{\frac{x}{t}} \tag{2.135}$$

Fig.2.16 and Fig.2.17 show for assigned parameter λ the variation of fluid height vs. abscissa at given time and vs. time at given abscissa, respectively. It can be noticed that the smaller parameter the greater fluid height. That flow characteristic is explained by the fact that the higher parameter λ, i.e. the higher the slope for given ratio H/L, the greater the gravity effect. Moreover, Fig. 2.16 exhibits the general space evolution of a gravity current. Immediately after the initiation of the flow, an inertial regime takes place, where inertia dominates the other effects present in the flow and the equation of a characteristic tangent is given by $h=4x$. During the development of the inertial regime, the viscous effects increase to the point of becoming dominant and the equation of a characteristic tangent is given by $h=0.75x$. The viscous regime then settles over a given distance,

until an equilibrium is reached which characterizes the asymptotic regime, where the equation of a characteristic tangent is given by $h = 0.2x$.

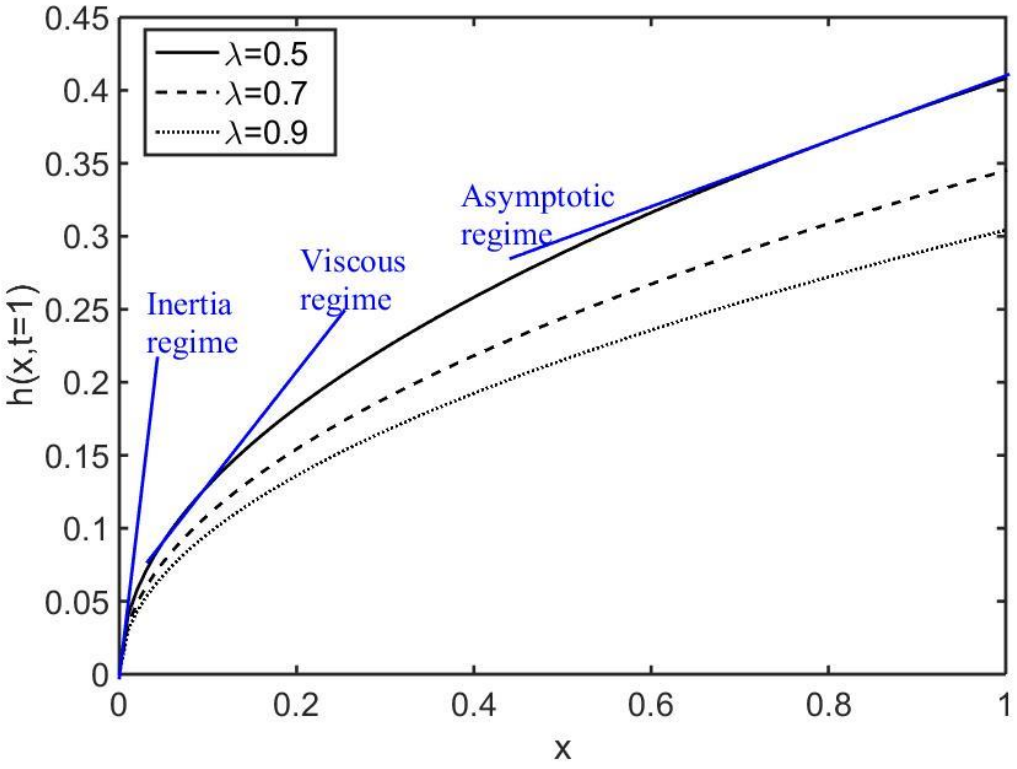

Figure 2.16 : Variation of fluid height vs. abscissa at given time and for assigned parameter λ

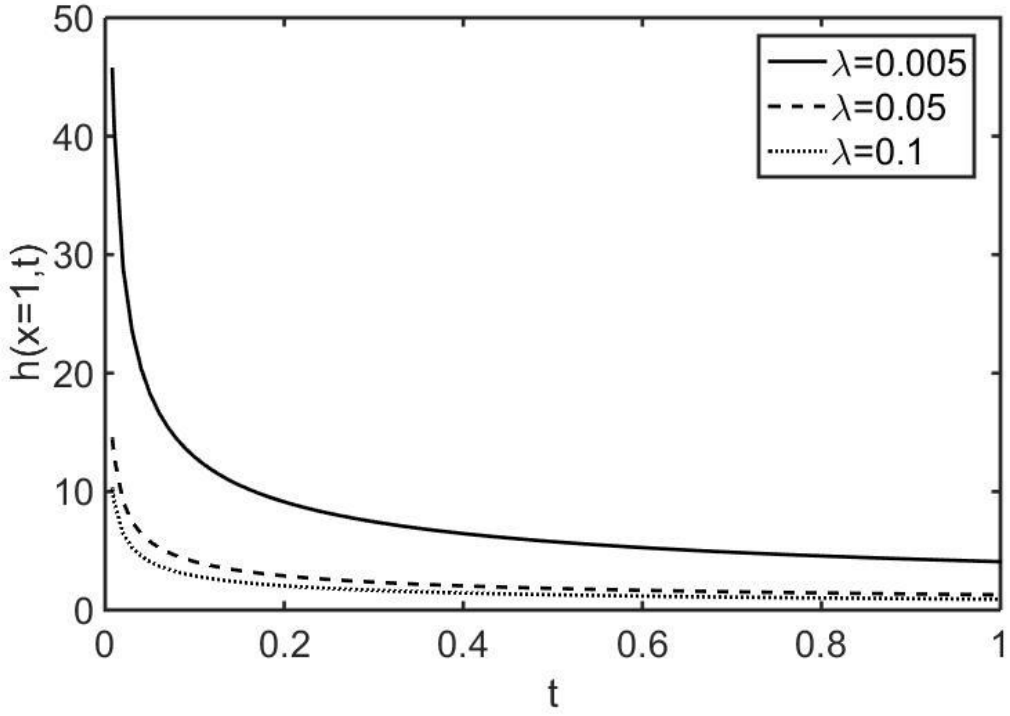

Figure 2.17 : Variation of fluid height vs. time at given abscissa and for assigned parameter λ

**Law of evolution of the front*

To determine the law of evolution of the front abscissa x_f, we state that the fluid volume V is equal to a constant δ, that is equal (see Fig.2.13) at any time *t*, per unit width in non dimensional variable to

$$\delta = \frac{l}{2L} \tag{2.136}$$

$$\frac{1}{2\sqrt{3\lambda t}} \int_0^{x_f} \sqrt{x} = \delta \tag{2.137}$$

Taking one quadrature of Equ. (2.137), we get

$$x_f = Ct^{1/3} \tag{2.138}$$

where

$$C = \left(3\lambda^{1/3} \delta^{2/3} \right) \tag{2.139}$$

Fig. 2.18 shows, for assigned value to parameter λ, the time variation of the abscissa of film front vs. parameter δ. It can be noticed that the higher parameter δ, the greater front abscissa. That flow characteristic is explained by the fact that the higher parameter δ, the greater the liquid volume and consequently the faster the flow.

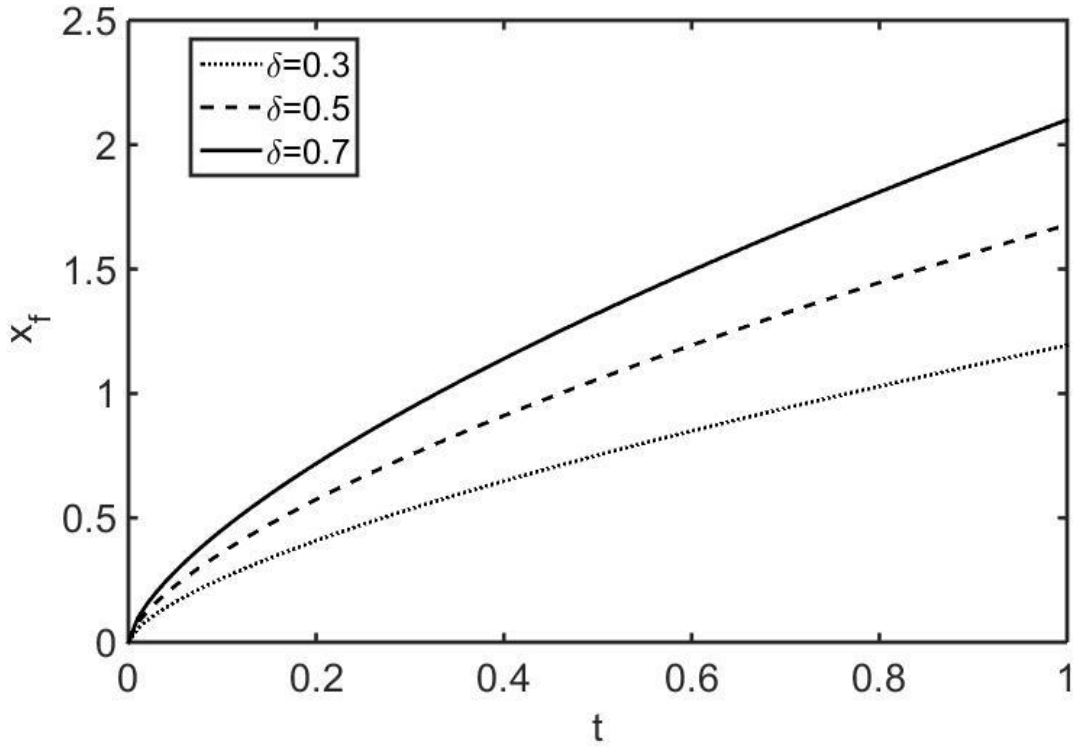

Figure 2.18 : Time evolution of front abscissa for given parameters λ and δ

2.5.4 Interface profile

Combining the results of the two previous sections, the whole interface can be shown. A master curve is obtained for given parameter λ and the front is obtained to close the interface downwards after computing front abscissa, for assigned parameter δ. As shown in Fig.2.19 where the interfaces corresponding to three flow configurations from the same master curve obtained with $\lambda = 0.5$ and the respective fronts can be drawn, considering the corresponding value of parameter δ, namely 0.3 ; 0.5 and 0.7 in this case

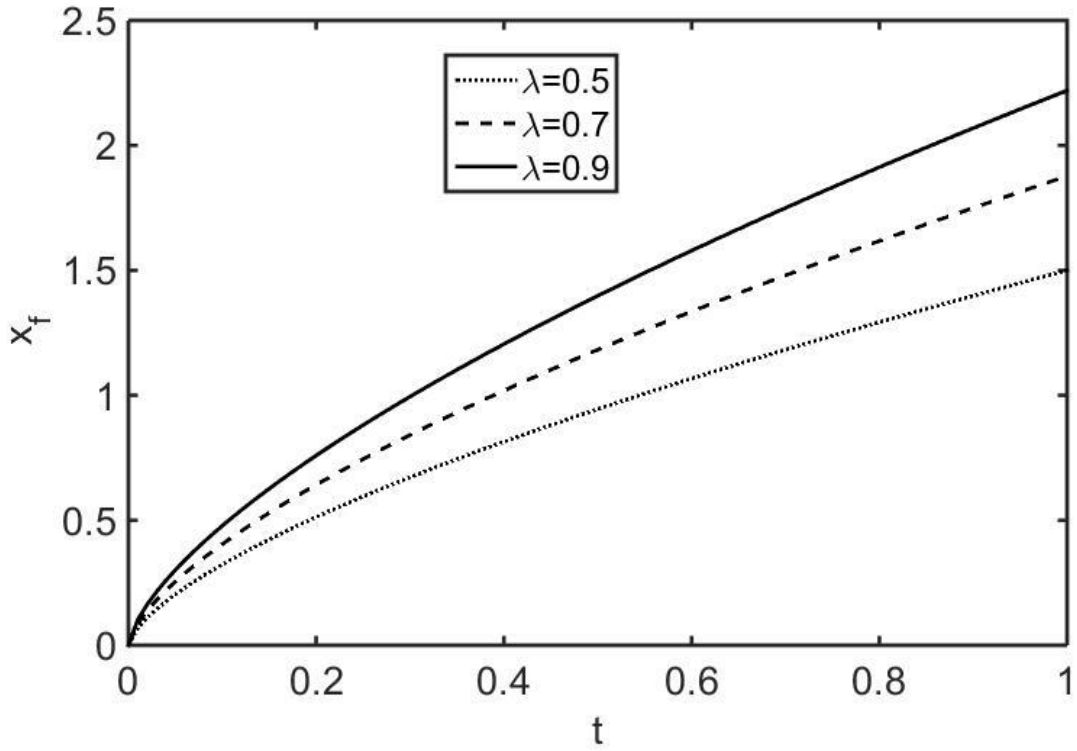

Figure 2.19 : Interface profile

2.5.5 Linear stability analysis

2.5.5.1 The Orr-Sommerfeld equation

If, from Equ. (2.126), we take the surface velocity as the reference velocity U_0, i.e.

$$U_b^*(y=0) = \frac{g}{2\mu_2}\left[\rho_1 \cos\theta \frac{dh*}{dx} + \rho_2 \sin\theta\right]\left[(h*)^2\right] \tag{2.140}$$

Then, in non dimensional form, the velocity field of the basic flow field writes

$$U(y) = 1 - y^2 \tag{2.141}$$

where the flow depth has been used as reference length defining the non dimensional normal coordinate y.

To investigate the linear stability of the previous laminar steady basic flow, a small 2D perturbation with velocity field $[u(x,y,t)]$; $[v(x,y,t)]$ and pressure field $[p(x,y,t)]$ is superimposed to the above steady basic flow. Using the characteristic length, velocity and time defined in Equ.(2.130),

the equations of conservation of mass and momentum are written in non dimensional form for the resulting hydrodynamic field $\left[\vec{U}_r\left(U_p,V_p\right),P_p\right]$ with

$$U_p = U_b(y) + u(x,y,t) \quad ; \quad V_p = v(x,y,t) \quad ; \quad P_p = P_b(x,y) + p(x,y,t) \tag{2.142}$$

in the following form:

$$\frac{\partial U_p}{\partial x} + \frac{\partial V_p}{\partial y} = 0 \tag{2.143}$$

$$\frac{\partial U_p}{\partial t} + U_p \frac{\partial U_p}{\partial x} + V_p \frac{\partial U_p}{\partial y} = -\frac{\partial P_p}{\partial x} + \frac{1}{\mathrm{Re}}\left(\frac{\partial^2 U_p}{\partial x^2} + \frac{\partial^2 U_p}{\partial y^2}\right) + \frac{1}{Fr^2}\sin\theta \tag{2.144}$$

$$\frac{\partial V_p}{\partial t} + U_p \frac{\partial V_p}{\partial x} + V_p \frac{\partial V_p}{\partial y} = -\frac{\partial P_p}{\partial y} + \frac{1}{\mathrm{Re}}\left(\frac{\partial^2 V_p}{\partial x^2} + \frac{\partial^2 V_p}{\partial y^2}\right) + \frac{1}{Fr^2}\cos\theta \tag{2.145}$$

where Reynolds number, Froude number respectively defined as

$$\mathrm{Re} = \frac{\rho_2 L U}{\mu_2} \quad ; \quad Fr = \frac{U}{\sqrt{gL}} \tag{2.146}$$

have been sorted as non dimensional control parameters of the flow.

The disturbance superimposed to the basic laminar steady flow produces a deformation $\hat{\eta}(x,y,t)$ of the interface. To satisfy identically the continuity equation, we introduce a stream function $\hat{\psi}(x,y,t)$ according to :

$$u(x,y,t) = \frac{\partial \hat{\psi}(x,y,t)}{\partial y} \quad ; \quad v(x,y,t) = \frac{\partial \hat{\psi}(x,y,t)}{\partial x} \tag{2.147}$$

Assuming that the instability sets with respect to long waves as in the case where the flow develops in open atmosphere (Liu et al., 1993 ; Smith, 1990 ; Kelly & Goussis, 1989), we investigate the linear regime where the waves are sinusoidal, where the stream function, the perturbation on the free surface and the pressure field can be expanded in normal modes repectively with the form :

$$\hat{\psi} = \psi(y)e^{i\alpha(x-ct)} \quad ; \quad \hat{\eta} = \eta(y)e^{i\alpha(x-ct)} \quad ; \quad \hat{p} = p(y)e^{i\alpha(x-ct)} \tag{2.148}$$

We consider a temporal analysis where the wave number α is real and is viewed as a small parameter, while the wave speed c is complex with the form $c = c_r + ic_i$ and i is the imaginary unit defined by $i^2 = -1$.

Substituting the disturbance hydrodynamic field described by Equs.(2.147)-(2.148) in the equations of motion (Equs.(2.143)-(2.144)), we get after a straightforward handling:

$$\psi'''' - 2\alpha^2\psi'' + \alpha^4\psi - i\alpha\,\mathrm{Re}\left[(U-c)\left(\psi'' - \alpha^2\psi\right) - U''\psi\right] \tag{2.149}$$

Equ.(2.149) known as the Orr-Sommerfeld equation (Orr, 1907; Sommerfeld, 1908) governs the stability of a Newtonian fluid over a sloping plane. The effect of the ambient liquid, water in this case, is described by the boundary conditions.

2.5.5.2 Boundary conditions

The above Orr-Sommerfeld equation is a fourth-order ordinary differential equation for the stream function is associated to four boundary conditions summarized in Table 2.1:

	No slip condition	Kinematic condition	Dynamic condition
Liquid 2/Solid plane interface	Impermeability of solid wall. Liquid 2 takes the same velocity as solid wall		
Liquid 1/Liquid 2 interface		The normal velocity of Liquid 2 at the interface must be equal to the normal velocity of the interface	-The shear stress is continuous at the interface -The normal stress is subjected to a jump due to the interfacial tension

Table 2.1: Summary of the boundary conditions.

i/ The no slip condition indicates the impermeability of the solid wall. So, along the contact line, the liquid takes the same velocity as the solid wall

$u = 0$ and $v = 0$ at $y = 0$ (2.150)

Using Equs. (3.147), we get in terms of stream function:

$\psi' = 0$ and $\psi = 0$ at $y = 0$

(2.151)

ii/ The kinematic condition indicates the impermeability of the interface described by its tangential vector $\vec{t}$ and normal vector $\vec{n}$. Therefore, the normal velocity of the fluid $\vec{U}_r \cdot \vec{n}$ at the interface must be equal to the normal velocity of the interface, defined as $\eta \Big/ \sqrt{1+\partial_x\left(\eta^2\right)}$.

So, we must have

$U_2(-\partial_x \eta) + V_2 = \partial_t \eta$ at $y = \eta$ (2.152)

Therefore, after a straightforward algebraic handling, the kinematic condition writes

$\psi(0) - (c-1)\eta = 0$ (2.153)

iii/ The dynamic condition indicates that the shear stress is continuous at the interface and that the normal stress is subjected to a jump due to the interfacial tension. The stress vector in the fluid being $\vec{\sigma} = \underline{\sigma} \cdot \vec{n}$ and the action of the surrounding air being restricted to a purely normal stress $-P_0 \cdot \vec{n}$, the dynamic condition gives the two following equations

$\vec{t} \cdot \vec{\sigma} = 0$ at $y = \eta$ (2.154)

$\vec{n} \cdot \vec{\sigma} - \vec{n} \cdot (-P_0 \vec{n}) = \frac{\gamma}{R}$ at $y = \eta$ (2.155)

After an algebraic handling, these two equations write respectively

$\psi''(0) + \alpha^2 \psi(0) + \eta D^2(0) = 0$ (2.156)

$$-\psi'''(0)+\left(3\alpha^2-i\alpha\,\mathrm{Re}(c-1)\right)\psi'(0)+i\alpha\,\mathrm{Re}\left(\frac{1}{Fr}+\frac{\alpha^2}{We}\right)\eta=0 \qquad (2.157)$$

where a fifth characteristic non dimensional quantity We^* and which can be turned as a characteristic Weber number, defined as

$$We^*=\frac{\rho_0 U_0 L_0}{\gamma_0} \qquad (2.158)$$

has been introduced, while the following relation exists between the Reynolds number and the Froude number

$$Fr^*=\frac{Re^*\tan\beta}{2} \qquad (2.159)$$

In the next sections, Orr-Sommerfeld equation given by Equ. (2.149) with the associated boundary conditions governed by Equs. (2.151); (2.153) ; (2.156) ; (2.157) can be solved analytically, using a perturbation method. In that analysis, the velocity field of the basic flow in non dimensional form was obtained in Equ. (2.158) and it is assumed following Charru (2007) that $\frac{\alpha^2}{We}=O(1)$. Furthermore, the celerity and the stream function can be investigated in the form of power series of that small parameter, say: $c=c_0+\alpha c_1$ and $\psi(y)=\psi_0(y)+\alpha\psi_1(y)$ respectively. The index gives the order of the solution.

In fact, Nsom et al. (2019) proposed a generalized model for shear thinning fluid over an inclined plane surrounded by the atmosphere that reduces to the previous model if power-law index equals unity $(n=1)$, i.e. for Newtonian fluid. So, a similar solution can be derived, provided that in the solution built by Nsom et al. (2019), we put $(n=1)$. Notably, the following results can be derived, where the subscript on the non dimensional parameters Re, Fr, We will be dropped, for making the notations simpler.

2.5.5.3 Solution

i. General solution

The problem at order zero is governed by Orr Sommerfeld equation (Equ. (2.149)) associated with boundary conditions (Equs. (2.151); (2.153); (2.156); (2.157)) in which we put $\alpha=0$. Its solution writes for the stream function say $\psi^{(0)}$

$$\psi^{(0)}(y)=\eta(y+1)^2 \qquad (2.160)$$

and for the celerity say $c^{(0)}$

$$c^{(0)}=2 \qquad (2.161)$$

Equ. (2.161) indicates that the perturbation celerity c_0 has a real value; the perturbation growth rate (imaginary part of celerity) is null. There is no instability with respect to the long wave perturbations considered, at zeroth order. Waves propagate without dispersion, at the same dimensional speed $2U_0$ for any wavenumber. Moreover, the ratio $\psi^{(0)}/\eta$ being real, the interface and the stream function are in phase, while u and v the components of the perturbation velocities are respectively in phase and in quadrature of phase. Again, this result is similar but not identical to the one obtained by Nsom et al. (2019) and Charru (2007). Indeed, the solution description is the same but the expression of the interface velocity U_0 is not the same.

At first order, the problem is governed by Orr Sommerfeld equation (Equ. (2.149)) associated with boundary conditions (Equs. (2.151); (2.153); (2.156); (2.157)) in which we put $\alpha = 1$. Its solution writes for the stream function say $\psi^{(1)}$

$$D^4\psi^{(1)}(y) = i\,\mathrm{Re}\left(\left(U_0 - c^{(0)}\right)D^2 - D^2U_0\right)\psi^{(0)} \tag{2.162}$$

Whose solution provides celerity at first order in the form

$$c^{(1)} = i\,\mathrm{Re}\,\frac{8}{15}\left(1 - \frac{5}{8}\left(\frac{1}{Fr} + \frac{\alpha^2}{We}\right)\right) \tag{2.163}$$

ii. Parametric study

Notice that the celerity correction $c_{(1)}$ is a pure imaginary so it does not bring a contribution to the wave celerity. It only affects its growth rate which at the order one in consideration is therefore

$$\sigma = \alpha\,\mathrm{Im}(c) = \alpha^2 c^{(1)} + O\left(\alpha^4\right) \tag{2.164}$$

The marginal stability corresponds to $c_1 = 0$. As Reynolds number and Froude number are related by Equ. (2.159), the latter secular equation involves two parameters say, Reynolds number Re and reduced wavenumber α^2/We . For assigned value of any of these parameters, Equ. (2.163) is solved by a shooting method. A trial value is given to one of them and the value of the other parameter is sought in order to satisfy Equ. (2.163). That parametric study is presented in the present subsection.

Equ. (2.163) gives the solution to Orr-Sommerfeld equation at first order, stated in previous subsection. It provides a relation between the wave celerity, the wave number and the Reynolds or Froude number for given flow configuration. In order to point out the effect of the different forces acting on the flow, the numerical results are presented in the form of a parametric study by a shooting method. For given slope, the marginal stability curve is defined as the states separating the stable flows from the unstable ones in the (wavelength, Reynolds number) plane. For given slope, it is found that the solution to Equ. (2.163) is not sensitive to the wavenumber α but to a reduced wavenumber given by ratio α^2/We. The computations are brought out for gentle slopes, such that $1° \leq \beta \leq 6°$ (Allouche, 2015 ; Nsom et al., 2018)

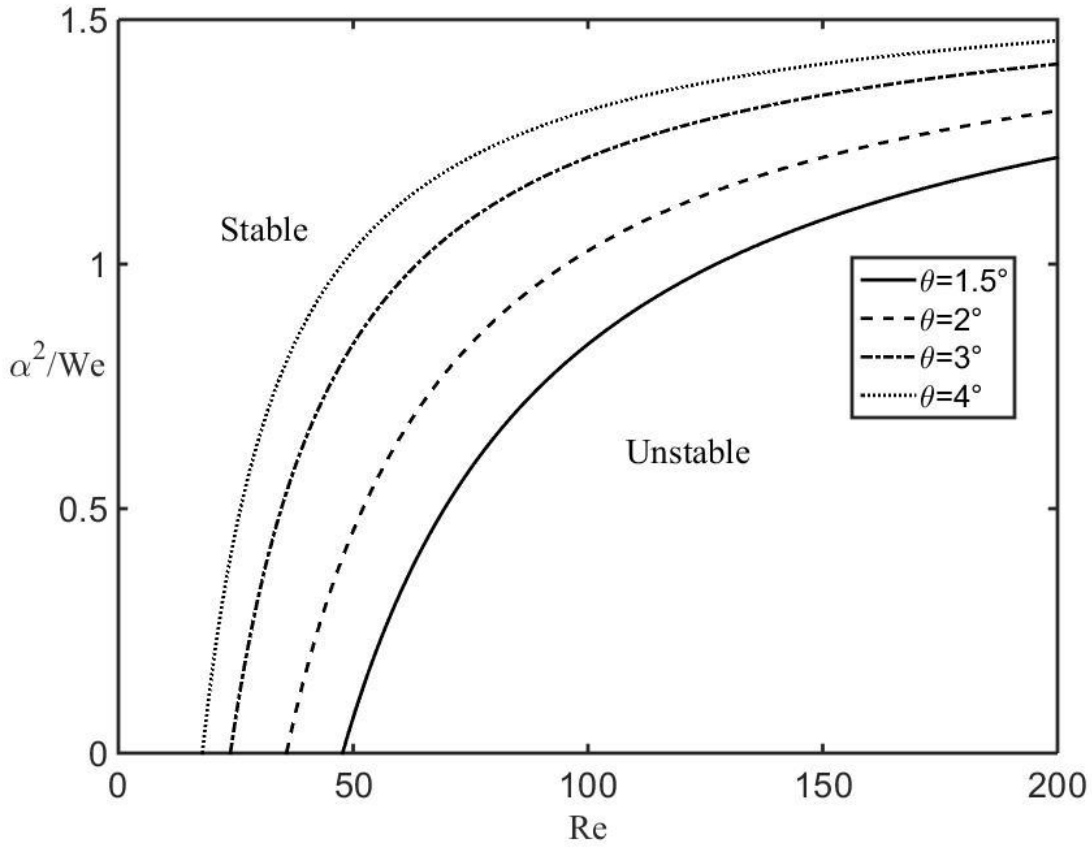

Figure 2.20: The marginal stability curve separating the stable states from the unstable ones for assigned flow configurations

Effect of inertia and pressure on flow stability

For given slope, the marginal stability curve is obtained as follows: a value of reduced wavelength is fixed and growing Reynolds numbers are used for computing Equ. (2.163). The values obtained for celerity c_1 are negative (defining stable flow) and then positive (defining unstable flow). Stable and unstable flows are separated by the marginal state where $c_1 = 0$ and the corresponding value of the Reynolds number defines the critical Reynolds number noted Re_c. Fig.2.18 shows that when the slope increases, the critical Reynolds number decreases for given reduced wavelength. Fig.2.18 shows that inertia acts along the x – axis while pressure (hydrostatic) acts along the y – axis. Therefore, inertia has a destabilizing effect while pressure has a stabilizing effect.

iii. Discussion and Conclusions

The stability of a thin film propagating beneath a large quantity of ambient static non miscible lighter liquid and over a sloping plane was considered theoretically. Such configuration that has never been considered earlier can model the spill of a heavy hydrocarbon into the ocean by a tanker, following a voluntary or accidental degassing or an act of war. Equations of conservation of the mass and the momentum were appropriately made non dimensional and a similar solution was proposed in this paper. In this way, an analytical expression of the hydrodynamic field, say velocity field and pressure field is provided. Then, the equation governing the spatiotemporal evolution of the water-oil interface was built and solved by a perturbation method. Notably, three flow regimes

were identified, say the inertial the viscous and the asymptotic regime in the height spatiotemporal evolution, for assigned aspect ratio λ. Also, the time evolution of the wave front position along the inclined plane was built.

Indeed, it was found that an appropriate non dimensional form of the velocity field shows that it is similar to the case where the surrounding fluid is the atmosphere with a different average velocity. Consequently, the stability analysis of both configurations and the results of both problems were similar. Notably, the solution to the secular equation showed that at zeroth order, there is no instability with respect to the long wave perturbations considered. Waves propagate without dispersion, at the same dimensional speed for any wavenumber. Moreover, the interface and the stream function are in phase, while the components of the perturbation velocities are respectively in phase and in quadrature of phase.

At first order, the secular equation was solved numerically by a shooting method. The effect of the different forces acting on the flow has been pointed out. It was particularly shown that pressure and surface tension have a stabilizing effect, while inertia has a destabilizing effect. Moreover, the relative variation of critical Reynolds number increases with increasing reduced wavenumber for all values of slope tested.

CHAPTER III

NUMERICAL SIMULATIONS

3 Chapter III Numerical Simulations

3.1 Problem statement

In this chapter, numerical simulations were carried out by using OpenFoam software. Interfoam is a specific solver of OpenFoam that used to release the gravity current in the lock-exchange configuration. The lockexchange is a flow of two fluids separated initialy by a wall that moved up to generate a gravity current. In this case, the gravity current flow is created by the difference of density where the heaver liquid moved in the bottom and the lighter liquid moved upper the heavier liquid. The difference of densities between two liquids can be balanced by the inertia, viscous and interfacial tension forces.
In our study, the two liquids are immiscibles and have differents densities, the same viscosities and an interfacial tension. To compare theses forces, we have used the follwong intial control parameters:

- Re_0: intial Reynolds number which is the ratio of the inertia to the viscous forces, and it varied from 25 to 7000 by variaying the viscosity of the liquids.
- We_0: initial Weber number which is the ratio of the inertia to the capillary forces and it varied from 0 to 2500 from by variying the interfacial tension.

To validate our numerical simulations, the temporal evolution of the front positions is compared to that obtained by Huppet et al (Huppert 1982). The validation of the numerical simulations will be completed by the effect of the mesh numbers on the apparition of the interface instabilities between the two liquids.

In our numerical simulations, we will show that the interface beween the two liquids can be smoth or can have undulations (Fig. 3.1) as function as the initial Re_0 and We_0. We have distinguished two interface instabilities: The first one occurs close the bottom (Fig 3.1. a) and the second one is in the stratified vertical direction (Fig 3.1.b).

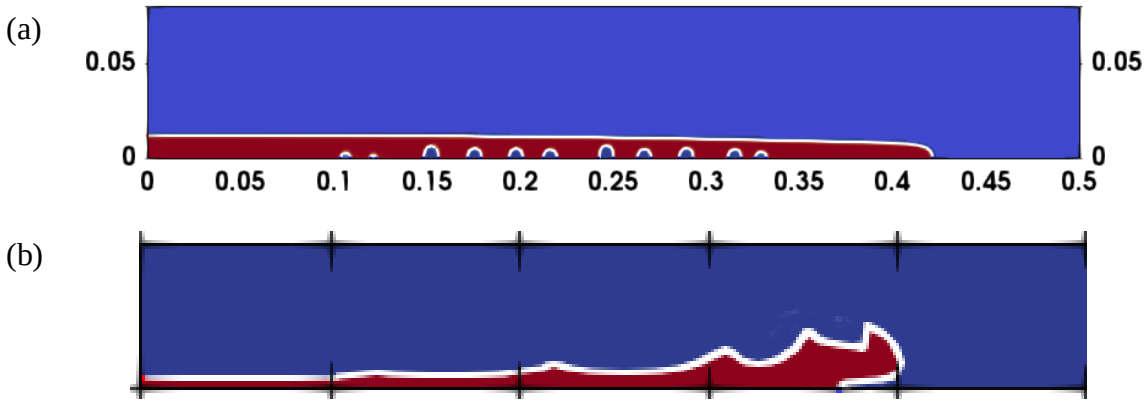

Figure 3.1. Gravity current with an interface intability: (a) close to the bottom for Re_0=25; We_0=250; (b) in the stratified vertical direction for Re_0=2500; We_0=250.

Theses two types of instabilities will be analysed to determine the mechanism of their creations. The velocity and density profiles and computed close to the interface instability in order to give the dominant force responsible to the destabilisation of the interface.

3.2 Lockexchange configuration

Two-dimensional geometry configuration on horizontal plane was chosen as a test case. In this domain, the length of the case is L=0.8 m and its height is h=0.08 m. The heavier fluid locates initially in the left side (red) while the lower fluid is in the right side (blue) of the geometry. The two fluids are separated by a wall which can be moved to give a gravity current motion. The dimensions of the heavier fluid are x_0 =0.08 m and h=0.08 m. The shape contains 6 vertices as shown in the figure 3.2 :

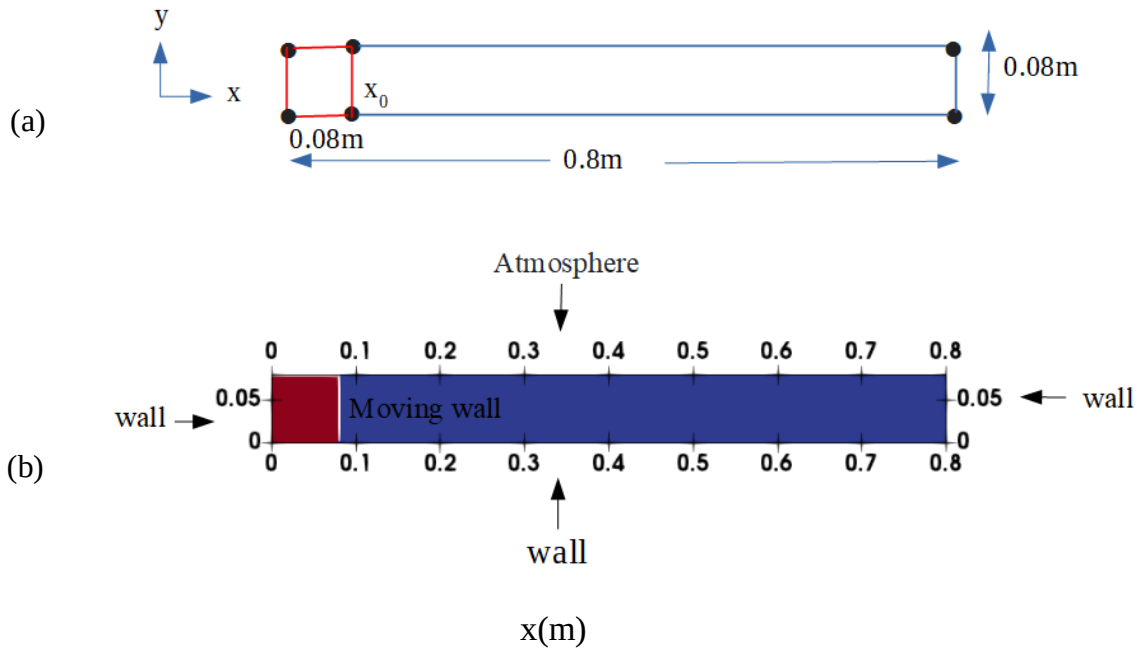

Figure 3.2 .(a) A sketch of the geometrical domain of gravity current (b)The numerical simulation of contour of fractional volumic c of the gravity current at t = 0 s . The two-layer immiscible fluids with same viscous but different densities ρ1 and ρ2 and with a grid resolution 1000×100.

The 2D simulations are carried out on a grid resolution $(\boldsymbol{n_x, n_y}) = (\mathbf{1000, 100})$, and the stepsizes are$\Delta \boldsymbol{x} = \boldsymbol{x/n_x} = \mathbf{80}\ \boldsymbol{cm/1000} = \mathbf{0.08}\ \boldsymbol{cm}$, and$\Delta \boldsymbol{y} = \boldsymbol{y/n_y} = \mathbf{8}\ \boldsymbol{cm/100} = \mathbf{0.08}\ \boldsymbol{cm}$. Despite its simple geometry it creates interesting and complex phenomena.

In the OpenFOAM package, the walls and atmosphere (The atmosphere is a standard patch, i.e. has no special attributes, merely an entity on which boundary conditions can be specified) are associated with the wall condition. To complete the problem, it is essential to define the border and the initial Conditions. The boundary conditions are defined on all the boundary faces of the domain and can be divided mainly into two types: Dirichlet and Neumann conditions: Dirichlet-prescribes are the value of the dependent variable on the border and is therefore called "fixed value" in

OpenFOAM. Also, Neumann -prescribes the gradient of the normal variable at the border and is therefore called "fixedgradient" in OpenFOAM.

3.3 Mathematical Model

In two-fluids system, the Navier Stokes equations for two incompressible, isothermal immiscible fluids include:

1- Continuity equations: $$\frac{\partial u_j}{\partial x_j} = 0 \quad (3.1)$$

2- Momentum Equation $$\frac{\partial \rho u_i}{\partial t} + \frac{\partial \rho u_j u_i}{\partial x_j} = -\frac{\partial P}{\partial x_i} + \frac{\partial\left(\tau_{ij}+\tau_{t_{ij}}\right)}{\partial x_j} + \rho g_i + f_{\sigma i} \quad (3.2)$$

where

u_i Represent the velocity

g_i The gravitational acceleration,

P The pressure

$\tau_{ij}$and $\tau_{t_{ij}}$ are the viscose and turbulent stresses.$f_{\sigma i}$ is the surface tension.

The density ρ is defined as: $\rho = C\rho_1 + (1 - C)\rho_2$

C is 1 inside fluid 1 with the densityρ1 and 0 inside fluid 2 with the densityρ2. At the interphase between the two fluids α varies between 0 and 1. The surface tension $f_{\sigma i}$ is calculated as: $f_{\sigma i} = \sigma k \frac{\partial C}{\partial x_i}$

σ is the surface tension constant, K the curvature. The curvature can be approximated as: $k = -\frac{\partial n_i}{\partial x_i} = -\frac{\partial}{\partial x_i}\left(\frac{\partial C/\partial x_i}{|\partial C/\partial x_i|}\right)$.

3- Equation for the interphase :$$\frac{\partial C}{\partial t} + \frac{\partial (C u_j)}{\partial x_j} = 0 \quad (3.3)$$

In order to know where the interphase between the two fluids is, an additional equation for C has to be solved. The equation can be seen as the conservation of the mixture components along the path of a fluid parcel.

The VOF method that is used in this work is an excellent tool to simulate complex interface motion between the gravity current and ambient fluid, where it's used to the interface tracking for two immiscible fluids. The VOF method has been embedded into commercial codes such as open-source CFD codes like OpenFOAM. In this method the interface is indirectly represented by a numerical field describing the volume fraction of gravity current within each computational cell. The VOF method is applied to several problems of environmental interest, including the dam-break problem, internal waves, and propagation of gravity current.

The volume of fluid (VOF) technique is one of the Finite volumes techniques which is use for tracking the interface between gravity current and the ambient fluid. In this method, continuity and momentum equations will be involved. And to determine the phase properties across the interface, we include the volume fraction equation. The equations, continuity, momentum equations will be

getting teamed by this volume fraction equation. The volume fraction equation is very important in case of two-fluid flow computations.

In this technique, we will solve the equations of mass and momentum conservation. Continuity equation have density ρ, this density is some average density in the field, and this average density will be having some particular value at bulk and some intermediate value between the bulk properties near the interface. So, the density ρ can be defined as function of volume fraction of the first fluid inside a cell, that volume fraction. We capture using the property called C. So C is the volume fraction, that means we are talking about two fluids 1 and 2, 1 is the first fluid and 2 is the second fluid so we will be finding out that we are having C_1 =1 in the bulk of the first fluid and C_2=1 at the bulk of second fluid and the corresponding values of C_2 and C_1 in the first fluid and second fluid will be becoming 0 and when the cell contains an interface between the tracked and non-tracked volumes, 0 < C < 1.We can defined the density based on the volume fraction of any of these two fluids. If C is nothing but the volume fraction for the first fluid so this ρC can be written as:$\boldsymbol{\rho = C\rho_1 + (1 - C)\rho_2}$,that is means whenever we are in the bulk of the first fluid, where value of C is 1 we will be getting that ρ gets the value of ρ1 and whenever we are in the bulk of second fluid, then we will be getting that this value of ρ, will be talking ρ2 because C will be at that time becoming 0. Similarly, viscosity can be also defined as: $\boldsymbol{\mu = C\mu_1 + (1 - C)\mu_2}$. Depending on C, we can find out the ρ and μ and we can write down a continuity equation which has the form (3.1). From the Momentum Equation(3.2), an added portion will be over here for the surface tension portion $\boldsymbol{f_{\sigma i}}$ because as we are dealing with two phase so we will be having surface tension involved in that, and surface tension will be involved in the interface, that is means $\boldsymbol{f_{\sigma i}}$ is the function which controls the value of surface tension.Since the interface location is changing, this value of α will be changing across the time then we need to get some equation of C which will be adverting from the first place to another place along with the time, and we have (3.3) which is the governing equation for conservation of volume fraction.

3.3.1 Inital conditions

Future values of the numerical simulation can be found by iterating forward one time period per iteration, so we shall need to initial conditions are needed in order to trace the system's variables forward through time. The initial and boundary conditions can be presented as follows:

1- **The velocity**

At the initial time t = 0, no-slip velocity initial conditions u=0, v=0 were used on walls, therefore, the initial velocity of walls with no-slip velocity y = 0, that is means the velocity in all directions is equal to zero.

2- The pressure

The initial pressure at walls is fixed flux pressure, that is means the pressure in all directions is equal to zero, also the initial depth of the gravity current is 0.008 m and the initial gravity current length is 0.008 m.

3.3.2 Boundary conditions

Boundary conditions are constraints necessary for the solution of a gravity currents problem in a specific domain. The boundary conditions can be presented as follows:

1- Leftwall: The region of interest of gravity current is (the lenght x = 0 m, $0 \leq y \leq 0.08$ m).
2- Rightwall: The region of interest of gravity current is (the lenght x = 0.8 m, $0 \leq y \leq 0.08$ m).
The velocity is set to zero at the wall boundary. The phase fraction can have any value between 0 and 1. The boundary conditions are summarized in the following table :

Varibles	Wall	Atmospher
U	no-Slip	Type:Pressureleft/rightwallVelocity Value:uniform(0,0,0)
p+ρgh	Grad(p)=0	Total pressure = 0
c	ZeroGradient	ZeroGradient

Table 3.1 .Boundary conditions

3.3.3 Control parameters values

The control parameters are initial Reynolds and initial Weber numbers which defined as $\boldsymbol{Re_0 = \frac{U_b h}{\nu}}$, $\boldsymbol{We_0 = \frac{\rho {U_b}^2 h}{\sigma}}$ respectively, where $\boldsymbol{U_b = \sqrt{\frac{gh\Delta\rho}{\rho}}}$ is the intial velocity, *v* is the kinematic viscosity is the same for the liquids, $\boldsymbol{\Delta\rho}$ is the density difference between the two fluid, $\boldsymbol{\sigma}$ is the surface tension and **h** is the height of gravity current. In this work, we have : $\boldsymbol{\Delta\rho = 40\ Kg/m^3}$, $\boldsymbol{U_b = 0.17\ m/s}$ $\boldsymbol{\sigma = \{0.01, 0.0001\}}$, $\boldsymbol{We_0}$=[0; 2500]. In the range of Re_0 = [25; 7000], the kinematic viscosity *v* corresponding to each Reynolds number is summarized in the table 3. 2.

Test number	Kinematic viscosity	Initial Reynolds numbers	Test number	Kinematic viscosity	Initial Reynold numbers
1	5.56×10^{-4}	25	10	3.98×10^{-6}	3500
2	2.78×10^{-4}	50	11	3.48×10^{-6}	4000
3	1.39×10^{-4}	100	12	3.09×10^{-6}	4500
4	2.78×10^{-5}	500	13	2.78×10^{-6}	5000
5	1.39×10^{-5}	1000	14	2.52×10^{-6}	5500
6	9.27×10^{-6}	1500	15	2.31×10^{-6}	6000
7	6.95×10^{-6}	2000	16	2.13×10^{-6}	6500
8	5.56×10^{-6}	2500	17	1.99×10^{-6}	7000
9	4.63×10^{-6}	3000			

Table 3.2. The kinematic viscosity by corresponds to Initial Reynold numbers

3.4 Results and discussion

3.4.1 The front position points of a gravity current

The gravity current flow was computed with initial Reynolds number from 25 to 7000 and with a fixed intial Weber number at We0=250.

The figure 3.3 presents the evolution of horizontal velocity Ux and the position of the interface represented by the countour with white coulour for Re0 =1000 and We0=250.
The heavier gravity current propagates over the rigid bottom surrounding by the lighter liquid.
This heavier gravity current consists of three main parts, namely: the head, the body and the tail.
In this subsection, we focus on the head of the gravity current. The advanced position of the head gives the front position points of the heavier gravity current as a function of time $\boldsymbol{X_f(t)}$ (Figure3.4a) this permits to calculate the front velocity $V_f(t) = \boldsymbol{dX_f/dt}$ (Figure3.4b).

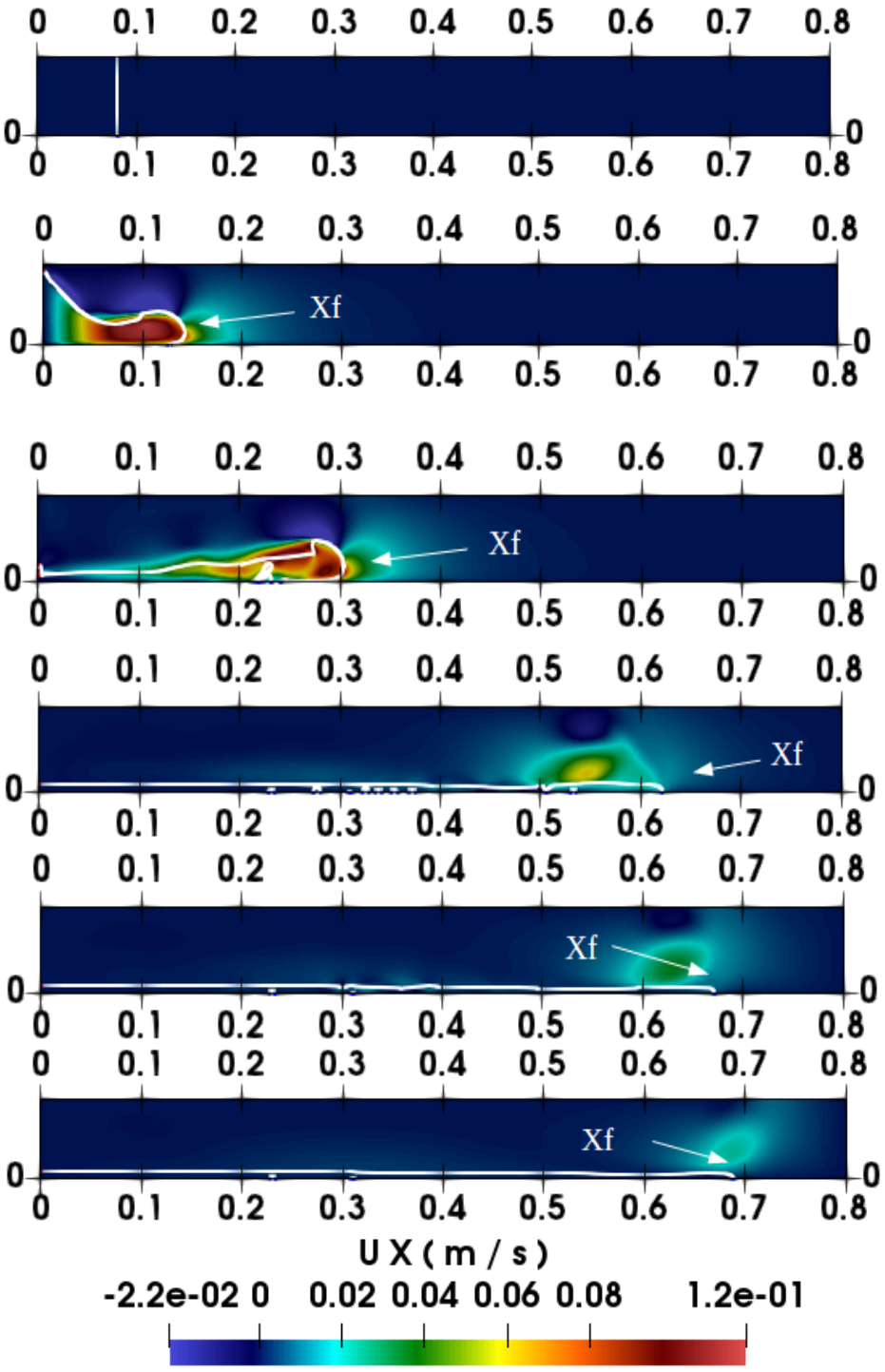

Figure3.3 . Horizontal velocity and interface position between two liquids for Re_0 =1000 and We_0=250, at t = 0s; 1s; 3s; 10s; 15s; 20s and with a grid resolution 1000×100.

(a)

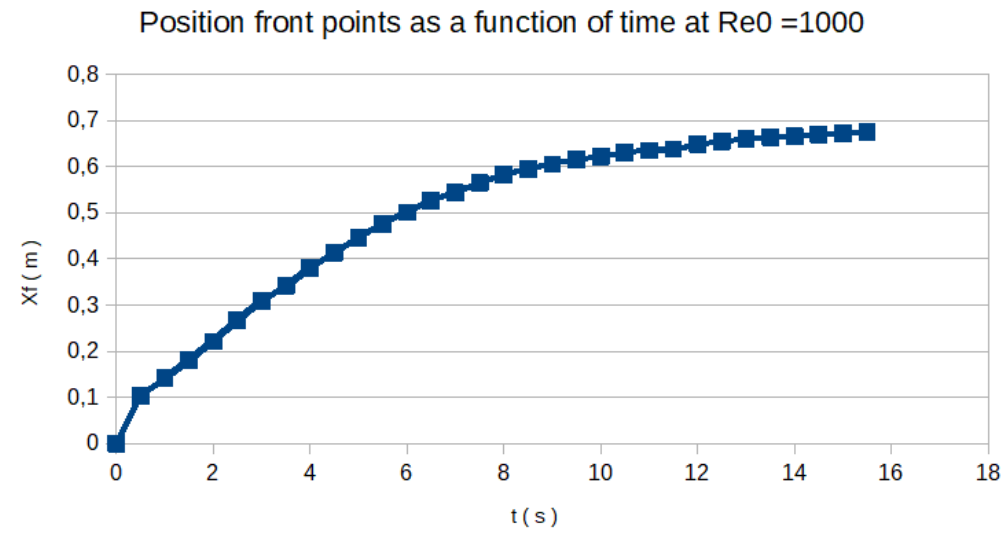

(b)

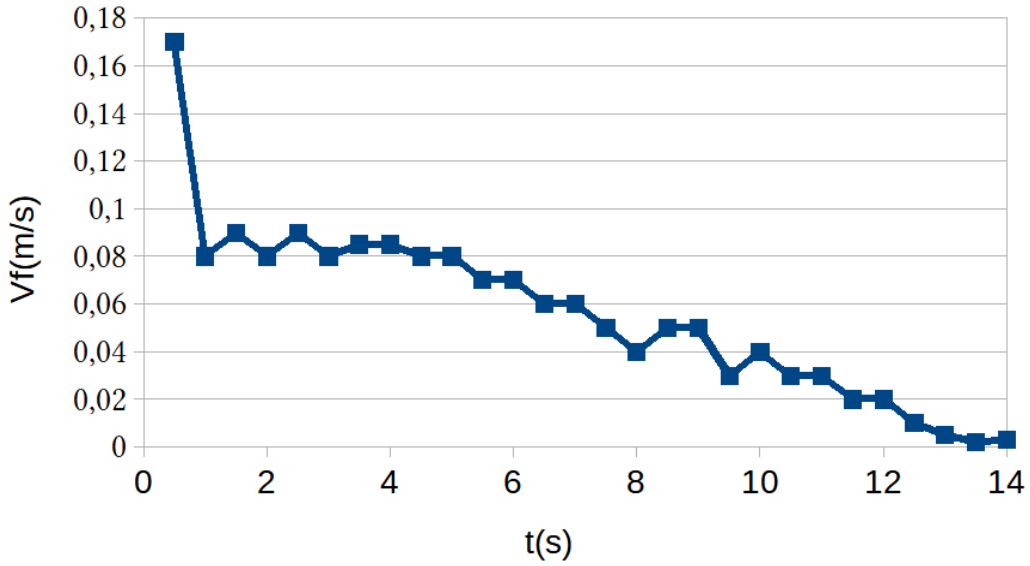

Figure 3.4 . (a) Diagram for the evolution of front position as a function of time for gravity current with initial Reynolds numbers =1000 and initial Weber number = 250. (b) Diagram for the evolution of the front velocity as a function of time for gravity current with initial Reynolds numbers =1000 and initial Weber number = 250 .

The velocity of front position points is equal to the nose velocity.

Figure 3.3 shows the behavior of the gravity current head, where the front (Xf) increase with the time following a power function (Xf = a tb). The exponent b of the power function of the front position wil be determined using the Huppert theory in the next subsection for the initial Reynolds numbers between 25 to 7000 and for We0=250.

The position front points (Xf) with the time were computed for the initial Reynolds numbers in the range 25-7000 and for We0=250 in the figure 3.5 where the horizontal axis represents time, and the vertical axis represents the front position points. Also the figure showed that when the Reynolds numbers increase, the values of the front position increase with time as shown in the figure 3.5

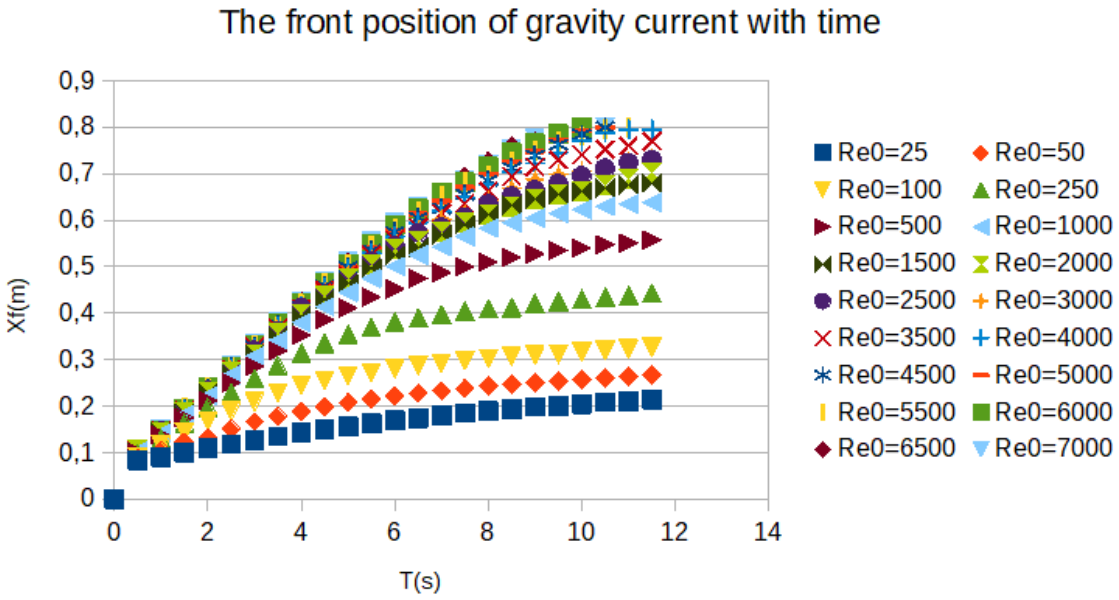

Figure 3.5 . Evolution of front position as a function of the time for initial Reynolds numbers : 25, 50, 100, 250, 500, 1000, 1500,2000, 2500, 3000, 3500, 4000 ,4500,5000, 5500, 6000, 6500, 7000 and initial Weber number We_0= 250.

3.4.2 Validation of numerical simulations

In order to validate our numerical simulations, two complementaries methods were used to answer for this question: the first is based on the Huppert theory, while the second one is based on the apparition of the interface instabilities.

The heoretical study of Huppert (Huppert et al 1982) showed (Huppet et al 1982) that the front position against time is a power law in the viscous regime: $\mathbf{X_f = \zeta\left(\frac{B_0 {A_0}^2}{3\nu}\right)^{1/5} t^{1/5}}$, where $\mathbf{B_0 = \acute{g}_0 A_0}$, $\mathbf{A_0 = L_0 h_0 = {h_0}^2}$.

In the figure 3.6, by dividing X_f by $\left(B_0 A_0^2/3\nu\right)^{1/5}$, , we plot $\boldsymbol{X_f/\left(\frac{B_0 {A_0}^2}{3\nu}\right)^{1/5}}$ versus $\boldsymbol{t^{1/5}}$ in order to compare with the theory of Huppert, We obtained on ζ=2.9. Although the obtained coefficient ζ in our numerical is twice higher than that obtained by Huppert (Huppet et al 1982) in his theory (ζ=1.411) but we have the same exoponet as Huppert.

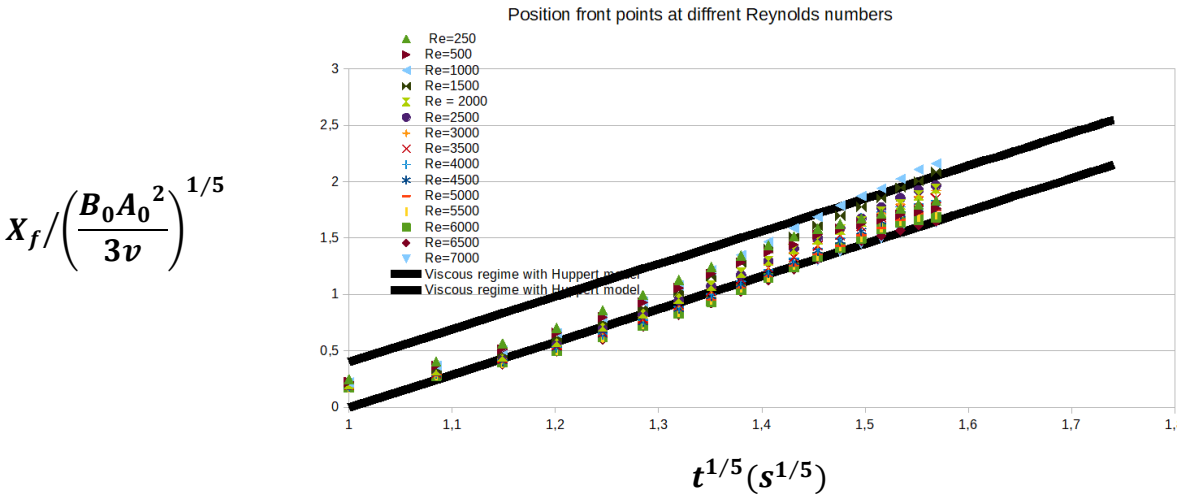

Figure 3.6 .Validation of numerical simulations by the theory of Huppert 1982 which showed that when the local Reynolds number decreases, the flow is visco-gravity (buyoncy-viscous phase), the position of the front is described by the power law:$X_f = \zeta \left(\frac{B_0 {A_0}^2}{3\nu}\right)^{1/5} t^{1/5}$,where $B_0 = \acute{g}_0 A_0$, $A_0 = L_0 h_0 = {h_0}^2$.

To complete the validation of our numerical simulations, the effect of the mesh numbers with the apparition of the interface instabilities was used to give an answer of this question. We have compared both the hydrodynamic and interface shape for differents mesh numbers and we have concluded that the mesh with 1000×100 gave the best detection of the interface instabilities between two immiscible liquids.

In Figure 3.7, we compare the numercal simulations results for the evolution of horizontal velocity with the interface position between two liquids with two meshes: (a) the low mesh is of 250×25 points and (b) the high mesh is of 1000×100. We can observe that the interface instability was detected for the high mesh of 1000×100. With this comparison, we have complemented the validation of our numerical simulations.

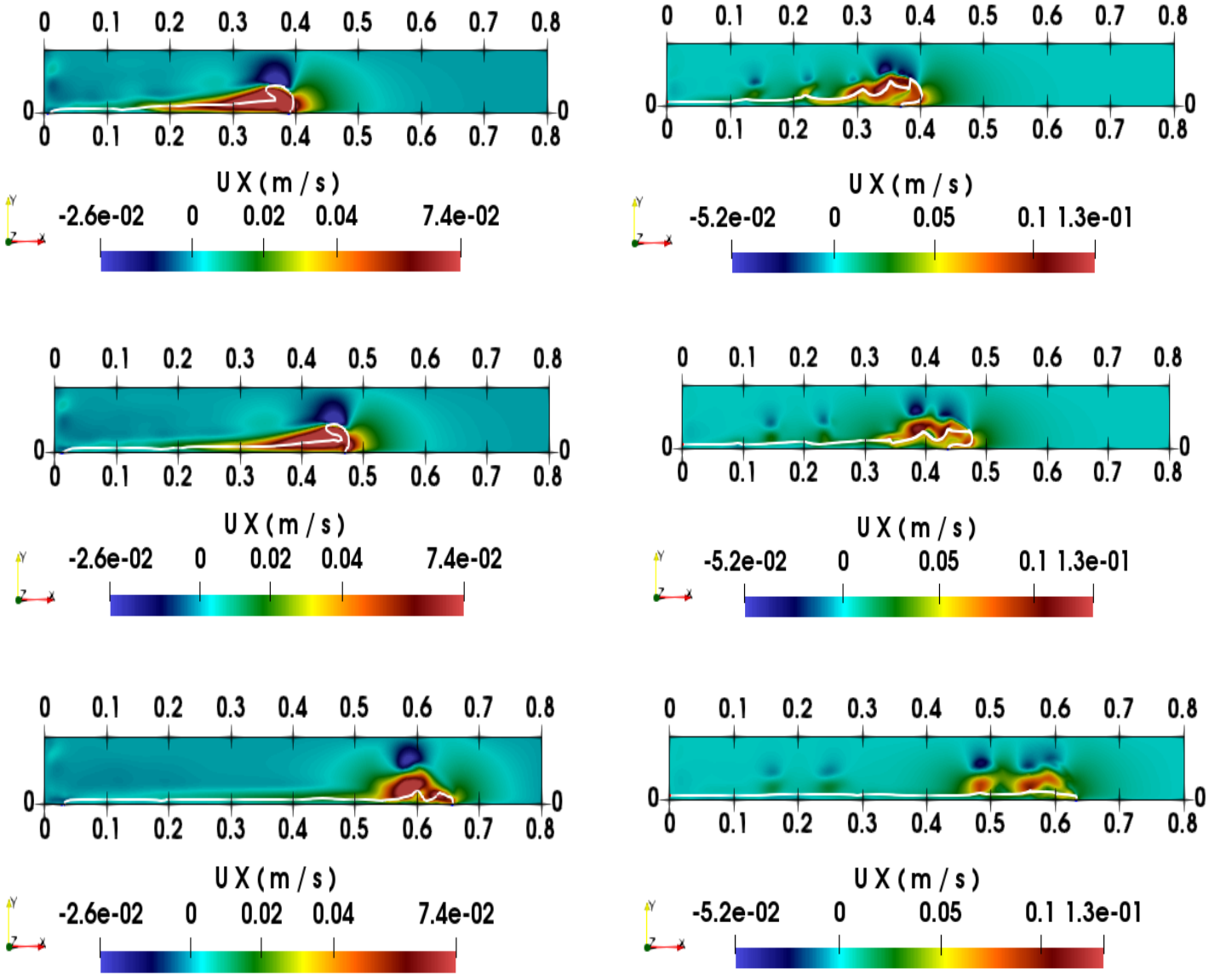

(a) (b)

Figure 3.7. The results of the numerical simulation of the evolution of horizontal and interface position for Re0 = 2500, t = 4s and 5s with a grid resolution: (a) 250×25 and (b) 1000×100.

In Figure 3.9, we compare the simulation results for the evolution of contour of vertical velocity of the gravity current and at time t = 4s, 5s, 8s with two meshes, the first meshe with an accuracy of 250×25 and the second meshe with an accuracy of 250×25. The results o showed that increasing the accuracy of the mesh gives more accurate results as follows:

3.4.3 Interface instability close to the horizontal bottom

In the Figure 3.8, the numerical simulation results showed that the interface close to the bottom is unstable for Re_0=[25; 2000] for We_0=250. We have observed that the head of the heavier liquid has an elevation that permits the intrusion of the lighter liquid between the head and the rigid bottom. In this case, the interface between the heavier and the lighter liquids has an undulation. Thus, this lead to the instability of the lower interface between the heavier and the lighter liquids close to the horizontal surface. In this case, the part of the heavy fluid in contact with the solid surface has a discontinuity where the lighter liquid remains trapped in the form of drops (figure 3.8). This is due to the competitions of the several forces that dominate the flow close to the bottom. The two liquids are immiscibles, viscous and with an interfaciale tension. The calculations of the bulk Reynolds ($\boldsymbol{Re_b} = \frac{\boldsymbol{V_f h}}{\boldsymbol{\nu}}$) and Weber ($\boldsymbol{We_b} = \frac{\boldsymbol{\rho V_f^2 h}}{\boldsymbol{\sigma}}$) numbers of the front permit to compare the dominate force close the bottom and the head with time. In the figure 3.9, the bulk Reynolds and Weber numbers are plotted with time for Re_0=2000 and We_0=250. When Reb<100 and Web<10, the capirally instability of the interface between the heavier and lighter liquis occurs as drops (Figures 3. 8 and 3. 9).

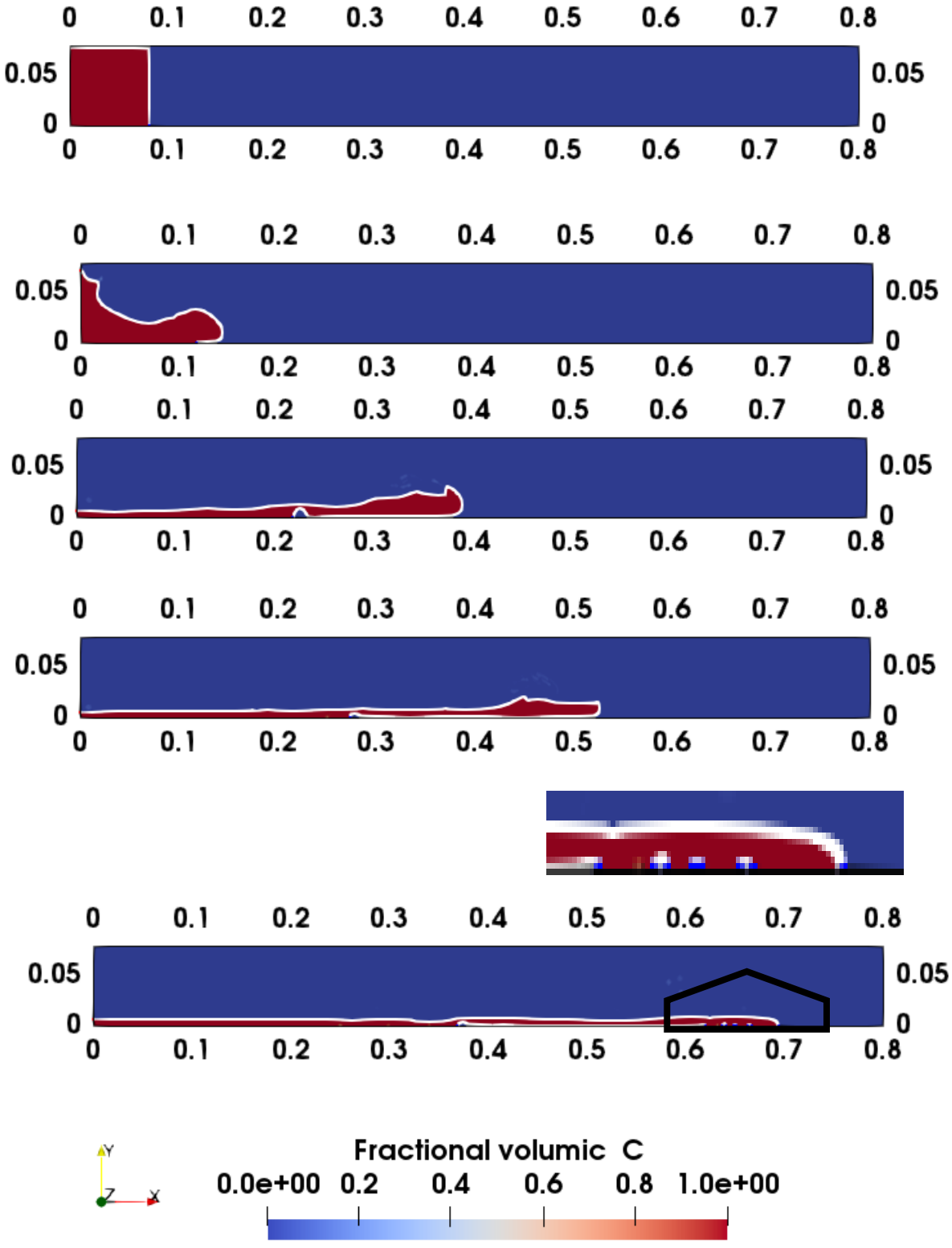

Figure 3.8 Capillay instability of the interface between two liquids close the bottom wall represented by the volumic fraction C for Re_0 = 2000 and We_0=250 and for t = 0, 1s, 3.5s, 5.5s and 10s. The zoom presents the drops (capillary instability).

(a)

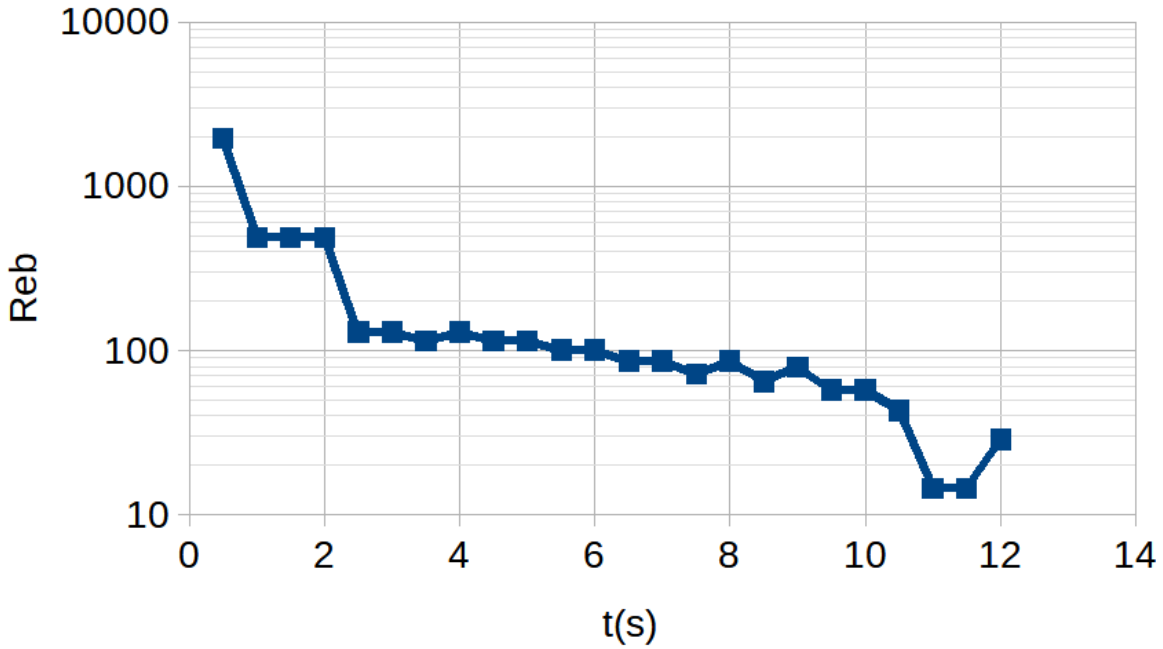

(b)

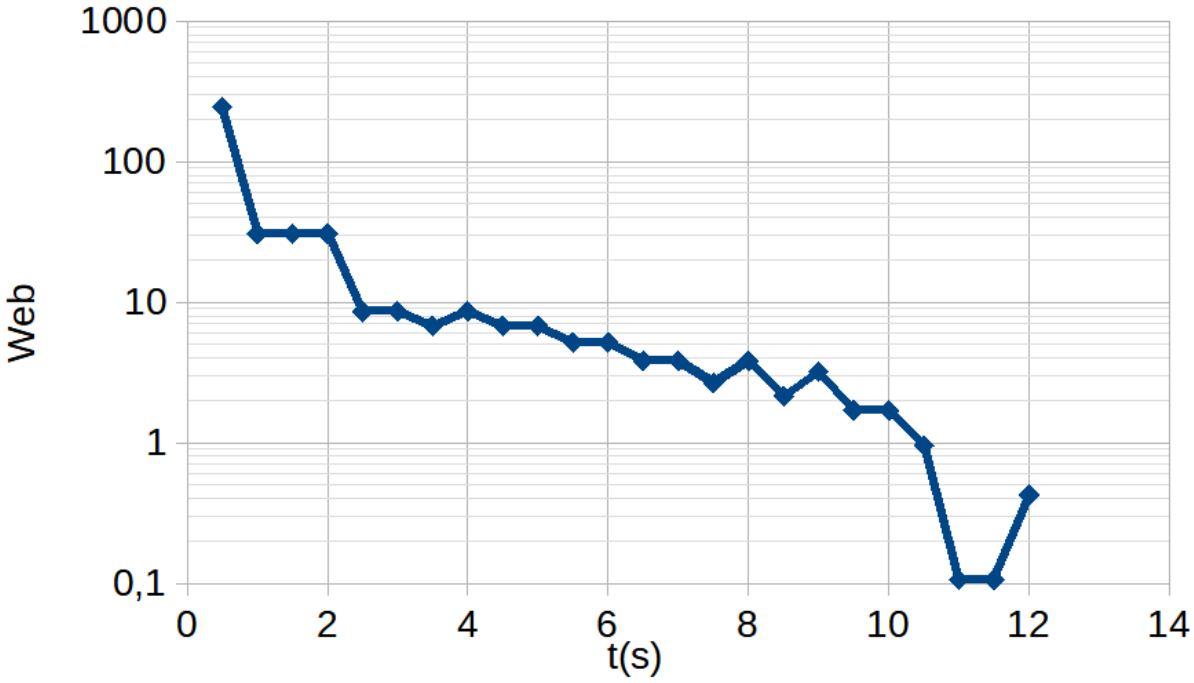

Figures 3. 9. Time evolution of the bulk Reynolds numbers (a) and the bulk Weber number (b) for Re_0=2000 and We_0=250.

3.4.4 Interface instability in vertical stratified density

On the addition of the interface close to the bottom, the two liquids have an interface in the vertical density stratification. Generally, the flow with density stratification has density and velocity thicknesses. In the case of miscible fluids, the characteristic thicknesses of the density δ and velocity δu profiles are of the same order of magnitude (δ ≈ δu), the resulting velocity profile is known to be subjected to an inflexional instability mechanism, which gives rise to the formation of vortical structures or Kelvin-Helmholtz billows travelling at approximately the average velocity between the two streams (Ho & Huerre 1984, Pouliquen 1993). In the case of immiscible liquids, the thickness of the density profile at the interface is much smaller than the thinckness of velocity profiles (δ<<δu), As first demonstrated by Holmboe (1962), this situation is more complex where a density discontinuity is embedded within a linear velocity profile, there may exist an additional pair of unstable travelling waves or Holmboe modes (Pouliquen 1993).

In Figure (3.10), the volumic fraction showed that the interface instability is in the form of cusp-like internal waves; consist of cusps projecting in to the interface between the heavier and the lighter liquids and moving from left to right. With the evolution of the flow with time, differences were observed in this wave's structure. It is clear that the growth rate, absolute phase speed, and wavelength are not equal. This instability occurs at the range of intial Reynolds numbers Re0=[500-7000] for We0=250.

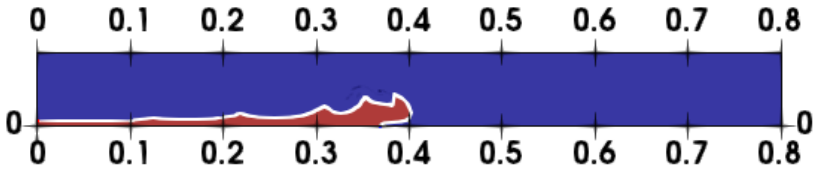

Figure 3.10 Volumic fraction C for the interface instability (Holmboe) in the vertical stratified density (for for Re_0 = 2500, We_0 = 250 at t = 4 s. The red color represents the heavier liquid with ρ_2=1080 kg.m^{-3} and the blue color represents the lighter liquid with ρ_1=1040 kg.m^{-3}, while the white color represents the interface between the two liquids for ρ=1060 kg.m^{-3}.

In this subsection, we will analyse the thichness profile of the horizontal and vertical velocities (Ux; Uy) and the density thickness against the vertical axis points Y close to the intability interface.

Figure 3.11 a-b present the respectively the fields of the component velocity Ux and Uy in the plane (X,Y) at t=2,5s for Re_0 = 2500, We_0 = 250. The white color represents the position of the interface separate the two liquids. The interface of the Figure 3.11 a-b presents three cusps of the

Holomboe instability. The amplitude of the cusps is high close to the head of the gravity current while it is lower close to the tail and it is intermediaite in the body of the gravity current.

First, we present the data analysis of the interface Holomboe instability for that close of the head of the gravity current which is marked by the white vertical narrow in the Figure 3.11 a-b at x=0.2m. In the interface Holomboe instability, the velocity profiles of the horizontal and vertical show a continuity variation while the density presents a discontinuity because of the immiscible liquids. To explore more the velocity variation, we have computed the velocity gradient (shear rate : $\frac{dUx}{dy}$; $\frac{dUy}{dy}$) as function of the Y axis close to the interface instability (Figure 3.11 c). The shear rate presents a maximum ($\frac{dUx}{dy} = \mathbf{19.3}\ \boldsymbol{s^{-1}}$; $\frac{dUy}{dy} = \mathbf{5.7}\boldsymbol{s^{-1}}$) at the head of the cusps interface of Holomboe. The moduls velocity gradient defined as $\sqrt{\left(\frac{dUx}{dy}\right)^2 + \left(\frac{dUy}{dy}\right)^2}$ presents a clear maximum (20 s^{-1}) at the head of the cusps interface of Holomboe (Figure 3.11. e).

(a)

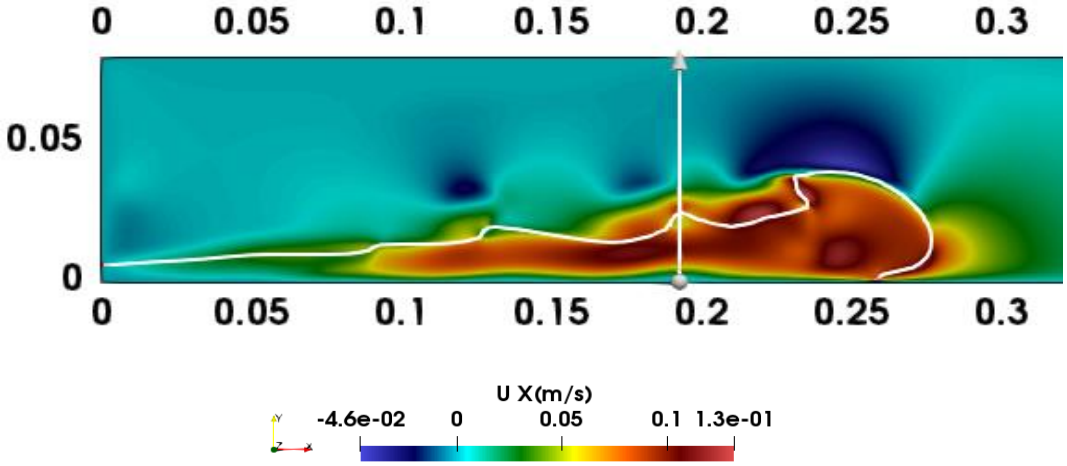
0
0.05
0.1
0.15
0.2
0.25
0.3
0.05
0
U X(m/s)
-4.6e-02
0
0.05
0.1
1.3e-01

(b)

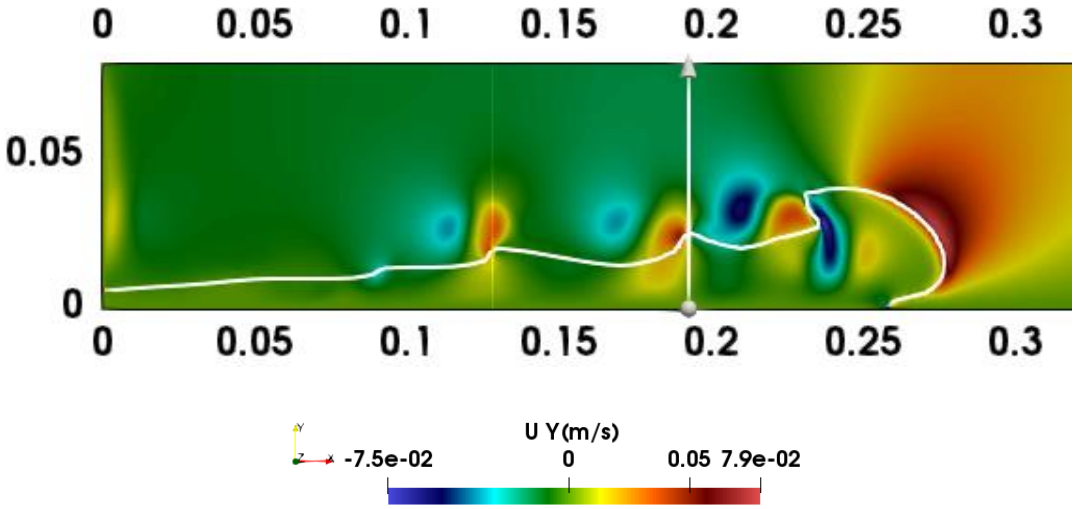
0
0.05
0.1
0.15
0.2
0.25
0.3
0.05
0
U Y(m/s)
-7.5e-02
0
0.05
7.9e-02

(c)

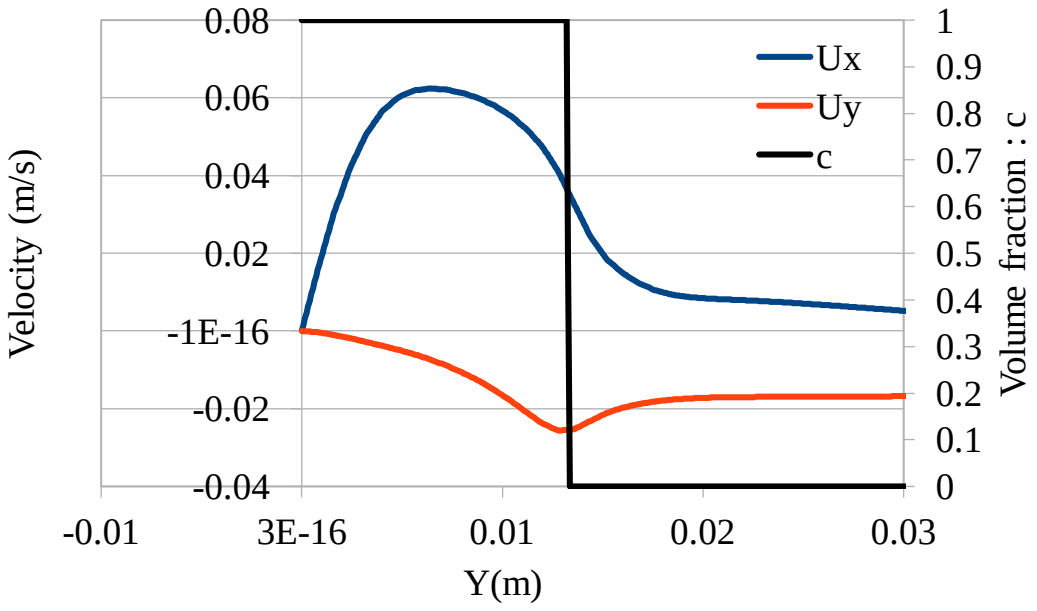
0.08
0.06
0.04
0.02
-1E-16
-0.02
-0.04
-0.01
3E-16
0.01
0.02
0.03
Y(m)
Velocity (m/s)
Volume fraction : c
1
0.9
0.8
0.7
0.6
0.5
0.4
0.3
0.2
0.1
0
Ux
Uy
c

(d)

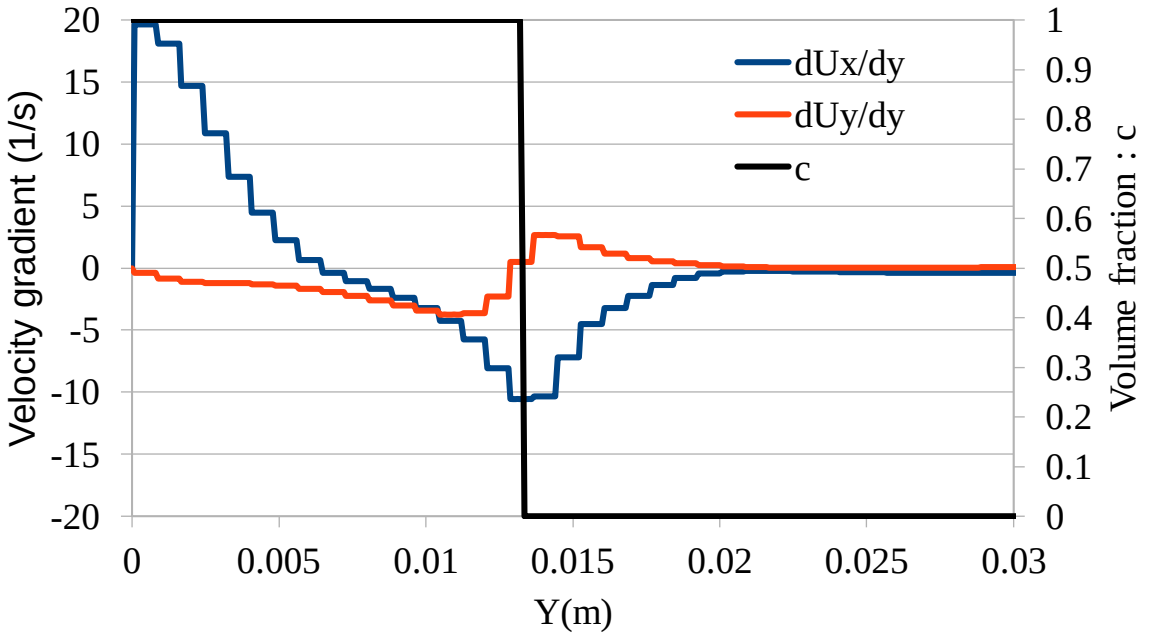

(e)

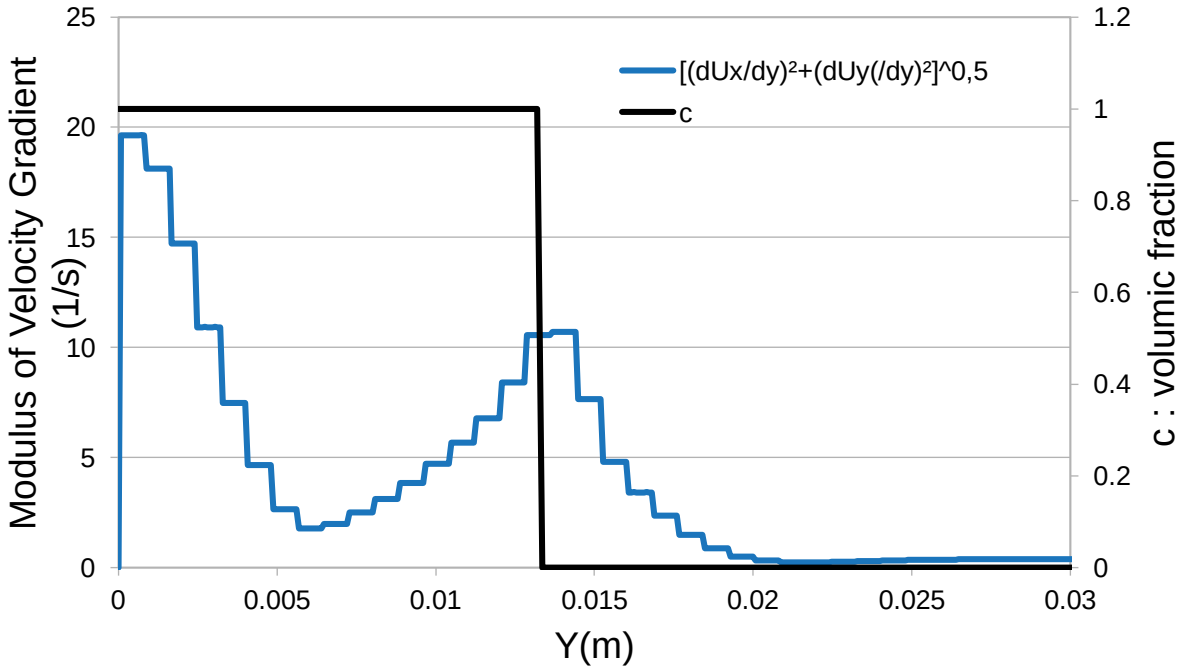

Figure 3.11 : (a)Horizontal velocity Ux(X,Y, t=2.5s), (b) vertical velocity Uy(x,y, t=2.5s), (c) velocity and density profiles in the Holomboe instability, (d) velocity gradient profile, (e) Modulus of velocity gradient in the Holomboe instability for Re_0 = 2500, We_0 = 250 t = 2.5 s.

In our case, the Holomoboe instability of the interface is related to the competition between the stratification of densities of the two liquids and the shear rate close to the interface. To quantify this competition, we use the Richardson number which is defined as the ratio between the buyoncy buoyancy frequency $N^2 = \frac{-g}{\rho_o}.\frac{\partial \rho}{\partial z}$ to the vertical shear rate: $Ri = N^2 / \left[(\frac{\partial \overline{u}}{\partial z})^2 + (\frac{\partial \overline{v}}{\partial z})^2\right]$. In our case the liquids are immiscibles so there is no density gradient $\frac{\partial \rho}{\partial z}$. Pouliquen et al (1993) have used a modified density gradient which is defined as $\frac{\rho_2 - \rho_1}{L}$ where $L = \sqrt{\frac{\sigma}{g(\rho_2 - \rho_1)}}$ is the lenghtscale of the density discontinuity of the two immiscible liquids related to the interfaciale tension σ and the density difference. In this case, we obtain a modified Richardson number (Ri-*loc*) as follows:

$$\mathrm{Ri}_{loc} = \frac{\frac{g(\rho_1 - \rho_2)}{(\rho_1 + \rho_2) \times L}}{\left[(\frac{\partial \overline{u}}{\partial z})^2 + (\frac{\partial \overline{v}}{\partial z})^2\right]}$$

In the Figure 3.12, we show the local Richardson number (Ri-*loc*) in the Holmboe intability in the three cusps: (a) Close to the tail of the gravity current, (b) in the body of the gravity current and (c) in close the head of the gravity current. The common behavior is that the Ri-loc presents a minimum at the three positions. This means that the shear rate can destabilize the stratification of the density and can create the instability at this position of the maximum shear.

(a)

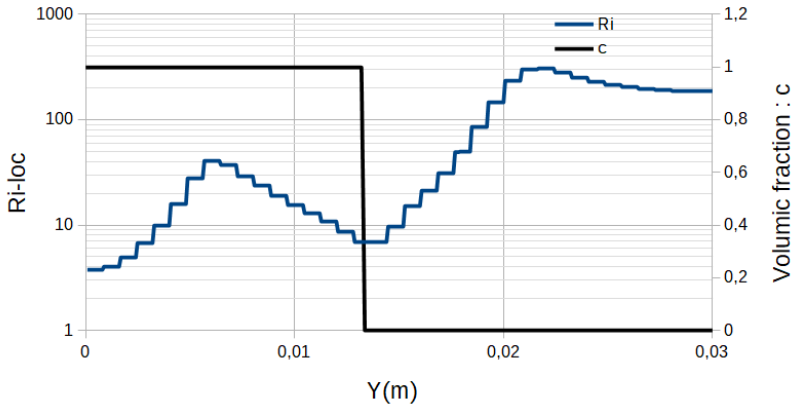

(b)

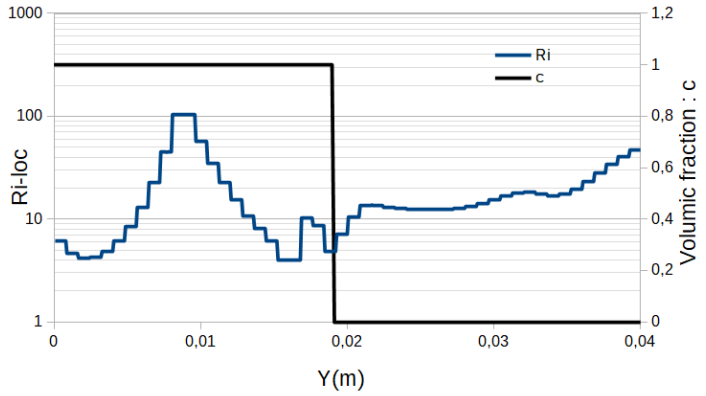

(c)

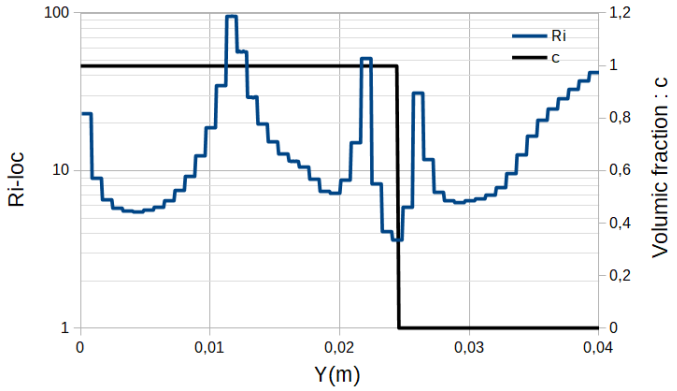

Figure 3.12. Local Richardson number behavior in the Holmboe instability

3.4.5 Relationship between Riloc and amplitude of the interface Holomboe instability

To analyse more the Holmboe instability, the amplitude was computed at three cusps (Figure. 3.13) and compared to Ri_{-loc} (Figure 3.14). For Re0=2500, We0=250, the amplitude (A) of the interface Holmboe interface and Ri-loc are:

- A=0.00643 m, Ri_{-loc}=3.5 for the cusp close to the head of the gravity current,
- A=0.00481 m, Ri_{-loc}=5 for the cusp in the body of the gravity current
- A=0.0015 m, Ri_{-loc}=7 for the cusp close to the tail of the gravity current

We conclude that the amplitude decreases when the Ri_{-loc} increases. This means that the interface is smooth for the large values of (Ri_{-loc}>10) where the density stratification is higher than shear rate. In the opposite case (small values of $Ri_{-loc}\leq 10$), the interface is unstable and presents cusp-like Holomboe instability.

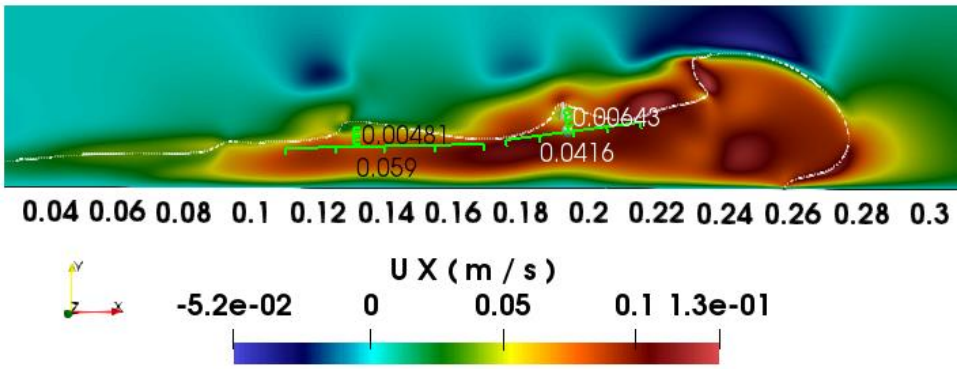

Figure 3.13 . Amplitude of the Holmboe for Re_0 = 2500, We_0 = 250 t = 2 s.

3.5 Relationship between We_{0c} and Re_{0c} of the interface Holomboe instability

In table 3.3, we give the initial Weber critical and intial Reynolds critical numbers in the interface instability between the gravity current and the ambient fluid.

In figure (3.14) diagram of the results for initial Weber critical's numbers of gravity current as a function of the initial critical Reynolds numbers range Re=[500; 2500] are given, it can notice that the initial weber critical numbers decrease by increasing the critical initial Reynold numbers.

Test	**Initial Reynolds critical number**	**Initial Weber critical number**
1	500	250
2	1000	100
3	1500	90
4	2000	50
5	2500	40

Table 3.3. The initial Reynold critical with initial Weber critical numbers

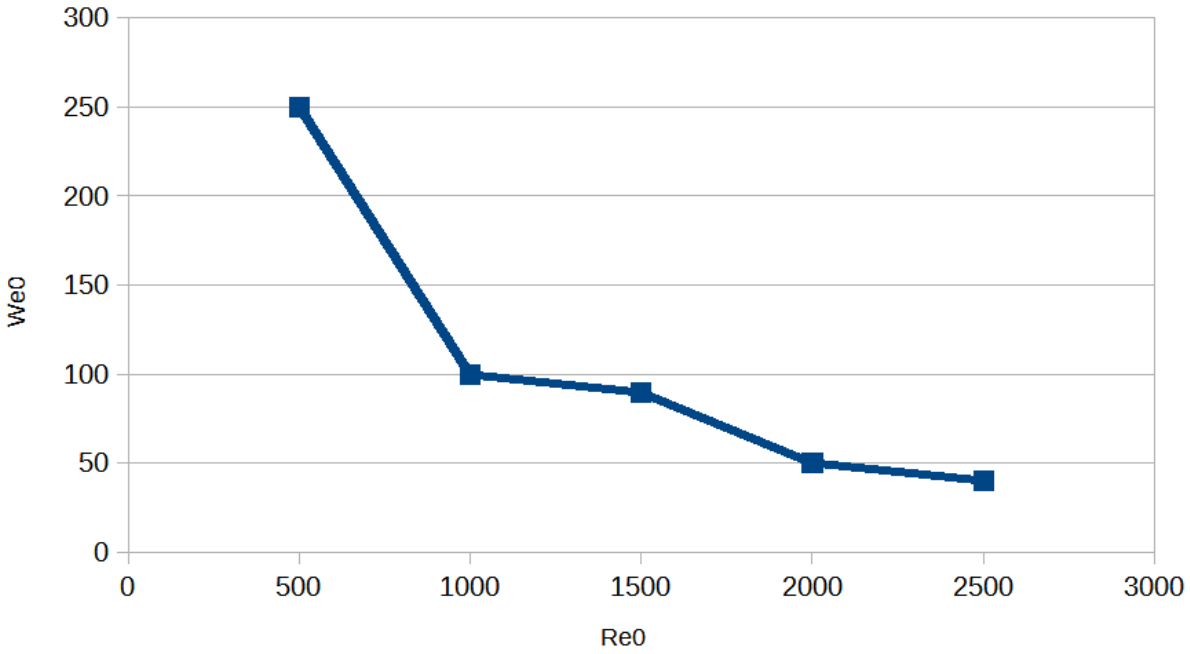

Figure 3.14. Initial Weber critical's numbers as a function of the initial critical Reynolds numbers range Re=500-2500

3.6 Conclusion

We have performed numerical simulations of the exchange flow of two immiscible fluids for intial Reynolds numbers Re_0 = [25; 7000] and initial Weber numbers We_0 = [0; 2500]. The numerical simulations were validated by the theory of Huppert et al (1982) where the front position against time presents a power law in the viscous regime. To complete the validation of our numerical simulations, the effect of the mesh numbers with the apparition of the interface instabilities was used. We have concluded that the mesh with 1000×100 gave the best detection of the interface instabilities between two immiscible liquids.

We have distinguished two interface instabilities: The first one occurs close the bottom (capillary instability) and the second one is in the stratified vertical direction (Holomboe instability).

The numerical simulation results showed that the interface close to the bottom is unstable (capillary instability) for Re_0 = [25; 2000] and for We_0=250. The calculations of the bulk Reynolds ($Re_b = \frac{V_f h}{\nu}$) number and Weber number ($We_b = \frac{\rho V_f^2 h}{\sigma}$) of the front permit to compare the dominate force close the bottom and the head with time. The capillary instability of the interface between the heavier and lighter liquids occurs as drops when Re_b<100 and We_b<10 for Re_0=2000 and We_0=250.

On the other hand, the interface instability in the stratified vertical direction (Holomboe instability) is in the form of cusp-like internal waves; consist of cusps projecting in to the interface between the heavier and the lighter liquids. With the evolution of the flow with time, differences were observed in this wave's structure. It is clear that the growth rate, absolute phase speed, and wavelength are not equal. This instability occurs at the range of initial Reynolds numbers Re_0=[500-7000] for We_0=250. The local Richardson number (Ri_{-loc} which compares the stratification to the shear rate effects) presents a minimum in the Holomboe instability for three cusps positions. This means that the shear rate can destabilize the stratification of the density and can create the instability of Holomboe at the position of the maximum shear rate. The amplitude of the Holomboe instability decreases when the Ri_{-loc} increases. This means that the interface is smooth for the large values of Ri_{-loc}. We estimate that the Holomboe instability occurred when Ri_{-loc} is lower than 10 (the shear rate dominates the stratification).

CHAPTER IV
CONCLUSIONS AND FUTURE WORKS

4 Chapter IV Conclusions and future works

4.1 GENERAL CONCLUSION

In this study we considered the propagation of a gravity current with density greater than that of seawater and therefore flow beneath it and upon a solid plate. We tackled our problem following two scenarios.

The first scenario was devoted to the stability analysis of a thin film propagating beneath a large quantity of ambient static non miscible lighter liquid and over a sloping plane . The study was theoretical. Such configuration that has never been considered earlier can model the spill of a heavy hydrocarbon into the ocean by a tanker, following a voluntary or accidental degassing or an act of war. Equations of conservation of the mass and the momentum were appropriately made non dimensional and a similar solution was proposed in this work. In this way, an analytical expression of the hydrodynamic field, say velocity field and pressure field is provided. Then, the equation governing the spatiotemporal evolution of the water-oil interface was built and solved by a perturbation method. Notably, three flow regimes were identified, say the inertial the viscous and the asymptotic regime in the height spatiotemporal evolution, for assigned aspect ratio λ. Also, the time evolution of the wave front position along the inclined plane was built. Notably, an appropriate non dimensional form of the velocity field shows that it is similar to the case where the surrounding fluid is the atmosphere but with a different average velocity. Consequently, the stability analysis of both configurations and the results of both problems were similar. Notably, the solution to the secular equation showed that at zeroth order, there is no instability with respect to the long wave perturbations considered. At first order, the secular equation was solved numerically by a shooting method. The marginal stability curve was built and the effect of the different forces acting on the flow has been pointed out. It was particularly shown that pressure and surface tension have a stabilizing effect, while inertia has a destabilizing effect.

In the second senario, the main goal of the work was to identify the nature of the instabilities created at the interface in stratified flow between two immiscible liquids with different densities.
We brought out numerical simulations using OpenFoam software in the lockexchange configuration upon horizontal plane. The Navier-Stokes equations were solved for two incompressible and isothermal fluids as well as and an equation for the interphase by using volume of fluid method (VOF). The obtained results from the numerical simulations were validated by the Huppert theory (Huppert et al 1982) of the space-time front position for the initial Reynolds number lying between

25 and 7000 and for initial Weber number between We_0 =250 and for two types of interface instability. The first type is the interface instability between the heavy fluid and the horizontal bottom. This instability occurs for inital Reynolds numbers lying in the range [25-2000] and for initial Weber number We_0 =250.

The second type was the interface instability between the heavy fluid and the ambient fluid far from the bottom and it is called Holmboe instability. The numerical simulation showed that the interface instability is in the form of cusp-like internal waves. It consists of cusps projecting into the interface between the heavy fluid and the ambient fluid and it moves from the left to the right. With the evolution of the flow with time, differences were observed in this waves structure, so this type of instability is the asymmetric holmboe instability.This instability occurs at the range of initial Reynolds numbers 500-7000 and with for initial Weber number We_0 =250.

4.2 Future Works

An analytical and numerical study of gravity currents of intermediate density in stratified water is a possible follow of the invistigations brought out in this thesis.

Bibliography

Ahmed, D. I., Latrache, N. and Nsom, B., (2018). Mixing of Saline Gravity Current Jet into Ambient Freshwater in Weakly Turbulent Regime. J. Hydraul. Eng., 144(5): 0501800.

Ahmed, D. I., Latrache, N., Niang, P. and Nsom, B. (2015). Etalement d'un jet hori zontal miscible de flottabilité positive. 22ndFrench Congress of Mechanics. Lyon, 24 to 28 August. DOI: 10. 13140/RG. 2. 1. 2254. 8880/1.

Ahmed, D. I., Latrache, N. and Nsom, B. (2017). Experimental Study of the Effect of the Spreading Buoyant Gravity current on the Coastal Environment. International Journal of Engineering and Technology, Vol. 9, No. 2.

Ahmed, D. I., Latrache, N. and Nsom, B. (2015). Applied the Large Scale Particle Image Velocimetry Technique for Measurement the Velocity of Gravity Currents in the Laboratory. Journal of Water Resource and Protection. 7, 597-604.

Ahmed, D. I. (2017). Experimental and Numerical Study of Model Gravity Currents in Coastal Environ ment: Bottom Gravity Currents, theis, IRDL, Brest, France. September.

Ahmed, D. I., Latrache, N. and Nsom, B. (2015). Measurement the Velocity by Large Scale-PIV for the gravity Currents flow of a Light Liquid to the Free Surface of a Dense Liquid. LBMS, EA 4325, UBO, Université de Bretagne Occidentale.

Alexakis, A. (2005). On Holmboe's instability for smooth shear and density profiles. Physics of Fluids 17. 084103.

Alexakis, A. (2009). Stratified shear flow instabilities at large Richardson numbers. Physics of Fluids 21. 054108.doi: 10.1063/1.3147934.

Azizyan, G., Pirzadeh B. and Abdollah, Ai. (2020). Hydrodynamic characteristics of lock-exchange flow in curve channels in the presence of blocks. Journal of Hydrosciences and Environment. ISSN: 2345-5608. 10 October.

Balmforth, N. J., Raster, R. V. and Toniolo, C. (2003). Interfacial instability in non-Newtonian fluid layers. Phys. Fluids 15(11). 3370-3384.

Benjamin, T. B., (1968). Gravity currents and related phenomena J. Fluid Mech., vol. 31, part 2, pp. 209-248.

Benjamin, T. B. (1957). Wave formation in laminar flow down an inclined plane. J. Fluid Mech. 2, 554-574.

Birman, V. K., Meiburg, E., and Ungarish, M. (2007). On gravity currents in stratified ambients. Phys. Fluids, vol.19, no. 8, pp. 1-11.

Blanchette,F., (2006). Evaluation of a simplified approach for simulating gravity currents over slopes of varying angles. Computers and Fluids 35. 492 – 500.

Bonnecaze, R., Hall worth M., Huppert H. and Lister, J. (1995). Axisymmetric particle-driven gravity currents. J. fluid Mech. 294: 93-122.

Bonometti, T. and Balachandar, S. (2008). Effect of Schmidt number on the structure and propagation of density currents. Theor. Comput. Fluid Dyn. 22, 341-361.

Britter, R. E. (1979). The spread of a negatively buoyant plume in a calm environmen. Atmos. Environ., vol. 13, pp. 1241-1247.

Carpenter, J. R., Balmforth, N. J. and Lawrence, G.A. (2010). .Identifying unstable modes in stratified shear layers. Phys.Fluids,22, 054104.

Castenedo, S., Medina, R., Losada, I. J., Vidal, C., Mendez, F. J., Osorio, A., Juanes, J. A. and Puente, A. (2005). The Prestige Oil Spill in Cantabria (Bay of Biscay). Part I: Operational Forecasting System for Quick Response, Risk Assessment and Protection of Natural Resources. J. Coastal Res. 22, 272-287.

Ca, V. T. , Cuong,H. ,Thai, T., Hien, N. X., (2014a). A method for locating possible sources of oil pollution in the East Vietnam Sea, Ber.Journal of Water Resources and Environmental Engineering, No. 23, November 2008.

Cesare, G. D., Schleiss, A. and Hermann, F. (2001). Impact of turbidity currents on reservoir sedimentation. Journal of Hydraulic Engineering, 127 (1), 6-16.

Chen, J. D. (1989). Growth of radial viscous fingering in a Hele-Shaw cell. J. Fluid Mech. 201, 223 -242.

Chen, K. P. (1993). Wave formation in the gravity driven low Reynolds number flow of two-liquid film down an inclined plane. Phys. Fluids A 5(12), 3038-3048.

Ciriello, V., Longo S., Chiapponi, L. and Federico V. Di (2016). Porous gravity currents: A survey to determine the joint influence of fluid rheology and variations of medium properties. Advances in Water Resources 92. 105–115.

Clarke, J. C., Smith, R. K. and Reid, D. G. (1981). The Morning Glory of the Gulf of Carpentaria: An atmos pheric undular bore. Mon. Weather Rev. 109, 1726-1750.

Creative Pancake Ideas Your Family Will Go Nuts Over (thespruceeats.com).

Dai, A., Huang, Y. and Hsieh Y. (2021). Gravity currents propagating at the base of a linearly stratified ambient. Phys. Fluids 33,066601.

Dai, A., Huang, Y. and Hsieh Y. (2022). On the merging and splitting processes in the lobe-and-cleft structure at a gravity current head. J. Fluid Mech. vol. 930, A6, doi: 10.1017/ jfm. 2021. 906.

Dayand, P., Man, A., and Zhang, Y. (2012). Principles and Emerging Applications in Biology and Chemistry. Microdroplet Technology. Springer Science and Business Media. pp. 9. 28 July. ISBN978-1- 4614 -3265- 4.

Dias, E. O., Alvarez-Lacalle, E., Carvalho, M.S. and Miranda, J. A. (2012). Minimization of viscous fluid fingering: a variational scheme for optimal flow rates. Phys Rev. Lett., 109, 144502.

Didden, N., Maxworthy, T. (1982). The viscous spreading of plane and axisymmetric gravity current, J. Fluid Mech. 121.

Eames, I., Gilbertson, M. A., Landeryou, M. (2005). The effect of an ambient flow on the spreading of a viscous gravity current. J. Fluid Mech. vol. 523, pp. 261–275.

Farenzena B. A. and Silvestrini, J. H. (2002). Density currents front velocity uncertainty. Computers and Fluids vo. 232, pp 105209, Brazil.

Fay, J. A. (1969). The spread of oil slicks on a calm sea. In Oil on the sea. pp. 33-63. Editor: D. P. Hoult, Plenum.

Felix, M., (2002). Flow structure of turbidity currents. Sedimentology 49, 397- 419.

Francisco, E. P., Espath, L. F. R. and Silvestrini, J. H., (2014). Direct numerical simulation of bi-disperse particle-laden gravity currents, 9th Spring school on transition and turbulence, São Leopoldo, Brazil.

Francisco, E. P., Espath, L. F. R. and Silvestrini, J. H. (2017). Direct numerical simulation of bidisperse par ticle-laden gravity currentsin the channel configuration, Applied Mathematical Modelling. 49. 739-752.

Francisco, E. P. , Espath, L. F. R., Laizet, S. and Silvestrini, J. H. (2018). Reynolds number and settling velocity influence for finite-release particle-laden gravity currents in a basin, Computers and Geosciences110. 1-9.

French-McCay, D. P. (2004). Oil spill impact modeling: Development and validation. Environ. Toxicol. Chem. 23(10), 2441-2456.

Friedlander, S. and Yudovich, V. (1999). Instabilities in Fluid Motion. Notices of the AMS, Volume 46, Number11.

Fowler, A. C and Johnson, C.(1995). Hydraulic run-away: a mechanism for thermally regulated surges of ice sheets. J. Glaciol. 41(139), 554 -561.

Fox, R.W., Mc Donald A. T. and Pritchard P. J. (2004). Introduction to fluid mechanic, (book), sixth edition, USA.

Garoosi, F. and Hooman, K., (2022). Numerical simulation of multiphase flows using an enhanced volume - of- Fluid (VOF) method. International Journal of Mechanical Scinces 215. 106956.

Ggundy, R. E. and Rottman J. W. (1985). The approach to self-similarity of the solutions of the shallow-water equations representing gravity-current releases. J. Fluid Mech. vol. 156, pp. 39-53.

Gratton J. and Vigo C. (1994). Self-similar gravity currents with variable inflow revisited: plane currents. J. Fluid Mech: 258: 77-104.

Greenshields, C. J. (2015). Open FOAM, The Open Source CFD Toolbox, Programmer's Guide, 13th December.

Griffiths, R. W. (1986). Gravity currents in rotating systems. Annu. Rev. Fluid Mech. 18, 59-89.

Gonzalez-Juez, E. and Meiburg, E. (2009). Shallow-water analysis of gravity-current flows past isolatedobstacles. J. Fluid Mech. vol. 635, pp. 415-438.

Guyon, E., Hulin, J. P. and Petit, L. (2001). Hydrodynamique physiqu. EDP Sciences-Paris.

Hacker, J., Linden, P. F. and Dalziel& S. B. (1996). Mixing in lock-release gravity currents. Dyn. Atmos. Oceans 24, 183-195.

Haller M., Cruickshank C., Streicher S., Harrison W., Andersen E., Furbo S. (2009). Methods to determine stratification efficiency of thermal energy storage processes, review and theoretical comparison. Sol Energy: 83: 1847e60.

Hartel, C., Meiburg E. and Necker, F. (2000). Analysis and direct numerical simulation of the flow at a gravity-current head. Part1. Flow topology and front speed for slip and no-slip boundaries. J. Fluid Mech.vol. 418, pp. 189-212.

Hoult, D. P. (1986). Oil spreading on the sea. Annu. Rev. Fluid Mech. 4, 341-368.

https:// iselinc.com/viscosity-qa/

https://www.greenpeace.org/usa/90000-gallon-oil-spill-looks-like/shell-oil-spill-in-the-gulf-of-mexico-4.

https://www.nsf.gov/news/mmg/mmg_disp.jsp?med_id=133765&from.

Huppert, H. E. (2006). Gravity currents: a personal perspective. J. Fluid Mech, vol. 554, pp. 299-322.

Huppert, H. E. (1982b). The flow and instability of viscous gravity currents down a slope. Nature 300, 427- 429.

Huppert, H. E. (1982). The propagation of two-dimensional and axisymmetric viscous gravity currents over a rigid horizontal surface. J. Fluid Mech: 121: 43–58.

Huppert, H. E. and Andrew, W. Woods (1994). Gravity-driven flows in porous layers. J. Fluid Mech. vol. 292, pp. 55-69.

Huppert, H. E. and Simpson J. (1980). The slumping of gravity currents. J Fluid Mech: 99: 785–99.

Huppert, H. E. and Takagi, D. (2007). The effect of confining boundaries on viscous gravity currents. J. Fluid Mech. vol. 577, pp. 495-505.

Huppert, H. E.and Ungarish, M. (2000). High-Reynolds-number gravity currents over a porous boundary: Shallow-water solutions and box-model approximations. J. Fluid Mech. vol. 418, pp.1-23.

InterFoam-OpenFOAMWi (2018). ki.https://openfoamwiki.net/index.php/InterFoam.24 dec.

Issakhov, A. and Imanberdiyeva, M. (2019). Numerical simulation of the movement of water surface of dam break flow by VOF methods for various obstacles. International Journal of Heat and Mass Transfer 136 1030-1051.

Issakhov, A., Zhandaulet, Y. and Nogaeva A. (2018). Numerical simulation of dam break flow for var ious forms of the obstacle by VOF method. International Journal of Multiphase Flow 109. 191-206.

Kaloudis, E., Grigoriadis, D. G. E. and Papanicolaou, E. (2016). Numerical simulations of constant-influx gravity currents in confined spaces: Application to thermal storage tanks. International Journal of Thermal Sciences 108. 1-16.

Kapitza, P. L. and Kapitza, S. P. (1949). Wave flow of thin layers of a viscous liquid. Zh. Eksp. Teor. Fiz., 19, 105-120 (English transl. in Collected Papers of P. L. Kapitza, eds. D. Ter Haar, Pergamon, 1965, pp. 690-709).

Keulegan, G. H. (1957). An experimental study of the motion of saline water from locks into fresh water channels. Nat. Bur. Stand. Rept. 5168.

Khoshkonesh, A., Nsom, B., Dehrashid, F. A., Heidarian P., and Riaz K., (2021). Comparison of the SWE and 3D models in simulation of the dam-break flow over the mobile bed. Fifth scientific Conference of applied research in science and technology of Iran.

Kowal, K. N. and Worster, M. G. (2015). Lubricated viscous gravity current. Journal of Fluid mechanics.

Kowal, K. N. and Worster, M. G. (2019). Stability of lubricated viscous gravity current. J. Fluid Mech. 871, 970-1006.

Kowal, K. N. and Worster, M. G. (2019). Stability of lubricated viscous gravity currents. Part 2: Global analysis and stabilisation by buoyancy forces. Journal of Fluid Mechanics.

Kundu, P. K. and Cohen, I. M. (2002). Fluid Mechanics, Second edition, (book), USA.

Lam, WK., Chan, L., Hasini, H. and Ooi, A., (2018). An Analysis of Two-Dimensional Stratified Gravity Current Flow using Open FOAM. International Journal of Engineering and Technology, 7 (4.35) 589-595.

Lane-Serff, G. F., Beal, L. M. and Hadfield, T. D. (1995). Gravity current flow over obstacles. J. Fluid Mech. Vol 292, 39 –53.

La Rocca, M., Adduce, C., Sciortino, G. and Bateman Pinzon, A. (2008): Experimental and numerical simulation of three-dimensional gravity currents on smooth and rough bottom. Phys. Fluids 20(10), 106603.

Linden, Paul F., (2004). Flow and transport in the Environment. book, USA.

Longo, S. and Federico,V. D. (2014). Axisymmetric gravity currents within porous media: First order solutionand experimental validation. Journal of Hydrology 519. 238-247.

Long, R. R. (1955). Some aspects of the flow of stratied fluids, III. Continuous density gradients. Tellus. VII (3), 341-357.

Marino, B. M., Thomas, L. P., and Linden, P. F. (2005). The front condition for gravity currents. J. Fluid mech. 536, 49-78.

Marino, I. Cantero, J. R., Lee, S. B. and Marcelo, H. G. (2007). On the front velocity of gravity currents .J. Fluid Mech. DOI: 10. 1017 / S0022112007005769.

Marshall, C. R., Dorrell, Dutta, R. M., S., Keevil, Peakall, G. M., J. **and** Tobias S. M. (2021). The effect of Schmidt number on gravity current flows: The formation of large-scale three-dimensional structures. Phys. Fluids 33, 106601.

Martine B. A. and Christophe C. (2006)· Inertial effects on Saffman-Taylor viscous fingering. J. Fluid Mech.vol. 552, pp. 83-97.

Mathunjwa J. S. and Hogg, A. J. (2006). Stability of gravity currents generated by finite-volume releases. J. Fluid Mech. vol. 562, pp. 261-278.

Michael C. D. and Scott W. M. (2011). Numerical solution to the Saffman-Taylor finger problem with kinetic undercooling regularisation . ANZIAM J. 52 (CTAC(2010), pp C124 - C138.

Morhig, D. M., Whipple, K. X., Hondzo, M., Ellis, C. and Parker, G. (1998). Hydroplaning of subaqueous debris flow. Geol. Soc. Am. Bull., 110 (3), 387-394.

Morning glory cloud over Goondiwindi July (2017). Clouds, Natural phenomena, Nature pictures (pinterest.fr) .

Mulder, T. and Alexander, J. (2001). The physical character of subaqueous sedimentary density flows and their deposits. Sedimentology 48: 269-299.

Murray, J. D., (1984). Asymptotic Analysis. Book. USA. volume 48, ISBN978-1-4612-7015-7.

Naranjo, J. A. , Sparks, RSJ, Stasiuk, MV, Mreno H and Ablay, GJ (1992). Morphological,structural and textural variations in the 1988–1990 andesite lava of lonquimay Volcano, Chile. Geol. Mag. 129,657-678.

Nsom, B. (2002). Horizontal Viscous Dam-Break Flow: Experiments and Theory. Journal of Hydraulic Engineering-ASCE, 128: 543-546.

Nsom, B., Alireza K., Saceed G., and Hossein B. (2019). A comprehensive study on dam-break flow over dry and wet beds. J. OceanEngineering 188. pp 106279.

Nsom, B., Debiane K, Piau, J. (2000). Bed slope effect on the dam break problem. Journal of Hydraulic Research.38: 459-464.

Nsom, B, Ndong, W. and Ravelo, B. (2008). Modelling the Zero-Inertia, Horizontal Viscous Dam-Break Problem. Wseas transactions on Fluid Mechanics. ISSN: 1790-5087.

Nsom, B., Ramifidisoa L., Latrache, N. and Ghaemizadeh, F. (2019). Linear stability of shear-thinning fluid down an inclined plane. J. of Molecular Liquids 277pp. 1036-1046.

Oehy, C. D. and Schleiss, A. J. (2007). Control of turbidity currents in reservoirs by solid and permeable obstacles. Journal of Hydraulic Engineering, 133 (6), 637-648.

Ooi, A., Zgheibb, N. and Balachandarb, S. (2015). Direct numerical simulation of three-dimensional gravity on a uniform slope. 7th International Conference on Fluid Mechanics, ICFM7. Procedia Engineering 126. 372-376 .

Orr, W. M. (1907). The stability or instability of the steady motions of a perfect liquid and of a viscous liquid. Proc. R. Irish Acad A., 27: 9-68, 69-138.

Ottolenghi, L., Adduce, C. , Inghilesi, R., Armenio, V. and Roman, F. (2016). Entrainment and mixing in unsteady gravity currents. Journal of Hydraulic Research Vol. 54, No. 5. pp. 541-557.

Ottolenghi,L., Prestininzi, P., Montessori, A., Adduce, C. and Rocca, M.L., (2018). Lattice Boltzmann simulations of gravity currents.European Journal of Mechanics / B Fluids 67. 125–136.

Papakonstantis, I. G., and Christodoulou G. C. (2010). Spreading of round dense jets impinging on a horizontal bottom, J. Hydro-environment Res. 4, 289-300.

Patterson, M. D., Simpson, J. E., Dalziel, S. B. and Nikiforakis, N. (2005). Numerical modelling of two-dimensional and axisymmetric gravity cur rents. Int. J. Numer. Meth. Fluids: 47: 1221–1227. DOI: 10. 1002 / d. 841.

Pelmarda, J., Norris, S. and Friedricha, H. (2018). LES grid resolution requirements for the modelling of gravity currents. Computers and Fluids vol. 174. P 256-270, New Zealand.

Penney, J. and Stastna, M., (2016). Direct numerical simulation of double-diffusive gravity currents. Physics of fluids 28, 086602, Canada.

Pouliquen, O., Chomaz, J. M. and Huerre, P. (1993). Propagating Holmboe waves at the interface between two immiscible fluids, J. Fluid Mech. (1994), vol. 266, pp. 217-302.

Reed, M., Johansen, O., Brandvik, P. J., Daling, P., Lewis, A., Fiocco, R., Mackay, D. and Prentki, R. (1999). Oil spill modeling towards the close of the 20th century: Overview of the state of the art. Spill Sci. Technol. Bull. 5(1), 3-16.

Ross, A. N., Linden, P. F., and Dalziel, S. B. (2002). A study of three-dimensional gravity currents on a uniform slope. J. Fluid Mech. 453, 239- 261.

Rottman, JW. and Simpson JE. (1983). Gravity currents produced by instantaneous releases of a heavy fluid in a rectangular channel. J Fluid Mech. 135: 95-110.

Rottman, J. W., Simpson, J. E., Hunt, J. C. R. and Britter, R. E. (1985). Unsteady gravity current flows over obstacles: some observations and analysis related to the phase II trials. J. Hazard.Mater. Vol11, 325-340.

Ruyer-Quil, C. and Manneville, P. (2000). Improved modeling of flows down inclined plane. Eur. Phys. J. B, 15, 357-369.

Schmid, Peter J. and Henningson, D. S. (2001). Stability and Transition in Shear Flows. Book., USA., Book., volume 12, ISBN 978-1-4612-6564-1.

Sea Breeze Pictures | Download Free Images on Unsplash.

Shin, J. O., Dalziel, S. B. and Linden P. F. (2004). Gravity currents produced by lock exchange. Uk. J. Fluid Mech. vol. 521, pp. 1–34.

Shringarpure, M., Lee, H.,Ungarish, M.and Balachandar, S. (2013). Front conditions of high-Re gravity currents produced by constant and time-dependent influx: An analytical and numerical study. European Journal of Mechanics B / Fluids 41109-122.

Simpson, J. E. (1997). Gravity Currents in the Environment and the Laboratory, Cambridge University Press.

Simpson, J. E. (1982). Gravity Currents in the Laboratory, Atmosphere, and Ocean. Annual Review of fluid Mechanics. 14: 213-234. Bibcode: 1982 AnRFM. 14. 213S. doi: 10.1146 / annurev. fl. 14. 010182. 001241.

Simpson, J. E., Maxworthy T., Leilich, J. and Meiburg, E. H. (2002). The propagation of a gravity current into a linearly stratied fluid. J. Fluid Mech. vol. 453, pp. 371-394.

Smith, R. K., Crook, N. and Roff, G.,(1982) . The Morning Glory: an extraordinary atmospheric undular bore. Quart. J. Roy. Meteorol. Soc. 108, 9.

Sommerfeld, A. (1908). Ein beitrag zur Hydrodynamischen Erklaerung der Turbulenten Fluessigkeitsbewegungen. In “Atti del 4 Congresso Inenazionale dei Matematic”, Ser. I, 3, 116-124, Roma (in German).

Tansel, B. (2014). Propagation of impacts after oil spills at sea: Categorization and quantification of local vs regional and immediate vs delayed impacts. Int. J. of Disaster Risk Reduction 7, 1-8.

Tavakol, B., Froehlicher, G. , Holmes, D. P. and Stone, H. A. (2017). Extended Lubrication Theory: Improved Estimates of Flow in Channels with Variable Geometry. physics.flu-dyn., arXiv: 1403. 2343v2.

Thomas, L. P. Marino, B. M. and Linden, P. F. (1998). Gravity currents over porous substrate. J. Fluid Mech. 366, 239-258.

Thomas, L. P. , Marino, B. M. and Linden, P. F. (2004). Lock-release inertial gravity currents over a thick porous layer. J. Fluid Mech. vol. 503, pp. 299–319.

Ungarish, M. (2009). An Introduction to Gravity currents and Intrusions, Chapman and Hall /CRC, Taylor and Francis Group, Boca Raton, F1.
Ungarish, M., and Zemach, T. (2005). On the slumping of high Reynolds number gravity currents in

two-dimensional and axisymmetric configurations. European Journal of Mechanics B / Fluids 24, 71-90.

Verhulst, F. (2000). Methods and Applications of Singular Perturbations, Boundary Layers and multiple Timescale Dynamics. Book., USA., SPIN 11005988.

Von Kàrmàn, T. (1940). The engineer grapples with nonlinear problems. Bull. M. Math. Soc. 46,615- 683.

Woumeni, R. (1991). Etude des instabilités visqueuses en milieu poreux à l'aide d'un scanner à ultrason. Thèse Université Paris VII.

Xie, C. Y., Tao, J. J. and Zhang L. S. (2019). Origin of lobe and cleft at the gravity current front. Physical review E 100, 031103 (R). DOI: 10. 1103 / PhysRevE. 100. 031103.

Yang, A. J.K., Tedford, E. W., Olsthoorn, J. , Lefauve, A. and . Lawrence, G. A (2021). Reynolds stresses in Holmboe instabilities. from linear growth to saturation .the Journal of Fluid Mechanics , Vol. 1, No. 12220, May.

Yih, C.S. (1967). Instability due to viscosity stratification. J. Fluid Mech. 27, 337-352.

Yiqun Ye, Tibing and David Z. Zhu. (2020). Numerical analysis of dam-break waves propagating over dry and wet beds by the mesh-free method. Ocean Engineering 217. 107969.

Zemach, T. (2019). Asymptotic similarity solutions for particle-driven gravity currents in non-rectangular cross-section channels of power-law form. European Journal of Mechanics / B Fluids: 74, 312–319.

Zgheib, N., Bonometti, T. and Balachandar, S. (2015). Direct numerical simulation of cylindrical particle-laden gravity currents Computers and Fluids 123. 23-31.

Zhang, L. Z., Zeng, L., Zhang, B., Li, Z. and Luo, Z. L. (2010). Numerical study on head advancement of axisymmetric gravity currents. Commun Non linear Sci Numer Simulat15. 1893-1898.

Z. H. Gu, H. L. Wen, C. H. Yu and Tony W. H. Sheu. (2018). Interface-preserving level set method for simulating dam-break flows, Journal of Computational Physics 374. 249-280.

Zhu, J.B. , Lee, C. B., Chen, G. Q. and Lee, J. H. W. (2006). PIV observation of instantaneous velocity structure of lock release gravity cur rents in the slumping phase. Communications in Nonlinear Science and Numerical Simulation 11. 262-270.

Zukoski, E. E. (1966). Influence of viscosity, surface tension, and inclination angle on motion of long bubbles in closed tubes. J. Fluid Mech. 25, 821.

COLLEGE DOCTORAL BRETAGNE SCIENCES POUR L'INGENIEUR

Université de Bretagne Occidentale

Titre : Stabilité des courants de gravité complexes en milieu côtier

Mots clés : Analyse de stabilité linéaire, Courant gravitaire, Interface liquide/liquide

Résumé : La côte est la zone de contact entre le continent et la mer. Il est donc susceptible de collecter des liquides pollués provenant à la fois de la mer et du continent. Cette thèse considère le cas où le liquide intrusif qui est déplacé par la seule gravité et est appelé le courant de gravité, est plus dense que l'eau de mer et coule donc en dessous de celle-ci. Les liquides sont non miscibles et ont la même viscosité. La stabilité hydrodynamique de l'interface de ce système liquide/liquide est abordée à la fois analytiquement et numériquement. Le modèle analytique étudie la stabilité temporelle d'une petite perturbation superposée à l'interface de ce système liquide/liquide afin de déterminer les paramètres critiques caractérisant l'apparition de l'instabilité. L'étude numérique vise à identifier la nature des instabilités créées à l'interface d'un système de deux liquides non miscibles de densités différentes dans une configuration d'écluse sur un plan horizontal. La différence de densité est maintenue fixe tandis que les viscosités sont augmentées pour contrôler le nombre de Reynolds initial. La tension superficielle interfaciale est variée pour contrôler le nombre de Weber initial. La compétition entre stratification et cisaillement conduit à une instabilité de Kelvin-Helmholtz ou Holmboe à l'interface. La réponse à cette question est de comparer l'épaisseur du gradient de vitesse et celle du gradient de densité près de l'interface. Pour le cas de deux liquides non miscibles, l'épaisseur du gradient de densité est égale à zéro. Dans ce cas, seuls la position de l'interface et le gradient de vitesse doivent être calculés.

Title : Stability of Complex Gravity Currents in Coastal Environment

Keywords : Linear stability analysis, Gravity current, Liquid/liquid interface

Abstract : The coast is the contact zone between the continent and the sea. It is therefore likely to collect polluted liquids coming from both the sea and the continent. This thesis considers the case where the intruding liquid which is moved by gravity alone and is called the gravity current, is denser than seawater and therefore flows below it. Liquids are immiscible and have the same viscosity. The hydrodynamic stability of the interface of this liquid/liquid system is addressed both analytically and numerically. The analytical model studies the temporal stability of a small disturbance superimposed at the interface of this liquid/liquid system in order to determine the critical parameters characterizing the appearance of the instability. The numerical study aims to identify the nature of the instabilities created at the interface of a system of two immiscible liquids of different densities in a lock configuration on a horizontal plane. The difference in density is kept fixed while the viscosities are increased to control the initial Reynolds number. The interfacial surface tension is varied to control the initial We-ber number. The competition between stratification and shear leads to a Kelvin-Helmholtz or Holmboe instability at the interface. The answer to this question is to compare the thickness of the velocity gradient and that of the density gradient near the interface. For the case of two non-target liquids, the thickness of the density gradient is equal to zero. In this case, only the interface position and the velocity gradient need to be calculated.